Label-Free molecular imaging and discrimination of stem cells by Raman micro-spectroscopy

by

Adrian Ghita

Thesis submitted to the University of Nottingham
for the degree of Doctor of Philosophy
September 2013
School of Physics and Astronomy

Abstract

This thesis is focused on the development of Raman micro-spectroscopy for label free imaging and discrimination of stem cells.

The thesis is divided into six chapters. Chapter 1 gives an overview of the existing techniques used for molecular analysis of cells, with emphasis on methods that allow non-invasive label-free imaging. A literature review of the main relevant applications of Raman micro-spectroscopy for imaging cells was also included.

Chapter 2 discusses the basic theoretical principles of Raman scattering and design of Raman micro-spectrometers. The practical aspects related to the design of an optimised Raman micro-spectrometer are presented in Chapter 3 along with experimental characterisation of its performance. The chapter concludes with examples of Raman spectral maps of endothelial cells.

Chapter 4 and Chapter 5 present experimental results obtained by Raman micro-spectroscopy for molecular analysis of live neural and mesenchymal stem cells. In these investigations Raman spectroscopy was used to identify, image and quantify spectral markers for label-free discrimination between glial cells and their neural progeny. The potential of Raman micro-spectroscopy to measure time-course molecular changes of individual bone nodules was demonstrated in Chapter 5. Future work and final conclusion are discussed in Chapter six of this thesis.

List of publications:

A. Ghita, F. Pascut, V. Sotille and I. Notingher, **Monitoring the mineralisation of bone nodules in-vitro by space- and time-resolved Raman micro-spectroscopy** *manuscript submitted to Analyst*

A. Ghita, F. C. Pascut, M. Mather, V. Sottile, and I. Notingher, **Cytoplasmic RNA in Undifferentiated Neural Stem Cells: A Potential Label-Free Raman Spectral Marker for Assessing the Undifferentiated Status**, *Anal. Chem., 2012, 84 (7), 3155–3162*

M. Larraona-Puy, A. Ghita, A. Zoladek, W. Perkins, S. Varma, I. H. Leach , A. A. Koloydenko, H. Williams and I. Notingher. **Discrimination between basal cell carcinoma and hair follicles in skin tissue sections by Raman micro-spectroscopy**, *J Mol Struct 2011, 993(1-3), 57-61*.

M. Larraona-Puy, A. Ghita, A. Zoladek, W. Perkins, S. Varma, I. H. Leach , A. A. Koloydenko, H. Williams and I. Notingher. **Development of Raman micro-spectroscopy for automated detection and imaging of basal cell carcinoma**, *J Biomed Opt 2009, 4(5): 054031*.

Table of contents

Chapter 1: Introduction to stem cells and methods for molecular imaging and discrimination

This chapter provides the scientific background and motivation of the research presented in the thesis. It gives an introduction to stem cells, with emphasis on neural stem cells and osteoblasts derived from mesenchymal stem cells, as these cells are the focus of interest in this project.

1.1 Methods for molecular analysis of individual cells

The capacity of the human body to recover from injuries or diseases is limited and in some situations almost non-existent. The standard medical procedures which involve surgery and drug based therapies have shown limitations in treating many complex conditions. New alternatives to existing medical treatments are required as the incidence of the medical conditions with clinical impact on society in terms of mortality, morbidity and quality of life is continuously increasing.

Tissue engineering is an emerging new field in modern medicine that aims to grow tissue in laboratories that can be used for replacement of diseased tissue and organs, repair and regeneration. Tissue replacement involves the growth of tissue and organs in-vitro to be implanted in the human body [1]. Repair involves medical treatment at the biological and molecular level. Regeneration is referred to in-vivo stimulation of organ or tissue development. The main advantages of the tissue engineering approaches are related to reduce the risks associated with tissue availability and viral infections (e.g. tissue rejection) or negative immunological response [2].

A number of different sources of cells are used or are considered to be used for tissue engineering, ranging from mature, fully differentiated somatic cells, adult stem cells, to human embryonic stem cells. The somatic cells extracted from the patients have no risks associated with the integration and immune response from the organic host as they are obtained in a limited number and have a low proliferation rate. On the other hand, adult stem cells are immature undifferentiated cells extracted from sites of human body, usually bone marrow, and are capable of

generating daughter cells. The self-renewal process occurs over the entire life time of the biological host. However, the limited number of available adult stem cells in the human body gives rise to impediments in the self-healing capabilities of the human body. Embryonic stem cells (ESCs) are derived from the inner cell mass of mammalian blastocyste and can differentiate spontaneously in vitro giving rise to pluripotent cells [3]. Therefore ESCs can serve as a potential research model for tissue development, cancer formation and metastasis, phenotype commitment, stem cells based therapy, gene therapy strategies and drug design [4].

Neural stem cells are responsible for the generation of neurons and glials cells and offer great promise for developing treatments for Parkinson's, Alzheimer's diseases, chronically inflammatory disorders of the central nervous system (CNS), as well as spinal cord injuries or strokes [5]. The capacity of endogenous neural stem cells to proliferate and replace the neural cells in-vivo may be affected by chronic inflammatory processes [5]. Hence the repair potential of endogenous stem cells may be limited and any medical procedures designed to mobilize neural stem towards inflammatory sites may be limited. Thus, therapies based on transplantation of neural stem cells from exogenous sources have been developed recently [6].

Bone is one of the biggest organs in the human body that has numerous mechanical and haematological functions. In addition to age-related diseases, there are congenital bone deformation, bone cancer and bone trauma that may require bone transplant. Current bone reconstruction and replacement surgical procedures are based on allogeneic tissue graft. Because of a limited supply of allogeneic bone,

engineering tissue-regeneration of the bone based on mesenchymal stem cells has raised a huge research interest. The growth of bone in-vitro requires culture of mesenchymal stem cells (MSCs) in osteogenic culture medium. Following proliferation and differentiation, MSCs give rise to osteoblasts, which are specialized cells responsible for formation of the bone nodules. The bone grafts obtained in-vitro can be used for clinical applications to restore the functionality of the skeletal system of the patients [1].

Despite their clinical potential, the progress of stem cell therapy has been limited by many challenges such as issues related to cell quality, phenotype heterogeneity, population number, delivery and integration with the biological host or proliferation and differentiation inside the host [7]. These challenges are in part due to the limited availability of non-invasive techniques able to characterize the cells at the molecular level.

During the last century, a plethora of chemical and imaging analysis techniques have been developed to understand the molecular dynamics underpinning the fundamental cellular processes such as proliferation, differentiation or apoptosis [8, 9]. These analytical techniques have potential benefits and can address certain types of applications or particular biological problems or processes. These encompass a broad range of techniques, from destructive assays targeting specific molecules to label free approaches [10] such as polymerise chain reaction (PCR), optical microscopy, capillary electrophoresis (CE), mass spectrometry (MS)), scanning probe microscopy (SPM), optical microscopy, nuclear magnetic resonance (NMR), transmission electron microscopy (TEM). In fact, besides NMR,

SPM, and optical microscopy, the vast majority of the techniques used to characterize cells are destructive and cannot be used for assessing the cells prior to clinical use.

Scanning probe microscopy describes a cluster of surface science methods based on the interaction between a probe (tip) and the sample surface. The force exchange between the tip and a surface (atomic force microscopy or AFM), magnetic force microscopy and electrostatic force) or charge carriers transfers (scanning ion conductance microscopy or SICM) can be used for topographic imaging of the cells. Atomic force microscopy is one of the most versatile surface characterization techniques and can image cells in liquid [11]. AFM nano-indentation was used to probe the dynamic mechanical properties of the cells [12]. Under sheer stress, the cells exhibited an increased stiffness which was correlated with mechanical changes of actin filaments in the cell cytoplasm [13]. Scanning ion conductance microscopy (SICM) can examine the cells without affecting their integrity or behaviour[14]. The tip used in SICM is a glass micropipette filled with an electrolyte and an electrode inside it. The tip senses the flow of ion currents and it does not require contact with the cell. The SICM is suitable for mapping of non-conducting samples immersed in electrolytes and can build topographical images of live cells in culture medium [15]. SICM can resolve fine structures on the cell surface, track cell movement [16], map protein dynamics or microvilli patterns on plasma membrane structure [17, 18] and cell response under different stimuli [19]. The SPM imaging is rather slow and can suffer from inconsistencies between tips.

Optical microscopy refers to a class of imaging techniques that are routinely used by biologists to obtain magnified images of the cells. Albeit conventional bright field or phase contrast microscopy is non-destructive and label-free, these imaging modality does not provide molecular information.

Fluorescence microscopy is a very popular optical technique that has been used in biological laboratories for many years. This technique relies on selective imaging of cellular molecules labelled with specific fluorescent dyes [20]. The most common approach in fluorescence microscopy is to add fluorophores that will chemically bind to the desired molecules inside the cells' structures or to genetically engineer the cells to express fluorescent protein such as green fluorescent protein (GFP) [21]. Wide-field fluorescence microscopy is the most common version of fluorescence microscopy [22], [23] but its downside is the low resolution images especially for samples with a height greater than 30 μm. Confocal fluorescence microscopy and multi-photon microscopy on the other hand can provide images with higher spatial resolution [24, 25]. Surface details and subsurface can be visualized by total internal fluorescence microscopy (TIRFM) [26], protein–protein interaction via fluorescence resonance energy transfer microscopy (FRET) [27-29]. At the same time FRET signal suffers from contamination coming from donor emission into acceptor channel and excitation of acceptor molecule. Details with spatial resolution beyond diffraction limit require super resolution techniques such as stimulated emission depletion microscopy (STED) [30, 31], 4Pi , structured illumination microscopy (SIM) or stochastic optical reconstruction microscopy (STORM), photo activated localization

microscopy (PALM) [32-34]. Fluorescence imaging techniques have limited application capabilities because they require the use of specific markers and suffer from limited stability and photo bleaching of the fluorophores. In addition the free radical released inside the cell during photo-excitation can be very toxic for cells. Transgenic expression of GFP which used to monitor protein localization in live cell can induce toxicity to the live cell lines leading to apoptosis [35]. Also, the multiple labelling in fluorescence imaging can raise difficulties because of the possibility of the emission signals overlap. Cell heterogeneity and accessibility of certain structures inside cells are often restricted by fluorescent dyes.

Many destructive assays such as polymerised chain reaction (PCR) [36], serial analysis of gene expression (SAGE) [37], capillary electrophoresis (CE) [38] [39] and bloting methods (Southern blot, Western Blot, Northern Blot) [40-43] are used for quantification of the gene expression, proteins, nucleic acids, ascorbic acid in cells [44] or to determine intracellular content of small amino-acids in the cells [45]. Mass spectrometry is a very sensitive analytical method that can identify chemicals by their mass to charge ratio with high chemical specificity. Schneiter et al. have coupled ESI-MS in order to elucidate biochemical difference of lipids species from various organelles membranes [46] and found the highest amount of lipid marker in the cell membrane. Chemical profiling by ESI-MS followed by multivariate analysis was able to discriminate between bacteria species for the purpose of accurate detection of pathogens [47]. Matrix assisted laser desorption/ionization (MALDI) is considered a soft ionization method that allows the extraction of biomolecules such as DNA, protein or amino-acids. This method

has been used to map the spatial distribution of peptides and peptides fragments which were in cultured Aplysia californica neurons [48].

The main limitations of mass spectrometry are the need to couple the spectrometers to a method of extraction of ions and molecules such as ablation or ionization. Therefore mass spectrometry is an invasive technique that cannot be used for live cell studies.

1.2 Raman spectroscopy of individual cell and molecular analysis

Raman spectroscopy is a label-free analytical technique that can provide detailed molecular information of a sample in non-destructive way. Similar to infared (IR) spectroscopy, Raman spectroscopy measure the transitions between vibrational levels of the molecules, but the underlying principles are completely different. However, while IR is based on absorption of electromagnetic radiation by the molecules, Raman spectroscopy relies on the inelastic scattering of incident radiation by the molecules.

When applied to molecular analysis of cells, IR spectroscopy measurements can be difficult due to the strong absorbance of water in the IR region and modest spatial resolution [49]. With new technological advances in lasers, optics and CCD cameras, Raman micro-spectroscopy has become a realistic

alternative to IR spectroscopy in the fields of biochemistry for imaging and non-invasive characterization of live cells [50].

Near infrared lasers can provide submicron spatial resolution while water has a small Raman scattering cross section. Therefore, measurement of cells in culture can be analysed significantly easier and higher spectral resolution compared to IR spectroscopy.

The first Raman micro-spectrometer was proposed and demonstrated by Dhamelincourt and Delhaye in 1973 [51] but it was not until 1990 when Puppels et al were able to measure the first Raman spectra of living cells [52]. Since then Raman spectroscopy was used to study, protein conformation in living cells [53], stem cell [54], probe chemical differences at different stages of the cell cycle [55, 56] between cells with different phenotypes [57], [58] and compare between live and apoptotic cells [59]. The most important feature of the Raman spectroscopy is the ability to measure molecular properties of live cells in a culture medium, without chemical or mechanical interference. Hence, Raman spectroscopy can be a reliable tool for real-time monitoring of cell differentiation. Early studies investigating the effect of laser irradiation of cells at different wavelengths and powers indicated has revealed that near infrared laser do not affect cell functionality [60]. Fourier analysis of the beating frequency of cardiomiocytes before and after irradiation with 785 nm laser provided similar results [61]. Raman spectroscopy can probe molecular information from living cells revealing distinct chemical features between nucleus and cytoplasm [52, 62], [72, 73], lipid structure inside cytoplasm [63], and cell response to diverse stress stimuli [64, 65]. For

future reading, the reader may address to a few relevant reviews on Micro-Raman spectroscopy for single cells analysis [66-69].

Searching for chemical discriminates of cancer cells from normal cells along with cancer drugs screening are one of the main goals in cancer research. More recently, several groups have shown that Raman spectroscopy can measure biochemical differences between different cell lines [70] or individual normal cells and cancer cells [71, 72], including neoplastic and normal hematopoietic cells [71]. Raman spectroscopy was also used to study the anticancer drugs at a single cell level [66]. Cisplatin is another anticancer used for chemotherapy. Exposure of the cells to the drug, has led to modifications in protein secondary structures as revealed by Raman spectroscopy [73].

Raman spectroscopy was also used to obtain biochemical information at the early stages of embryogenesis of murine stem cell [74], and to address one major problem in stem cell therapy, the phenotype heterogeneity of the cell populations obtained after stem cell differentiation. The differentiation process describes a series of biochemical changes which are meant to transform a stem cell into a fully functional somatic cell. These changes can be correlated to changes in the Raman spectra of cells [75]. Recent studies have shown that Raman spectral markers can be used to discriminate fully committed mature cells from undifferentiated cells [76-80] and to assess the differentiation status of murine stem cells [79].

A higher amount of nucleic acids (DNA and RNA) was found in murine embryonic stem cells compared to fully differentiated cells [77]. The intensity of

the Raman bands assigned to DNA peak were reduced by 50% in newly differentiated cells which is explained by the lower proliferation rate [75].

The human heart is considered to be a non-regenerative tissue and the permanent loss of cardiomyocites can lead to cardiac muscle failure. For this reason stem cell therapy for replacing damaged cardiac tissue is considered an alternative to classical heart transplants. Recent reports indicated that the Raman spectroscopy label can discriminate cardiomyocites (CM) from other phenotypes [65]. Moreover the spectral marker that distinguishes between the phenotypes of CM and non-cardiomyocites was found to be glycogen [80] and was quantified in human embryonic stem cells [81]. The statistical model developed based on PCA analysis can discriminate between CM and non- cardiomyocites with 97% specificity and 96 % sensitivity [65].

Human mesenchymal stem cells can differentiate into osteoblastic lineage, when cultured in osteogenic medium. The changes can lead to spatial separation in 950-960 cm^{-1} region associated to vibrations of peak in hydroxyapatite [82, 83]. For a better understanding of the bone formation process several cell types (mouse ESC (mESC), neonatal calvaria osteoblast (OB), and adult bone marrow mesenchymal stem cells (MSC) have been tested in vitro for bone mineralization and then compared to native bone [84].

Raman imaging provides new insights into cells by probing the spatial distribution of chemical species and organelles inside cells [85-91]. Furthermore, Raman experiments were able to follow the cellular uptake of the drugs [92-95], cellular dynamics [96], and continuous biochemical changes throughout cell cycles

[97]. Apoptosis, also known as programmed cell death, is an important biological phenomenon that involves morphological and chemical changes of the cell organelles. Raman spectral mapping of apoptotic cells showed changes in the distribution of the nucleic acids [98, 99] and detected the accumulation of lipids when cells were treated with different apoptotic drugs [100-103]. Krafft et al have applied multivariate analysis to image morphological differences between normal and apoptotic cells [104].

Time course experiments measuring Raman spectra of cells in-vitro revealed spatial and temporal molecular changes related to apoptosis [94], cardiac differentiation of human embryonic stem cells [105], formation of the endoderm layer in embryonic bodies [106], mitosis of living yeast cells [97, 107] or release of cytochrome c from mitochondria during apoptosis [108].

References:

1. Frohlich, M., et al., *Tissue engineered bone grafts: biological requirements, tissue culture and clinical relevance.* Curr Stem Cell Res Ther, 2008. **3**(4): p. 254-64.
2. Williams, D., *Benefit and risk in tissue engineering.* Materials Today, 2004. **7**(5): p. 24-29.
3. Evans, M.J. and M.H. Kaufman, *Establishment in culture of pluripotential cells from mouse embryos.* Nature, 1981. **292**(5819): p. 154-6.
4. Dean, M., *Cancer stem cells: redefining the paradigm of cancer treatment strategies.* Mol Interv, 2006. **6**(3): p. 140-8.
5. Martino, G. and S. Pluchino, *The therapeutic potential of neural stem cells.* Nat Rev Neurosci, 2006. **7**(5): p. 395-406.
6. Giusto, E., et al., *Neuro-immune interactions of neural stem cell transplants: From animal disease models to human trials.* Exp Neurol, 2013.
7. Choumerianou, D.M., H. Dimitriou, and M. Kalmanti, *Stem cells: promises versus limitations.* Tissue Eng Part B Rev, 2008. **14**(1): p. 53-60.
8. Trouillon, R., et al., *Chemical analysis of single cells.* Anal Chem, 2013. **85**(2): p. 522-42.
9. Lin, Y., et al., *Chemical analysis of single cells.* Anal Chem, 2011. **83**(12): p. 4369-92.
10. Skommer, J., Z. Darzynkiewicz, and D. Wlodkowic, *Cell death goes LIVE: Technological advances in real-time tracking of cell death.* Cell Cycle, 2010. **9**(12).
11. Butt, H.J., et al., *Imaging cells with the atomic force microscope.* J Struct Biol, 1990. **105**(1-3): p. 54-61.
12. Kuznetsova, T.G., et al., *Atomic force microscopy probing of cell elasticity.* Micron, 2007. **38**(8): p. 824-833.
13. Sato, M., et al., *Local mechanical properties measured by atomic force microscopy for cultured bovine endothelial cells exposed to shear stress.* J Biomech, 2000. **33**(1): p. 127-35.
14. Korchev, Y.E., et al., *Specialized scanning ion-conductance microscope for imaging of living cells.* J Microsc, 1997. **188**(Pt 1): p. 17-23.
15. Chen, C.C., Y. Zhou, and L.A. Baker, *Scanning Ion Conductance Microscopy.* Annual Review of Analytical Chemistry, Vol 5, 2012. **5**: p. 207-228.
16. Korchev, Y.E., et al., *Scanning ion conductance microscopy of living cells.* Biophys J, 1997. **73**(2): p. 653-8.
17. Shevchuk, A.I., et al., *Imaging proteins in membranes of living cells by high-resolution scanning ion conductance microscopy.* Angew Chem Int Ed Engl, 2006. **45**(14): p. 2212-6.

18. Gorelik, J., et al., *The use of scanning ion conductance microscopy to image A6 cells.* Molecular and Cellular Endocrinology, 2004. **217**(1-2): p. 101-108.
19. Korchev, Y.E., et al., *Cell volume measurement using scanning ion conductance microscopy.* Biophys J, 2000. **78**(1): p. 451-457.
20. Bour-Dill, C., et al., *Determination of intracellular organelles implicated in daunorubicin cytoplasmic sequestration in multidrug-resistant MCF-7 cells using fluorescence microscopy image analysis.* Cytometry, 2000. **39**(1): p. 16-25.
21. Rusan, N.M., et al., *Cell cycle-dependent changes in microtubule dynamics in living cells expressing green fluorescent protein-alpha tubulin.* Mol Biol Cell, 2001. **12**(4): p. 971-80.
22. Robinett, C.C., et al., *In vivo localization of DNA sequences and visualization of large-scale chromatin organization using lac operator/repressor recognition.* J Cell Biol, 1996. **135**(6 Pt 2): p. 1685-700.
23. Janicki, S.M., et al., *From silencing to gene expression: real-time analysis in single cells.* Cell, 2004. **116**(5): p. 683-98.
24. Nichols, B.J., et al., *Rapid cycling of lipid raft markers between the cell surface and Golgi complex.* J Cell Biol, 2001. **153**(3): p. 529-41.
25. Presley, J.F., et al., *ER-to-Golgi transport visualized in living cells.* Nature, 1997. **389**(6646): p. 81-5.
26. Schneckenburger, H., *Total internal reflection fluorescence microscopy: technical innovations and novel applications.* Current Opinion in Biotechnology, 2005. **16**(1): p. 13-18.
27. Truong, K. and M. Ikura, *The use of FRET imaging microscopy to detect protein-protein interactions and protein conformational changes in vivo.* Curr Opin Struct Biol, 2001. **11**(5): p. 573-8.
28. Elangovan, M., R.N. Day, and A. Periasamy, *Nanosecond fluorescence resonance energy transfer-fluorescence lifetime imaging microscopy to localize the protein interactions in a single living cell.* J Microsc, 2002. **205**(Pt 1): p. 3-14.
29. Elangovan, M., et al., *Characterization of one- and two-photon excitation fluorescence resonance energy transfer microscopy.* Methods, 2003. **29**(1): p. 58-73.
30. Klar, T.A., et al., *Fluorescence microscopy with diffraction resolution barrier broken by stimulated emission.* Proc Natl Acad Sci U S A, 2000. **97**(15): p. 8206-10.
31. Muller, T., C. Schumann, and A. Kraegeloh, *STED microscopy and its applications: new insights into cellular processes on the nanoscale.* Chemphyschem, 2012. **13**(8): p. 1986-2000.
32. Nagerl, U.V., et al., *Live-cell imaging of dendritic spines by STED microscopy.* Proc Natl Acad Sci U S A, 2008. **105**(48): p. 18982-7.
33. Hein, B., K.I. Willig, and S.W. Hell, *Stimulated emission depletion (STED) nanoscopy of a fluorescent protein-labeled organelle inside a living cell.* Proc Natl Acad Sci U S A, 2008. **105**(38): p. 14271-6.
34. Huang, B., M. Bates, and X. Zhuang, *Super-resolution fluorescence microscopy.* Annu Rev Biochem, 2009. **78**: p. 993-1016.

35. Liu, H.S., et al., *Is green fluorescent protein toxic to the living cells?* Biochemical and Biophysical Research Communications, 1999. **260**(3): p. 712-717.
36. Doyle, L.A., et al., *A multidrug resistance transporter from human MCF-7 breast cancer cells.* Proc Natl Acad Sci U S A, 1998. **95**(26): p. 15665-70.
37. Velculescu, V.E., et al., *Serial analysis of gene expression.* Science, 1995. **270**(5235): p. 484-7.
38. Nemes, P., et al., *Metabolic differentiation of neuronal phenotypes by single-cell capillary electrophoresis-electrospray ionization-mass spectrometry.* Anal Chem, 2011. **83**(17): p. 6810-7.
39. Swearingen, K.E., et al., *Quantification of green fluorescent protein in cellular supernatant by capillary electrophoresis with laser-induced fluorescence detection for measurement of cell death.* Talanta, 2010. **81**(3): p. 948-53.
40. Dimmeler, S., et al., *Activation of nitric oxide synthase in endothelial cells by Akt-dependent phosphorylation.* Nature, 1999. **399**(6736): p. 601-5.
41. Jiang, J., et al., *Real-time expression profiling of microRNA precursors in human cancer cell lines.* Nucleic Acids Res, 2005. **33**(17): p. 5394-403.
42. Wernig, M., et al., *In vitro reprogramming of fibroblasts into a pluripotent ES-cell-like state.* Nature, 2007. **448**(7151): p. 318-U2.
43. Sampaolesi, M., et al., *Mesoangioblast stem cells ameliorate muscle function in dystrophic dogs.* Nature, 2006. **444**(7119): p. 574-579.
44. Sun, X., et al., *Determination of ascorbic acid in individual rat hepatocyte by capillary electrophoresis with electrochemical detection.* J Chromatogr B Analyt Technol Biomed Life Sci, 2008. **870**(1): p. 46-50.
45. Zhao, S., X. Li, and Y.M. Liu, *Integrated microfluidic system with chemiluminescence detection for single cell analysis after intracellular labeling.* Anal Chem, 2009. **81**(10): p. 3873-8.
46. Schneiter, R., et al., *Electrospray ionization tandem mass spectrometry (ESI-MS/MS) analysis of the lipid molecular species composition of yeast subcellular membranes reveals acyl chain-based sorting/remodeling of distinct molecular species en route to the plasma membrane.* J Cell Biol, 1999. **146**(4): p. 741-54.
47. Meetani, M.A., et al., *Desorption electrospray ionization mass spectrometry of intact bacteria.* J Mass Spectrom, 2007. **42**(9): p. 1186-93.
48. Zimmerman, T.A., S.S. Rubakhin, and J.V. Sweedler, *MALDI mass spectrometry imaging of neuronal cell cultures.* J Am Soc Mass Spectrom, 2011. **22**(5): p. 828-36.
49. Moss, D.A., M. Keese, and R. Pepperkok, *IR microspectroscopy of live cells.* Vibrational Spectroscopy, 2005. **38**(1–2): p. 185-191.
50. Notingher, I. and L.L. Hench, *Raman microspectroscopy: a noninvasive tool for studies of individual living cells in vitro.* Expert Rev Med Devices, 2006. **3**(2): p. 215-34.
51. Delhaye, M. and P. Dhamelincourt, *Raman Microprobe and Microscope with Laser Excitation.* Journal of Raman Spectroscopy, 1975. **3**(1): p. 33-43.

52. Puppels, G.J., et al., *Studying single living cells and chromosomes by confocal Raman microspectroscopy.* Nature, 1990. **347**(6290): p. 301-3.
53. Ye, J., et al., *Determination of Penetratin Secondary Structure in Live Cells with Raman Microscopy.* Journal of the American Chemical Society, 2009. **132**(3): p. 980-988.
54. Chan, J.W. and D.K. Lieu, *Label-free biochemical characterization of stem cells using vibrational spectroscopy.* Journal of Biophotonics, 2009. **2**(11): p. 656-668.
55. Matthews, Q., et al., *Variability in Raman spectra of single human tumor cells cultured in vitro: correlation with cell cycle and culture confluency.* Appl Spectrosc, 2010. **64**(8): p. 871-87.
56. Swain, R.J., G. Jell, and M.A. Stevens, *Non-invasive analysis of cell cycle dynamics in single living cells with Raman micro-spectroscopy.* Journal of Cellular Biochemistry, 2008. **104**(4): p. 1427-1438.
57. Notingher, I., et al., *In situ non-invasive spectral discrimination between bone cell phenotypes used in tissue engineering.* Journal of Cellular Biochemistry, 2004. **92**(6): p. 1180-1192.
58. Brown, K.L., et al., *Raman spectroscopic differentiation of activated versus non-activated T lymphocytes: an in vitro study of an acute allograft rejection model.* J Immunol Methods, 2009. **340**(1): p. 48-54.
59. Notingher, I., et al., *Spectroscopic study of human lung epithelial cells (A549) in culture: living cells versus dead cells.* Biopolymers, 2003. **72**(4): p. 230-40.
60. Puppels, G.J., et al., *Laser irradiation and Raman spectroscopy of single living cells and chromosomes: sample degradation occurs with 514.5 nm but not with 660 nm laser light.* Experimental Cell Research, 1991. **195**(2): p. 361-7.
61. Pascut, F.C., et al., *Noninvasive detection and imaging of molecular markers in live cardiomyocytes derived from human embryonic stem cells.* Biophys J, 2011. **100**(1): p. 251-9.
62. Draux, F., et al., *Raman imaging of single living cells: probing effects of non-cytotoxic doses of an anti-cancer drug.* Analyst, 2011. **136**(13): p. 2718-2725.
63. Pully, V.V., A. Lenferink, and C. Otto, *Hybrid Rayleigh, Raman and two-photon excited fluorescence spectral confocal, microscopy of living cells.* Journal of Raman Spectroscopy, 2010. **41**(6): p. 599-608.
64. Konorov, S.O., et al., *Raman microspectroscopy of live cells under autophagy-inducing conditions.* Analyst, 2012. **137**(20): p. 4662-8.
65. Hosoda, A., et al., *Detection of ER stress in vivo by Raman spectroscopy.* Biochem Biophys Res Commun, 2011. **405**(1): p. 37-41.
66. Diem, M., et al., Infrared and Raman Spectroscopy and Spectral Imaging of Individual Cells, in Infrared and Raman Spectroscopic Imaging. 2009, Wiley-VCH Verlag GmbH & Co. KGaA. p. 173-201
67. Notingher, I., Raman Spectroscopy cell-based Biosensors. Sensors, 2007. 7(8): p. 1343-1358.

68. Mariani, M.M., P.J.R. Day, and V. Deckert, Applications of modern micro-Raman spectroscopy for cell analyses. Integrative Biology, 2010. 2(2-3): p. 94-101.
69. Chan, J., et al., Raman spectroscopy and microscopy of individual cells and cellular components. Laser & Photonics Reviews, 2008. 2(5): p. 325-349.
70. Swain, R.J., et al., *Assessment of cell line models of primary human cells by Raman spectral phenotyping.* Biophys J, 2010. **98**(8): p. 1703-11.
71. Chan, J.W., et al., *Micro-Raman spectroscopy detects individual neoplastic and normal hematopoietic cells.* Biophys J, 2006. **90**(2): p. 648-56.
72. Hedegaard, M., et al., *Discriminating Isogenic Cancer Cells and Identifying Altered Unsaturated Fatty Acid Content as Associated with Metastasis Status, Using K-Means Clustering and Partial Least Squares-Discriminant Analysis of Raman Maps.* Analytical Chemistry, 2010. **82**(7): p. 2797-2802.
73. Nawaz, H., et al., *Comparison of subcellular responses for the evaluation and prediction of the chemotherapeutic response to cisplatin in lung adenocarcinoma using Raman spectroscopy.* Analyst, 2011. **136**(12): p. 2450-63.
74. Zuser, E., et al., *Confocal Raman microspectral imaging (CRMI) of murine stem cell colonies.* Analyst, 2010. **135**(12): p. 3030-3.
75. Notingher, L., et al., *In situ spectroscopic study of nucleic acids in differentiating embryonic stem cells.* Vibrational Spectroscopy, 2004. **35**(1-2): p. 199-203.
76. Schulze, H.G., et al., *Assessing Differentiation Status of Human Embryonic Stem Cells Noninvasively Using Raman Microspectroscopy.* Anal Chem, 2010. **82**(12): p. 5020-5027.
77. Notingher, I., et al., *In situ spectral monitoring of mRNA translation in embryonic stem cells during differentiation in vitro.* Anal Chem, 2004. **76**(11): p. 3185-3193.
78. Pascut, F.C., et al., *Toward label-free Raman-activated cell sorting of cardiomyocytes derived from human embryonic stem cells.* J Biomed Opt, 2011. **16**(4): p. 045002.
79. Notingher, I., et al., *In situ spectral monitoring of mRNA translation in embryonic stem cells during differentiation in vitro.* Analytical Chemistry, 2004. **76**(11): p. 3185-3193.
80. Konorov, S.O., et al., *Evidence of marked glycogen variations in the characteristic Raman signatures of human embryonic stem cells.* Journal of Raman Spectroscopy, 2011. **42**(5): p. 1135-1141.
81. Konorov, S.O., et al., *Absolute Quantification of Intracellular Glycogen Content in Human Embryonic Stem Cells with Raman Microspectroscopy.* Anal Chem, 2011. **83**(16): p. 6254-6258.
82. McManus, L.L., et al., *Raman spectroscopic monitoring of the osteogenic differentiation of human mesenchymal stem cells.* Analyst, 2011. **136**(12): p. 2471-81.
83. McManus, L.L., et al., *Assessment of an osteoblast-like cell line as a model for human primary osteoblasts using Raman spectroscopy.* Analyst, 2012. **137**(7): p. 1559-1569.

84. Gentleman, E., et al., *Comparative materials differences revealed in engineered bone as a function of cell-specific differentiation.* Nature Materials, 2009. **8**(9): p. 763-70.
85. van Manen, H.J., et al., *Single-cell Raman and fluorescence microscopy reveal the association of lipid bodies with phagosomes in leukocytes.* Proc Natl Acad Sci U S A, 2005. **102**(29): p. 10159-64.
86. KRAFFT, et al., *Identification of organelles and vesicles in single cells by Raman microspectroscopic mapping*. Vol. 38. 2005, Kidlington, ROYAUME-UNI: Elsevier. 9.
87. Uzunbajakava, N., et al., *Nonresonant Raman imaging of protein distribution in single human cells.* Biopolymers, 2003. **72**(1): p. 1-9.
88. Uzunbajakava, N., et al., *Nonresonant confocal Raman imaging of DNA and protein distribution in apoptotic cells.* Biophysical Journal, 2003. **84**(6): p. 3968-81.
89. Matthaus, C., et al., *Label-free detection of mitochondrial distribution in cells by nonresonant Raman microspectroscopy.* Biophysical Journal, 2007. **93**(2): p. 668-73.
90. Draux, F., et al., *Raman spectral imaging of single living cancer cells: a preliminary study.* Analyst, 2009. **134**(3): p. 542-8.
91. Miljkovic, M., et al., *Label-free imaging of human cells: algorithms for image reconstruction of Raman hyperspectral datasets.* Analyst, 2010. **135**(8): p. 2002-2013.
92. Chernenko, T., et al., *Label-Free Raman Spectral Imaging of Intracellular Delivery and Degradation of Polymeric Nanoparticle Systems.* ACS Nano, 2009. **3**(11): p. 3552-3559.
93. Matthaus, C., et al., *New ways of imaging uptake and intracellular fate of liposomal drug carrier systems inside individual cells, based on Raman microscopy.* Mol Pharm, 2008. **5**(2): p. 287-93.
94. Ling, J., et al., *Direct Raman imaging techniques for study of the subcellular distribution of a drug.* Appl Opt, 2002. **41**(28): p. 6006-17.
95. Meister, K., et al., *Label-Free Imaging of Metal-Carbonyl Complexes in Live Cells by Raman Microspectroscopy.* Angew Chem Int Ed Engl, 2010.
96. Fukunaga, H., et al., *Label-free biomedical imaging of hydrodynamics in single human cells.* Biomed Res, 2010. **31**(3): p. 177-81.
97. Huang, Y.S., et al., *Molecular-level investigation of the structure, transformation, and bioactivity of single living fission yeast cells by time- and space-resolved Raman spectroscopy.* Biochemistry, 2005. **44**(30): p. 10009-19.
98. Zoladek, A., et al., *Non-invasive time-course imaging of apoptotic cells by confocal Raman micro-spectroscopy.* Journal of Raman Spectroscopy, 2011. **42**(3): p. 251-258.
99. Uzunbajakava, N., et al., *Nonresonant confocal Raman imaging of DNA and protein distribution in apoptotic cells.* Biophys J, 2003. **84**(6): p. 3968-3981.
100. YAO, H., et al., *Raman spectroscopic analysis of apoptosis of single human gastric cancer cells*. Vol. 50. 2009, Kidlington, ROYAUME-UNI: Elsevier. 5.

101. Bouchier-Hayes, L., et al., *Measuring apoptosis at the single cell level.* Methods, 2008. **44**(3): p. 222-228.
102. Verrier, S., et al., *In situ monitoring of cell death using Raman microspectroscopy.* Biopolymers, 2004. **74**(1-2): p. 157-162.
103. Zoladek, A., et al., *Non-invasive time-course imaging of apoptotic cells by confocal Raman micro-spectroscopy.* Journal of Raman Spectroscopy, 2010: p. n/a-n/a.
104. Krafft, C., et al., *Studies on stress-induced changes at the subcellular level by Raman microspectroscopic mapping.* Anal Chem, 2006. **78**(13): p. 4424-4429.
105. Pascut, F.C., et al., *Non-invasive label-free monitoring the cardiac differentiation of human embryonic stem cells in-vitro by Raman spectroscopy.* Biochim Biophys Acta, 2013. **1830**(6): p. 3517-24.
106. El-Hagrasy, M.A., et al., *Discrimination of primitive endoderm in embryoid bodies by Raman microspectroscopy.* Anal Bioanal Chem, 2012. **402**(3): p. 1073-81.
107. Huang, Y.S., et al., *Molecular-level pursuit of yeast mitosis by time- and space-resolved Raman spectroscopy.* Journal of Raman Spectroscopy, 2003. **34**(1): p. 1-3.
108. Okada, M., et al., *Label-free Raman observation of cytochrome c dynamics during apoptosis.* Proc Natl Acad Sci U S A, 2012. **109**(1): p. 28-32.

Chapter 2: Theoretical considerations of Raman scattering and instrumentation design

This chapter provides an introduction to the theory of Raman scattering and introduces the theoretical consideration related to instrumentation design. The Raman effect is discussed from a classical point of view and a brief quantum mechanical description is included. The final part of this chapter describes the theoretical aspects relevant to the main components of the Raman micro-spectrometer as well as the performance characterization in terms of sensitivity, spatial and spectral resolution.

2.1 Classical and quantum mechanical theory of Raman scattering

Light scattering can be regarded as the redirection of light when electromagnetic waves interact with obstacles. As a consequence of the interaction between the sample molecules and electromagnetic waves, electrons within the molecules are disturbed periodically with the same frequency (ν_0) as the electric field of the incident wave, creating an induced electric dipole moment. This disturbance of the electronic cloud is then propagated, thereby resulting in scattered light.

The scattering processes can be classified in two categories. Elastic scattering at the same frequency (ν_0) as the incident wave is called Rayleigh or Mie-Tyndall scattering. Inelastic scattering of light at the emitted radiation has a different frequency (ν) compared to the incident light is known as Raman and Brillouin scattering.

The first theoretical predictions of inelastic scattering light were made by Smekal (1923) and were followed by the first experimental observation in 1928 by Raman and Krishnan [1] who observed a frequency shift in the spectrum of scattered light compared to incident light. This frequency shift is known today as the Raman shift and can be calculated by the formula:

$$\Delta(cm^{-1}) = 10^{-7}\left(\frac{1}{\lambda_{excitation}} - \frac{1}{\lambda_{Raman}}\right), \tag{2.1}$$

where Δ is the Raman shift, $\lambda_{excitation}$ is the wavelength of the excitation source and λ_{Raman} is the corresponding Raman wavelength

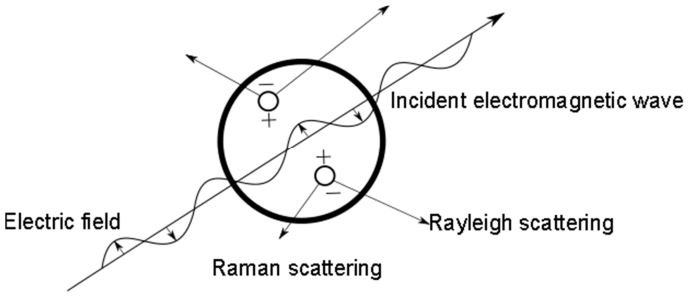

Figure 2.1 Light scattering by an induced electric dipole

In classical interpretation Raman effect can be explained by interaction of incident radiation of electric field ***E*** with a molecule. The incident electromagnetic field (figure 2.1), induces an electric dipole moment ***P***:

$$\boldsymbol{P}=\alpha\boldsymbol{E}\ , \tag{2.2}$$

where α is the electric polarizability of the molecule and ***E*** is the amplitude of electrical field corresponding to the incident electromagnetic wave. The polarizability represents an intrinsic property of the molecule and depends on the electronic structure and the nature of the chemical bonds. For non-isotropic molecules, the polarizability may vary with position and interatomic distances, and depends on the molecule symmetry. For example large atoms like Xe have high polarizability because their large electron clouds are more easily disturbed by an external electric field.

A simple qualitative description of the Raman scattering can be obtained using the classical electromagnetic theory. Consider an electromagnetic wave defined by the formula:

$$\boldsymbol{E}=\boldsymbol{E}_0\cos(2\pi\nu_0 t), \tag{2.3}$$

where ν_0 is the frequency. From equations (2.1) and (2.2), the time dependent induced electric dipole moment is:

$$\boldsymbol{P}=\alpha\,\boldsymbol{E}_0\cos(2\pi\nu_0 t) \tag{2.4}$$

Let's assume one molecule that is free to vibrate, but not rotate. The molecule is fixed in space in its equilibrium position and nuclei can vibrate around their equilibrium positions. Any disturbance in the electronic cloud caused by the incident electromagnetic wave will induce changes in the molecule polarizability. This variation of the polarizability during the vibrations of the molecule can be expressed by expanding the polarizability α in a Taylor series with respect to the coordinates x_i of vibration:

$$\alpha = \alpha_0 + \frac{\partial\alpha}{\partial x_i}x_i \tag{2.5}$$

The coordinate of vibration x_i can be written as a sinusoidal function in terms of the frequency of the vibration ν_i, the characteristic frequency of i-th normal vibrational mode and time t:

$$x_i = x_i^0\cos(2\pi\nu_i t) \tag{2.6}$$

Combining equation (2.5) with equation (2.6) yields :

$$\alpha = \alpha_0 + \alpha_1 x_i^0 \cos(2\pi \nu_i t), \tag{2.7}$$

where $\alpha_1 = \frac{\partial \alpha}{\partial xi}$ and α_0 is the initial polarizability.

The induced electric dipole moment can be expressed as:

$$\boldsymbol{P} = \alpha_0 \boldsymbol{E}_0 \cos(2\pi \nu_0 t) + \alpha_1 \boldsymbol{E}_0 \cos(2\pi \nu_0 t) \cos(2\pi \nu_i t) \tag{2.8}$$

Equation 2.8 can be rearranged using the trigonometric identity:

$$\cos a \cos b = \frac{\cos(a+b) + \cos(a-b)}{2} \tag{2.9}$$

and:

$$\boldsymbol{P} = \alpha_0 \boldsymbol{E}_0 \cos(2\pi \nu_0 t) + \alpha_1 \boldsymbol{E}_0 \frac{\cos 2\pi(\nu_0 + \nu_1)t + \cos 2\pi(\nu_0 - \nu_1)t}{2} \tag{2.10}.$$

Although equation (2.10) was obtained using the classical electromagnetic theory, it describes several important properties of Raman scattering processes. First the polarization and scattering intensity have linear dependence on the laser intensity. It also apparent that only vibrations that change the polarizability of the molecule are Raman active $\frac{\partial \alpha}{\partial x_i} \neq 0$. The changes in frequency, also known as Raman shift can be positive or negative in respect to the laser frequency. Because $\alpha_1 \ll \alpha_0$, Raman scattering is much weaker than Rayleigh scattering.

Equation (2.10) shows that light will be scattered by the molecule at three frequencies. The first term represents the Rayleigh scattering, the second term contains waves with frequencies $\nu_0 + \nu_i$ and is known as anti-Stokes Raman scattering [2] and relates the outgoing scattered photons with an increase in

frequency by an amount v_i and finally the third term v_0 -v_i, called Stokes Raman scattering is associated with a decrease in frequency of the resulting scattered photon.

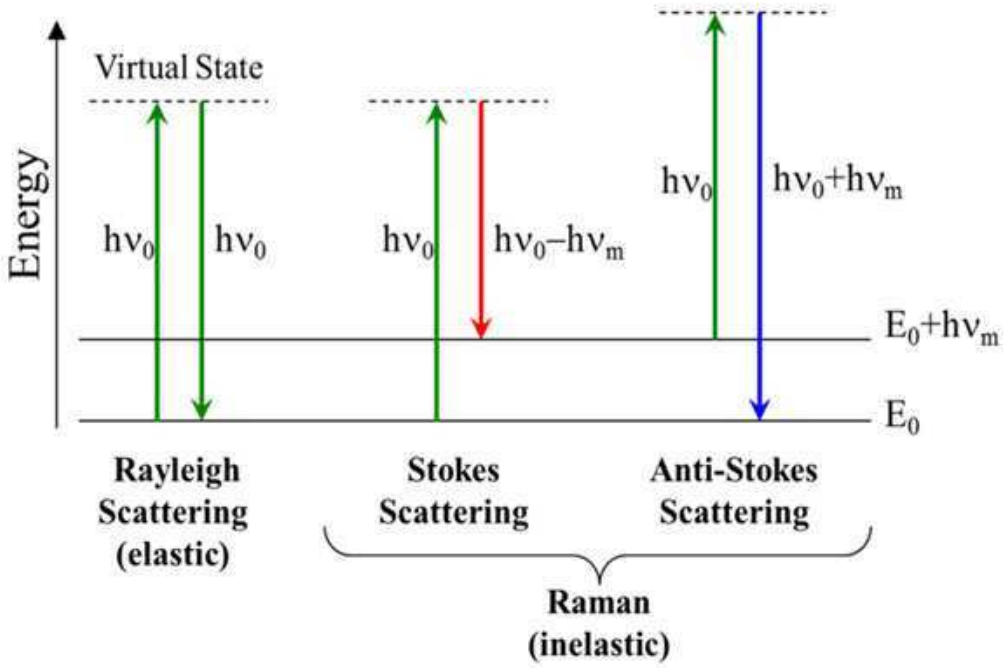

Figure 2.3 Jablonski energy diagram for Raman scattering [3]

The Stokes and anti-Stokes Raman scattering can also be explained using the Jablonski diagram (Figure 2.3). Only a small of part (10^{-6} of scattered photons) of incident of incident photon will suffer inelastic scattering. The origin of inelastic scattering can be explained in terms of energy transfer between incident radiation and scattering molecule.

The molecules situated on the ground state are excited to a virtual state followed by relaxation to a vibrational level on ground state, resulting in an energy difference lost, process known as Stoke scattering. Alternatively if the molecule is already on an excited vibrational level of the ground state, it will excite to a virtual state and relaxe back to the ground state, then the molecule will gain energy. This process is known as anti-Stokes scattering. At room temperature most of the molecules will be in the ground state, therefore it is expected that the majority of the Raman scattering will be dominated by Stokes Raman scattering. The ratio between intensities of the Stokes and anti-Stokes scattered light depends on the population of the vibrational ground and excited states and can be calculated using Boltzmann's equation [4]:

$$\frac{I_{Stokes}}{I_{anti-Stokes}} = \left(\frac{v_0 - v_i}{v_0 + v_i}\right)^4 e^{\frac{hv_i}{k_B T}} \quad , \tag{2.11}$$

where T is the absolute temperature, k_B is the Boltzman constant.

Equation 2.11 highlights the proportionality of the Raman intensity with fourth power of the frequency. In general the Raman scattering intensity can be expressed as [5]:

$$I=KI_0\alpha^2 (v_0 \pm v_i)^4, \tag{2.12}$$

where K represents a series of constants; I_0 is the intensity of the incident radiation.

The quantum theory of Raman scattering aims to explain shortcomings of classical of Raman scattering. The polarizability tensor in the classical form does not provide information related to transitional level of the scattering molecules levels or molecular rotation.

In the quantum theory the incident radiation induces a perturbation which alters the wavefunction of the molecule.

$$\Psi = \Psi^{(0)} + \Psi^{(1)} + .., \tag{2.13}$$

where $\Psi^{(0)}$ and $\Psi^{(1)}$ are zero order and first order perturbation wavefunctions. The wavefunctions can be computed from the time dependent Schrodinger and introduce into the formula of the transition electric dipole:

$$\mathrm{P_{fi}} = < \Psi_\mathrm{f} | \overline{p} | \Psi_\mathrm{i} >, \tag{2.14}$$

leading to :

$$\mathrm{P}_{fi}^{(1)} = \frac{1}{2}(\alpha)_{fi}\mathrm{E_0 e^{-i(-\omega_{fi}+\omega)t}P_{fi}} = < \Psi_\mathrm{f} | \overline{p} | \Psi_\mathrm{i} >, \tag{2.15}$$

were f and i are the subscripts to the final and initial state of transition, Ψ_f and Ψ_i are the total wave function of perturbed state in initial and final state, $\omega_{ri} = \omega_r - \omega_{i,}$ and $\omega_{i\,,}\omega_r$ is the the incident and r state angular frequency. $(\alpha)_{fi}$ is the transition polarizability tensor expressed by the formula:

$$(\alpha)_{fi} = \frac{1}{2\hbar}\sum_\mathrm{r}\left(\frac{<f|\overline{\mathrm{p}}|\mathrm{r}><r|\overline{\mathrm{p}}|\mathrm{i}>}{\omega_\mathrm{ri}-\omega_i} + \frac{<f|\overline{\mathrm{p}}|\mathrm{r}><r|\overline{\mathrm{p}}|\mathrm{i}>}{\omega_\mathrm{ri}+\omega_i}\right) \quad , \tag{2.16}$$

Qualitative discussions can be made on the frequency denominator on first term in equation (2.16). If $\omega_{ri} \gg \omega_i$, we have the situation of spontaneous Raman scattering and $(\alpha)_{fi}$ will have typical values. The resonance regime is reached when $\omega_{ri} \approx \omega_i$ where $|r>$ states will predominate and $(\alpha)_{fi}$ will be determine by the number in electronically excited states. A consequence of the resonance regime is the boost in the Raman intensity by several orders of magnitude [6] that provides the ability to probe the presence of certain analytes in smaller concentration than spontaneous regime [7]. Figure 2.4 illustrates the situation of normal and resonant Raman scattering.

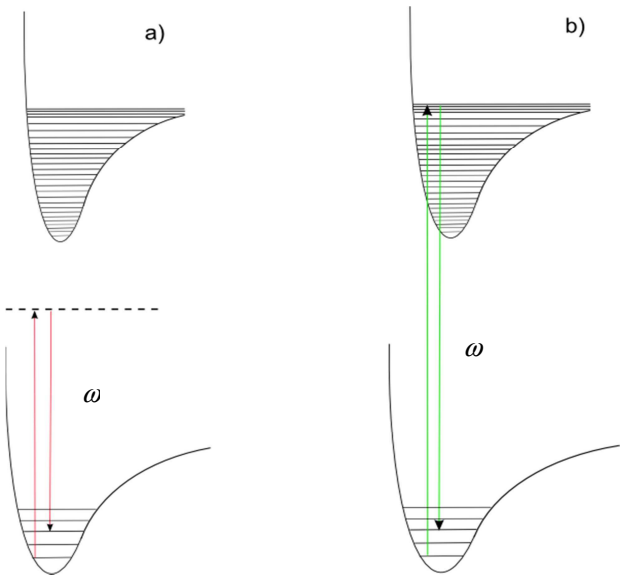

Figure 2.4 types of Raman scattering processes a) $\omega_{ri} \gg \omega$ Spontaneous Raman scattering regime b) $\omega_{ri} \approx \omega$

Also the quantum mechanics explain why some lines are forbidden based on asymmetry of the wavefunctions.

2.2 Design of the Raman micro-spectrometers

This part of the chapter describes the main design considerations to maximize the performance of the Raman micro-spectrometer for high resolution molecular imaging of cells.

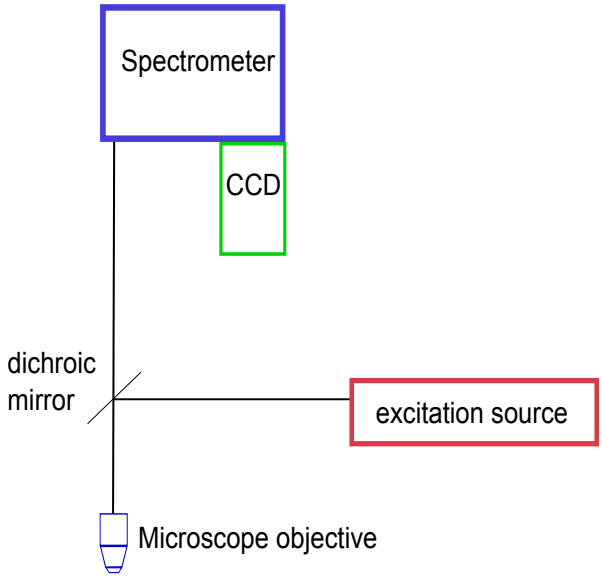

Figure 2.5 Schematic diagram of a Raman micro-spectrometer.

A typical Raman micro-spectrometer consists of five major components [4,5,8] (figure 2.5): excitation source, microscope, sample illumination and signal collection optics, wavelength analyser for the Raman scattered light, signal detection and control system.

2.3.1 Excitation source

Because the intensity of the Raman scattered light is proportional to $1/\lambda^4$, the most common lasers used in Raman spectroscopy are in the visible range of electromagnetic domain (400-660nm). Another advantage of using visible lasers is the higher quantum efficiency of the CCD detectors used for detection of the Raman scattered light. However, a drawback when using visible lasers for Raman measurements of biological samples is the higher probability to excite fluorescence emission and induce sample photo-damage [9]. Fluorescence emission can generate a large background signal that can swamp the Raman spectrum. Laser wavelength plays an important role on sample degradation. Some compounds in cells can act as photosensitizers, thus absorption of visible laser light can result in sample damage. The wavelength of the laser also provides a limit to the spatial resolution that can be achieved by a Raman micro-spectrometer. In confocal configuration the resolution in the sample plane (i.e. normal to laser beam), is [10, 11, 12]:

$$r_{x,y,confocal} \approx \frac{0.61\lambda}{N.A.}, r_{z\ confocal} \approx \frac{1.67\lambda}{(N.A.)^2} \quad (2.17)$$

where λ is the wavelength of the laser and $N.A.$ is the numerical aperture of the objective.

2.3.2 Sample illumination and signal collection

The use of optical microscope objectives allows efficient light collection in Raman spectroscopy when microscopic samples needed to be investigated. The microscope objective is a key component of a Raman micro-spectrometer and offers the possibility to focus the laser to a small spot and maximises signal collection, all within very complex, aberration corrected optical system. The selection of the microscope objective is important for maximizing the collection efficiency of the Raman scattered light and for increasing the spatial resolution, by focusing the laser to a small spot size.

A defining parameter of a microscope objective is the numerical aperture (*N.A.*), which describes system ability of an optical to gather light and is expressed by the formula:

$$N.A. = n \sin\alpha, \tag{2.18}$$

where n is the refractive index of the medium between the sample and the objective, α-is the half angle of the cone of light. For dry objectives (n=1) the maximum achievable half angle is 72^0, which yields an N.A. of 0.95 [8]. Immersion objectives are designed for higher light collection efficiency and for

observation of biological specimens through a cover slip (thickness ~ 0.17 mm) glass of different refractive index (usually 1.47). In Raman micro-spectroscopy, the water immersion objectives are preferred over oil immersion objectives because the oil give rise to a series of Raman bands that can overlap the Raman bands of the sample.

2.3.3 Wavelength analyser

Raman micro -spectrometers using visible (450-640nm) or near infrared lasers (640-900nm) are equipped with dispersive spectrometer as a spectral analyser.

The dispersive spectrometer spatially separates the Raman scattered light into light with different wavelengths that are projected simultaneously to an CCD detector located in the focal plane of the focusing mirror. Figure 2.6 shows a schematic description of a Czerny –Turner spectrometer design used in the instrument.

A Czerny-Turner spectrometer consists of two concave mirrors and a reflective diffraction grating. The Raman scattered light entering the spectrometer is collimated by the collection mirror and directed towards the reflective diffraction grating. The diffraction image is collected by the second mirror and focused on the CCD detector.

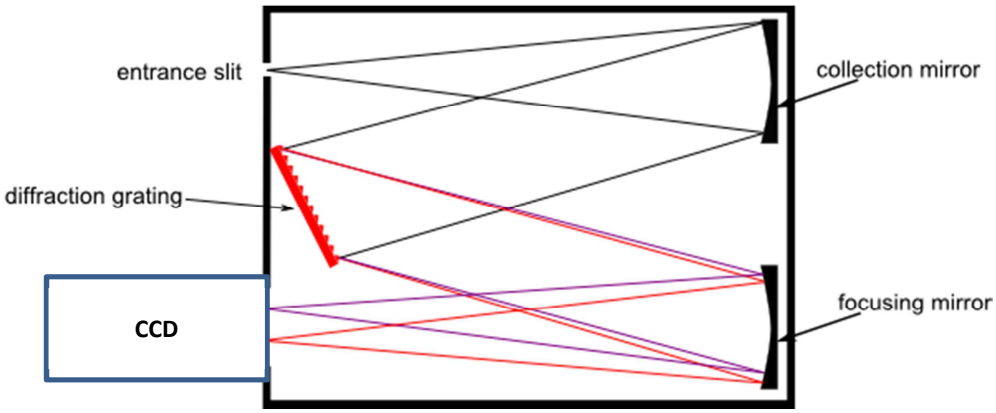

Figure 2.6 Schematic description of Czerny-Turner design for a spectrometer

The following parameters are important when choosing a spectrometer for Raman micro-spectroscopy: *f* number (*f*/#), the blaze wavelength, focal length of the mirrors and diffraction grating efficiency. The *f*/# is related to the N.A. (*f*/#=0.5 *N.A.*) and is an indicator of the light collection efficiency of the spectrometer. The flux of light (Φ) passing through the spectrometer depends on the $(f/\#)^{-2}$:

$$\Phi \propto \frac{1}{f/\#^2} \tag{2.19}$$

To maximise the optical throughput of the spectrometer it is also important to choose the most efficient diffraction grating. The efficiency of diffraction grating is defined as the percentage of the flux of light reaching the detector and depends on the wavelength of light and diffraction order in which the grating is operated. Equation 2.19 defines the corresponding blaze wavelength for which grating reaches maximum efficiency:

$$\lambda_B = \frac{2d}{m} \sin \theta_B, \tag{2.20}$$

where θ_B is the angle between the face of the grooves and the plane of grating, m is diffraction order and d is the distance between the grooves.

Linear dispersion describes the spread of the wavelength domain within the plane of focusing mirror. The linear dispersion is defined by the formula [4]:

$$\frac{\mathrm{d}\lambda}{\mathrm{d}x} = \frac{\cos \beta}{knf}, \tag{2.21}$$

where β is the angle of the diffracted light corresponding to wavelength λ, f is the focal length of focusing mirror, k is the diffraction order and n is groove density of the grating. The linear dispersion is influenced by the focal length and/or groove density of the diffraction grating (Equation 2.21). Higher dispersion (smaller dλ/dx) implies better spectral resolution, which results in increased spread-out of the spectral domain on the CCD. However this will lead to smaller spectral coverage by the CCD.

2.3.4 Detector

The CCD (charged couple device) is the preferred detectors for low light applications such as Raman spectroscopy. The CCD is a photosensitive silicon device which stores and manipulates the electrical charge for conversion into a

digital value. The selection of the CCD detectors depends on the laser wavelength used for excitation of the Raman scattering and the characteristics of the spectrometer type and will determine the sensitivity, spectral coverage, and speed of the acquisition. The parameters which are influencing the CCD performances are: CCD format, quantum efficiency, readout noise, dark current and dynamic range. Dark current is a process of generation of random electron/hole pairs in semiconductor devices. The noise caused by the dark current overlaps with much weaker Raman bands. To limit the effect of the dark current the CCD has to be cooled to low temperatures (>60 ^{0}C). Cosmetic defects such as dead pixels, charge traps or silicon imperfection can affect the overall performances of the CCD detectors.

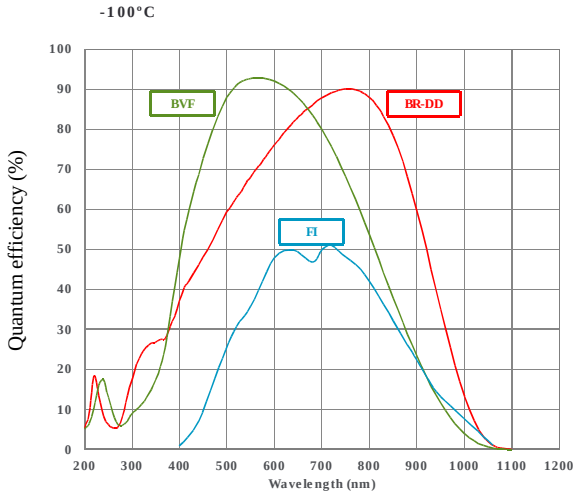

Figure 2.7 Quantum efficiency curves of CCD detectors used in Raman micro-spectroscopy [13]

The quantum efficiency curve (QE) represents the probability to detect a photon at a certain wavelength and affect the signal to noise ratio of the Raman spectra in spectral domain of interest (Figure 2.7). Selection of laser wavelength will determine the corresponding wavelength domain of the Raman shift range on the quantum efficiency curve. Thus the sensitivity of the detection can be improved if the fingerprint region of the Raman shift overlaps with the region of maximum quantum efficiency of the CCD detector.

References:

1. Raman, C.V. and K.S. Krishnan, *A New Type of Secondary Radiation.* Nature, 1928. **121**: p. 501-502.

2. Turrell, G., *1 - The Raman Effect, in Raman Microscopy*, T. George and C. Jacques, Editors. 1996, Academic Press: London. p. 1-25.

3. http://bwtek.com/raman-theory-of-raman-scattering/. *Jablonski Energy Diagram for Raman Scattering*. Raman Tutorial.

4. McCreery, R.L., *Raman Spectroscopy for Chemical Analysis*. 2005: Wiley.

5. Smith, E. and G. Dent, *Modern Raman Spectroscopy: A Practical Approach*. 2005: Wiley.

6. Czernuszewicz, R.S. and M.B. Zaczek, *Resonance Raman Spectroscopy, in Encyclopedia of Inorganic and Bioinorganic Chemistry*. 2011, John Wiley & Sons, Ltd.

7. Okada, M., et al., *Label-free Raman observation of cytochrome c dynamics during apoptosis*. Proc Natl Acad Sci U S A, 2012. **109**(1): p. 28-32.

8. Turrell, G. and J. Corset, *Raman Microscopy: Developments and Applications*. 1996: Elsevier Science.

9. Puppels, G.J., et al., *Laser irradiation and Raman spectroscopy of single living cells and chromosomes: Sample degradation occurs with 514.5 nm but not with 660 nm laser light*. Experimental Cell Research, 1991. **195**(2): p. 361-367.

10. Diaspro, A., *Confocal and Two-Photon Microscopy: Foundations, Applications and Advances*. 2001: Wiley.

11. Hawkes, J.F.B. and I. Latimer, *Lasers: Theory and Practice*. 1995: Prentice Hall PTR.

12. Siegman, A.E., *Lasers*. 1986: University Science Books.

13. Andor, *iDus 401 Series.*

Chapter 3: Development and characterization of the Raman spectrometer

This chapter describes the design, development and characterization of a Raman micro-spectrometer optimised for cell imaging. The first part of the chapter discusses the practical aspects and the design considerations, laser stability tests and spectral resolution. The last part of the chapter presents examples of Raman spectral maps of endothelial cells obtained with the instrument.

3.1 Optical design: general considerations

The schematic description of the Raman micro-spectrometer is presented in Figure 3.1.

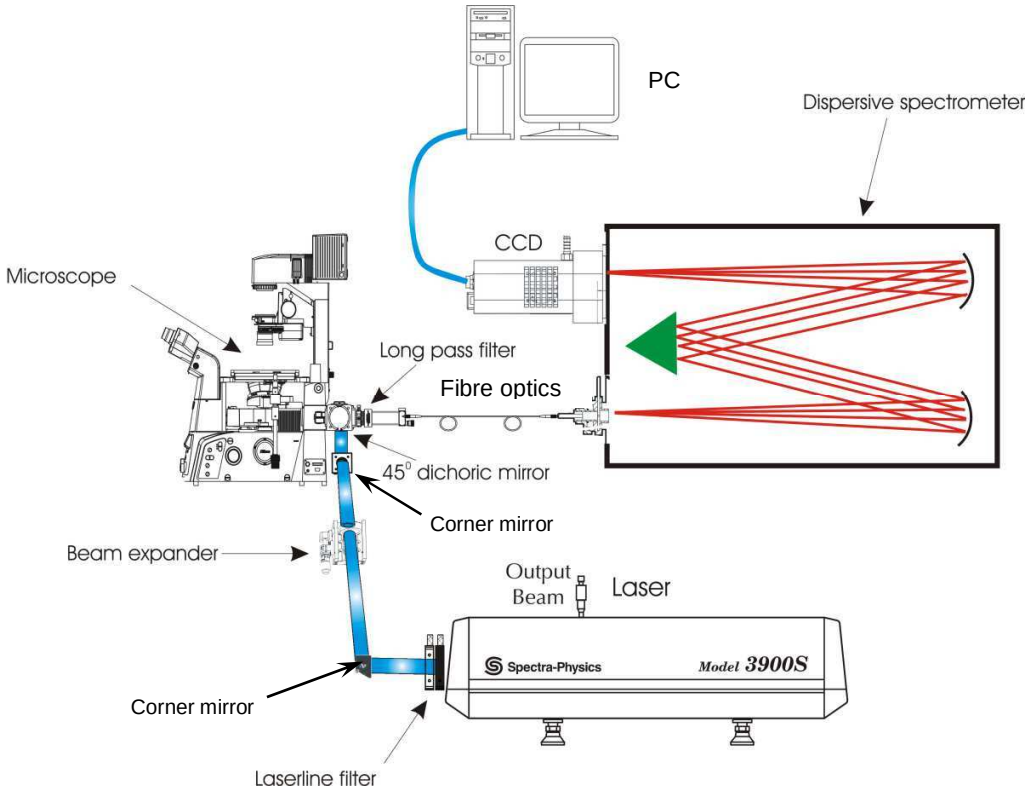

Figure 3.1 MicroRaman system design

Raman scattering is excited by a continuous waveform (CW) Ti:saphhire laser (Spectra Physics 3900S) tuned at 710 nm, which is focused on the sample by a 60× water immersion microscope objective (UPLSAPO 60xw -1.2 N.A., Olympus).

The laser has a high beam quality ($M^2 < 1.1$) that allows the beam to be focused to a diffraction limited spot. The laser beam was expanded to fill the pupil of the microscope objective (diameter of 7mm) to obtain a laser spot of 0.48 µm. The diameter of the laser spot was calculated using formula: $4 \lambda M^2 f/\pi D$, where f is the focal length of the microscope objective and D is the diameter of the back entrance of the microscope objective.

For comparison alternative laser diodes used in commercial instruments have typical beam quality of M^2=1.7. Such lasers focused using the same microscope objective will yield a focal a spot diameter of 0.7 µm. The wavelength of the selected excitation can be tuned in the range of 700 – 1000 nm. The tradeoff between laser wavelength and live cell photo-damage has been discussed in the previous chapter (excitation source section 2.3.1). The shortest near infrared wavelength available for this laser, 700 nm is sufficient to avoid cell damage [1, 2] while still providing Raman scattering matching the sensitivity curve of the detector. The Ti:sapphire gain medium does not degrade over time, providing stability to the instrument.

A laser line filter is mounted in front of the Ti:sapphire laser to cut off the secondary emissions to prevent the distortion of the measuremed signal. After passing the laser line filter, the beam is expended to fill up the back entrance of the microscope objective. The 45^0 dichroic mirror redirect the expanded laser inside the microscope objective. Apart from microscope objective, the spatial resolution achieved by Raman micro-spectrometer depends also on the beam properties of the laser.

The Raman scattered light is collected by the same objective and is focused onto an optical fibre which acts as an efficient replacement for the pinhole in a conventional confocal microscope. The optical fibre is connected to a dispersive spectrometer (77200, Oriel, Newport) equipped with a 1000 lines/mm ruled diffraction grating blazed at wavelength 900nm. The Raman scattered light is then focused on a thermally cooled back illuminated deep depletion CCD (DU401A Andor Technology).

The selection of the components used for the Raman micro-spectrometer is discussed in detail having in consideration the main design factors: maximize collection of the Raman scattered light, maximize spatial resolution, minimize damage to live cells. Transmission (Figure 3.2) and numerical aperture of the microscope objective influence the collection efficiency of the Raman photons, thus the signal-to-noise ratio of the spectra can be improved by choosing an objective with high transmission and N.A..

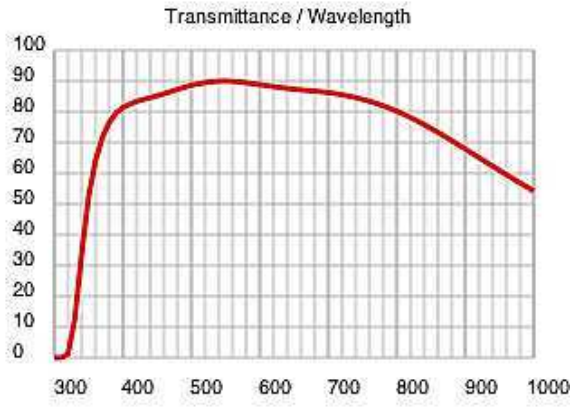

Figure 3.2 Transmission curve for the UPLSAPO 60xw used for the Raman micro-spectrometer [3].

An optimized Raman micro-spectrometer will transmit the collected light flux from the microscope objective to detector via the intermediary optics and spectrometer.

The coupling of the microscope objective with spectrometer will involve using intermediary optics, selected to match the numerical aperture of the microscope objective and spectrometer (Figure 3.3). If we know the parameters of the microscope objective and spectrometer, we can compute the focal length of the focusing in the optical fibre.

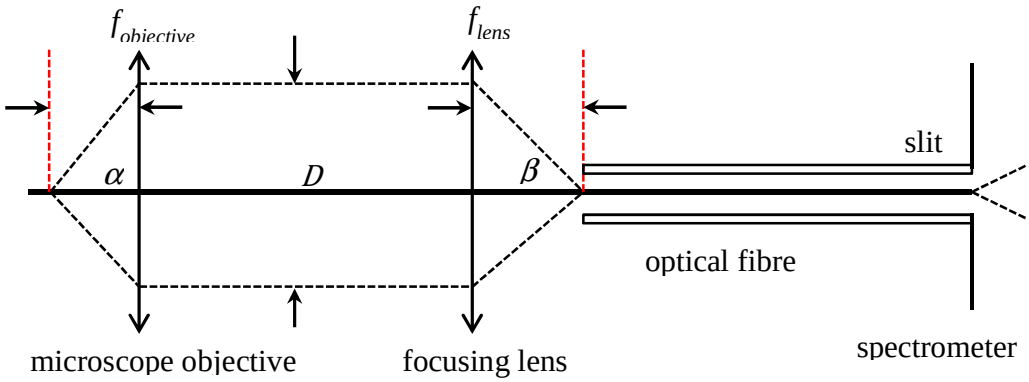

Figure 3.3 Optical coupling for the Raman micro-spectrometer. *D* is the diameter of the back pupil of the microscope objective and $f_{objective}, f_{lens}$ are the focal lengths microscope objective and focusing lens

The numerical aperture of the focusing lens is:

$$N.A. = n_{air} \sin \beta \tag{3.2}$$

From Figure 3.2 the collection angle β of the lens by using tan formula in figure 3.2:

$$\tan\alpha = \frac{2f_{lens}}{D}. \tag{3.3}$$

Thus the numerical aperture of the focusing lens can be expressed by the following formula:

$$\tan(\sin^{-1}(N.A._{lens})) = \frac{D}{2f_{lens}} \tag{3.4)}$$

The diameter D can be related to the collection angle and focal length of the microscope objective by $D = 2f_{objective}\tan\alpha$ and

$$\alpha = \sin^{-1}\left(\frac{N.A._{objective}}{n_{immersion}}\right) \tag{3.5}$$

Therefore using equations 3.5 and 3.5 the optimised focal length of the lens is:

$$f_{lens} = \frac{f_{objective}\tan\left(\sin^{-1}\left(\frac{N.A._{objective}}{n_{immersion}}\right)\right)}{\tan(\sin^{-1}(N.A._{lens}))} \tag{3.6}$$

Using the parameters of the selected microscope objective $N.A._{objective}$=1.2, $n_{immersion}$=1.33, $f_{objective}$=3.33 mm, a pupil diameter of D=7 mm, the numerical aperture of the lens has to match the numerical aperture of the spectrometer $N.A._{lens}$=0.12, the resulting focal length of the lens is f_{lens}=30 mm.

Because elastic scattering is several orders of magnitude higher than Raman scattering, an effective filtering of Rayleigh scattering is required to prevent laser light entering the spectrometer.

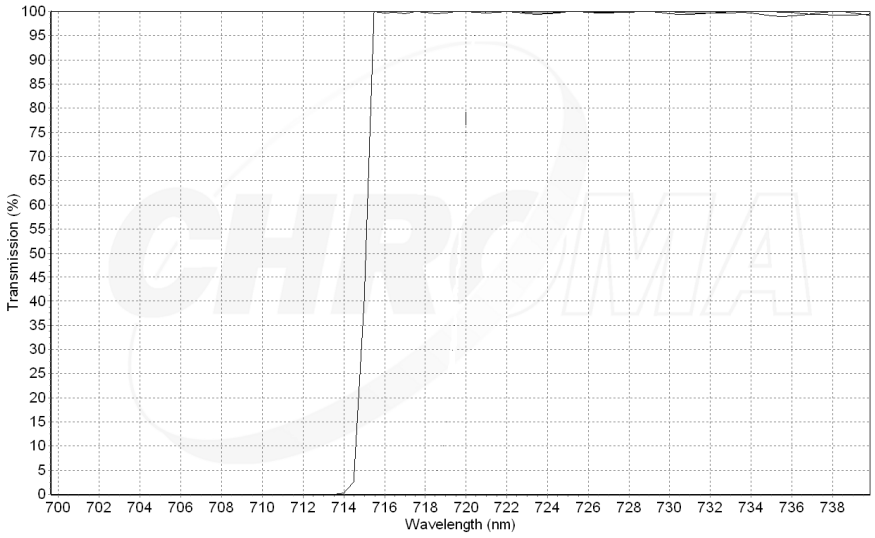

Figure 3.4 Transmission curve for the long pass filter used to block the Rayleigh scattering [4]

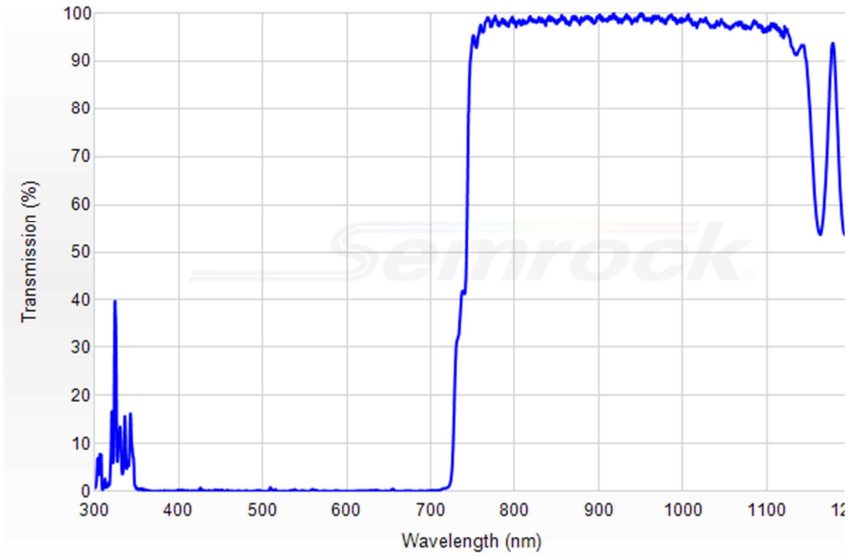

Figure 3.5 Transmission curve for the FF-735 450 dichroic mirror [5]

Stray light can give rise to a high background that can cover the entire Raman spectrum. For this instrument, the filtering was implemented using a long pass edge filter (Figure 3.4) along with a high transmission 45^0 dichroic mirror (Figure 3.5).

3.2 Laser wavelength and power stability

Laser wavelength stability

As the Raman shifts represent the difference between two frequencies (laser and Raman scattered photons), any change in laser frequency (or wavelength) will be recorded as an error in the final Raman spectra.

Thus the stability of the laser wavelength was evaluated on short term (eight hours) and long term (five days) experiments. The short period experiment is important to characterize the stability for typical experiments carried out on single day. The long term wavelength stability experiment is relevant for the measurements which require extensive period of time and consist of five days observation of the laser wavelength. The position of the lenses, mirror and grating was not altered to ensure stability of instrument during the experiments and evaluate the spectral errors due to errors in the laser wavelength. The measurements were done at constant room temperature of 20^0 C to prevent any changes in temperature with more than $\pm 3^0$C as recommended by the laser manufacturer.

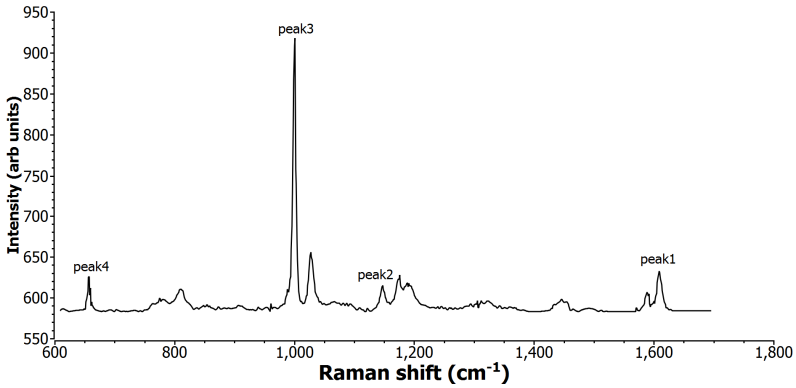

Figure 3.6 Raman spectra of polystyrene. The peaks taken into consideration for wavelength stability tests are labelled.Peak1 is assigned to benzene ring stretching, peak 2 to in-plane CH deformation, peak 3 to CH deformation, and peak 4 to in-plane benzene ring deformation

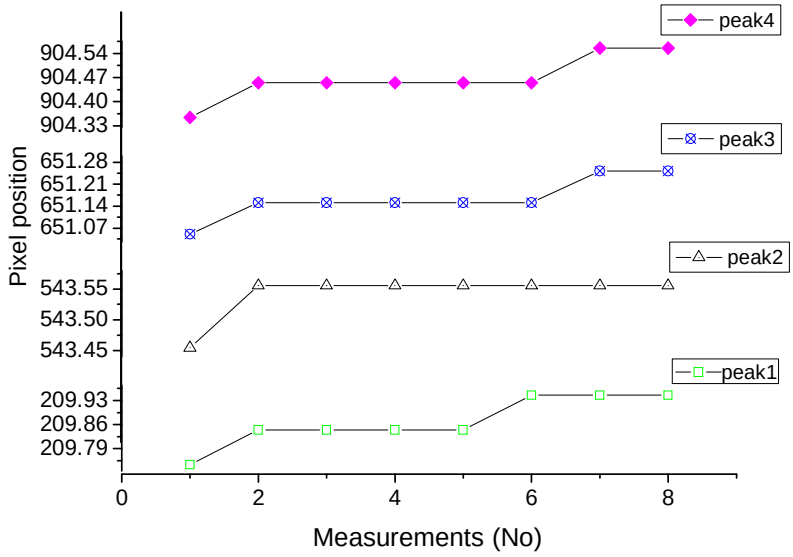

Figure 3.7 present the position of the selected Raman measured at 1 hour intervals over total of 8 hours. Peak1 to peak4 position (pixel number) vs time

For both short and long term stability tests, Raman spectra of a polystyrene sample were recorded at different time points and Raman shift of several peaks of polystyrene were analysed.

The pixel position obtained from the peak fit software in Matlab is obtained in decimal numbers. Figure 3.7 shows that the positions of the selected Raman bands change by less than one pixel (0.25 pixel units) over 8 hours, which correspond to a Raman shift error of 0.28 cm^{-1}. This value is below the spectral calibration accuracy of the spectrometer (± 0.5 cm^{-1}) when using ASTM standard (Tylenol and 1,4 BSMB) and cannot influence the data analysis.

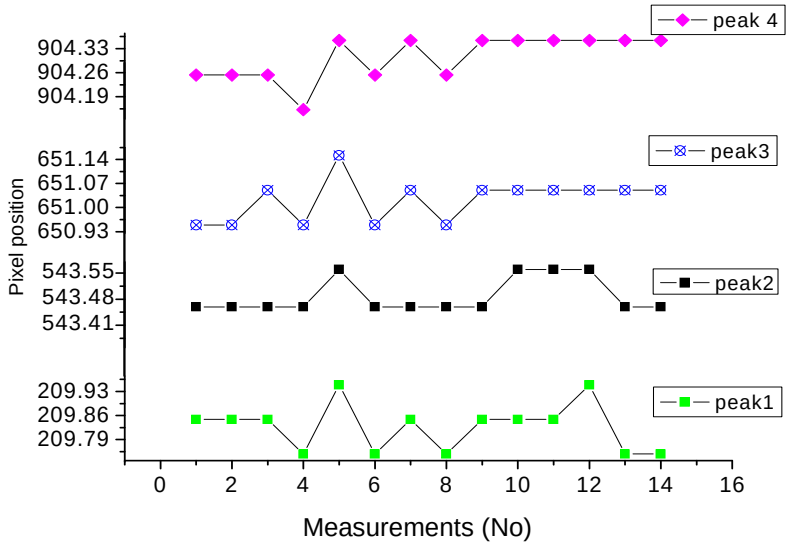

Figures 3.8 peak1 to peak4 position (pixel number) vs measurements covering five days time.

For the long term experiment, measurements were taken on different times of the day over a period of five days. The same analysis technique was used as in short term experiment. The peak positions for the selected Raman bands are shown in the figure 3.8. The calculated laser drift with is 0.3 pixel numbers with 99.7% confidence which is equivalent to a laser wavelength error for the Raman shift of 0.33 cm^{-1}.

Again this value is below the spectral accuracy of the spectrometer. The long term stability of the laser wavelength indicates that the laser is suitable for Raman experiments over longer period of time such as measurements of large numbers of cells and long-time course experiments.

Power Stability

Major fluctuations of the laser power can lead to changes in the number of photons recorded by the CCD camera and can be misinterpreted as a change in concentrations of the analytes. To ensure that laser is for suited cell measurements, the power stability of the laser was tested over several hours (power-meter PM 100D, Thorlabs, UK). In this experiment the output power of the laser was chosen to match the intended power that will be normally used for cell measurements. Figure 3.9 shows the variation over time of the laser power. The average value of the laser power within seven hours measurement interval was 321 mW with the standard deviation 2.4 mW.

For typical Raman peak in spectrum of a cell (120 counts), the power drift of 2.24% represents an error in the intensity of only two counts which is bellow the readout noise of the CCD.

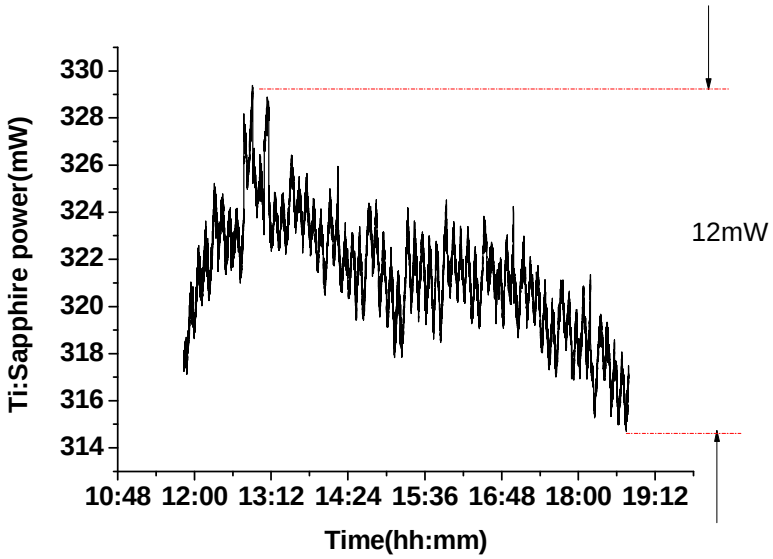

Figure 3.9 Ti:Sapphire laser output power vs time

3.3 Spectrometer throughput and resolution

The spectrometer used for the Raman micro-system is a 77200 monochromator from Oriel Newport spectra Physics in Czerny Turner configuration (figure 3.10 b). This spectrometer has a focal length of 250 mm, *f*/4.4, and contains a plane ruled diffraction grating with a groove density of

1000lines/mm (53-*-701R, Richardson gratings, Newport Spectra Physics). The blaze wavelength of the grating is 900 nm and is suitable for measurements of Raman spectral lines in the region 750-800nm. The choice of the grating was dictated by few requirements: spectral resolution, spectral coverage and blaze efficiency (figure 3.11).

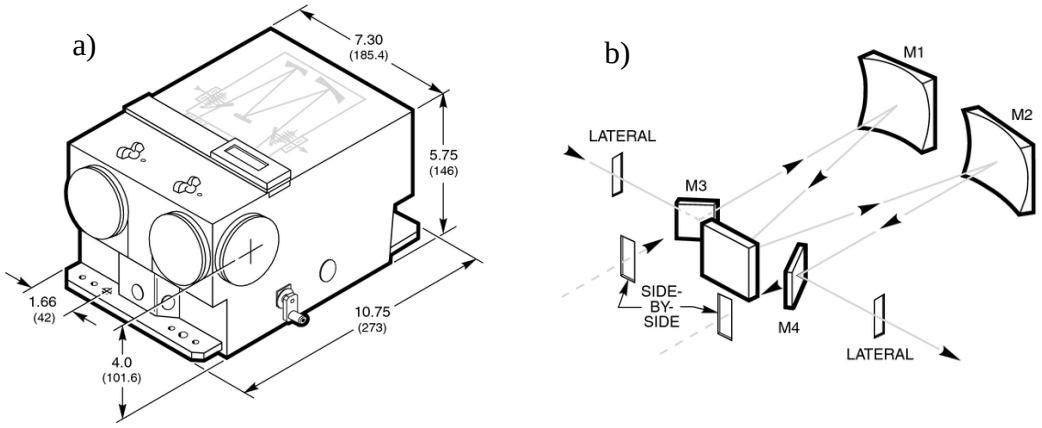

Figure 3.10 a) 77200 1/4 m focal length monochromator b) optical system for the 77200 monochromator

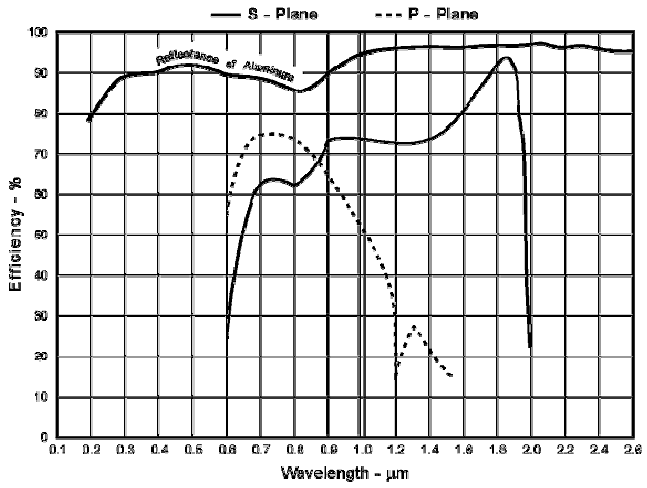

Figure 3.11 Blaze efficiency curve of the diffraction grating inside the selected Oriel spectrometer

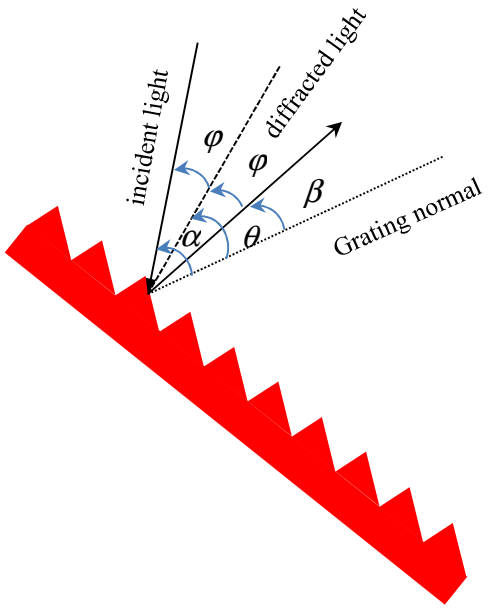

Figure 4.12 Drawing of the diffraction grating used in the first order. φ is the constant deviation angle, θ is the rotation angle of the grating, α is the incidence angle and β is the diffraction angle.

To increase the efficiency of the diffraction grating for a specific diffraction order, it is possible to design the grating to reduce the light scattered in other diffraction order. For the diffraction grating used in this spectrometer the number of available diffraction orders can be calculated:

$$\sin\alpha+\sin\beta=nk\lambda \tag{3.7}$$

with

$$\alpha=\theta+\varphi \tag{3.8}$$

and

$$\beta_k = \theta - \varphi, \tag{3.9}$$

where β_k is the diffraction angle for given diffraction order k and n is the groove density.

For the selected grating, n=1000lines/mm, k=-1, and φ=13.04, λ=800nm, the resulting incidence angle and the grating angles corresponding to the -1 diffraction order are: α=-11.16 and β_1=-37.27. Using the equation 3.7, 3.8 and 3.9 the second diffraction order is:

$$\sin(-11.16) + \sin \beta_2 = 1.6 \tag{3.10}$$

Which correspond to sin β_2=-1.4. This result shows that the second order of diffraction is physically impossible and the grating will provide maximum efficiency in the 1st order.

The performance of the Oriel spectrometer based on the optimised diffraction grating was compared with the Andor Shamrock used previously in the system.

For these experiments was used the laser wavelength of 785 nm and the same condition were used: CCD detector (Andor DU401A), and microscope objective, dry 50×, 0.75 N.A. (Nikon, Japan). The Andor spectrometer has a focal length of 303 mm, a plane ruled grating with groove density of 830 l/mm and a 820 nm blaze wavelength.

The Raman spectra of polystyrene measured using the two Raman spectrometers are shown in Figure 3.12. The same acquisition time and laser power

was used for both measurements. The relative intensity of the Raman peaks obtained after background subtraction was $I_{Oriel}/I_{Andor=}1.38$. This result shows that the optimised Oriel spectrometer was 27% more efficient than the standard Andor spectrometer used in previous studies [6].

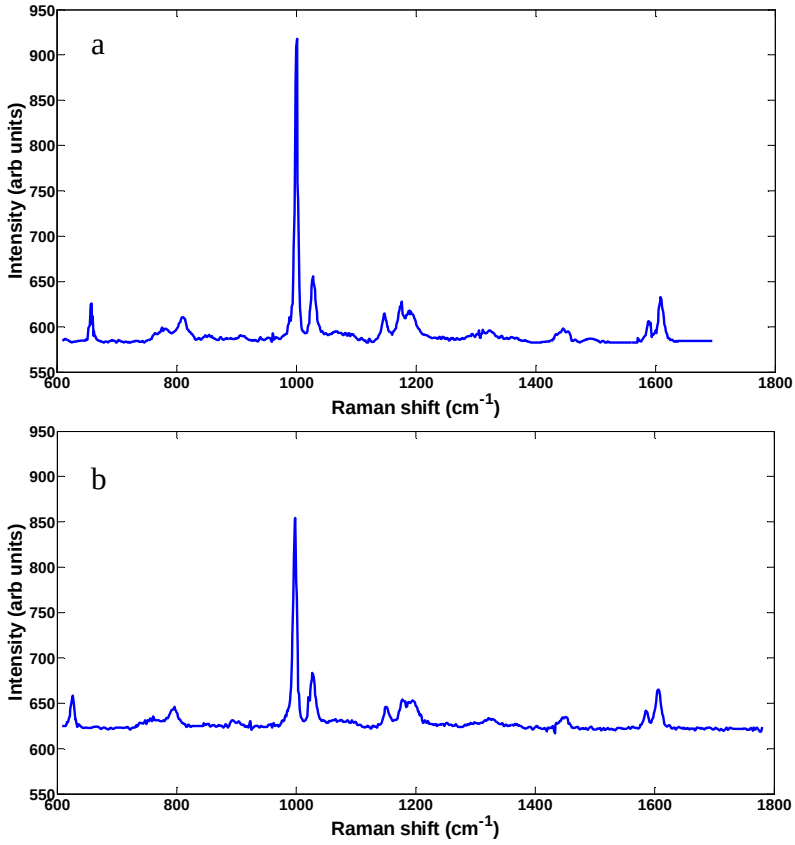

Figure 3.12 Raman spectra of polystyrene measured using: Oriel spectrometer a) and Andor spectrometer b)

Spectral resolution

The spectral resolution of the Oriel spectrometer was measured using standard Hg calibration lamp coupled to the spectrometer with an optical fibre. The peaks of the calibration lamp are shown in Figure 3.13. The overall spectral resolution was calculated as the mean of the FWHM values of the peaks over the entire spectrum.

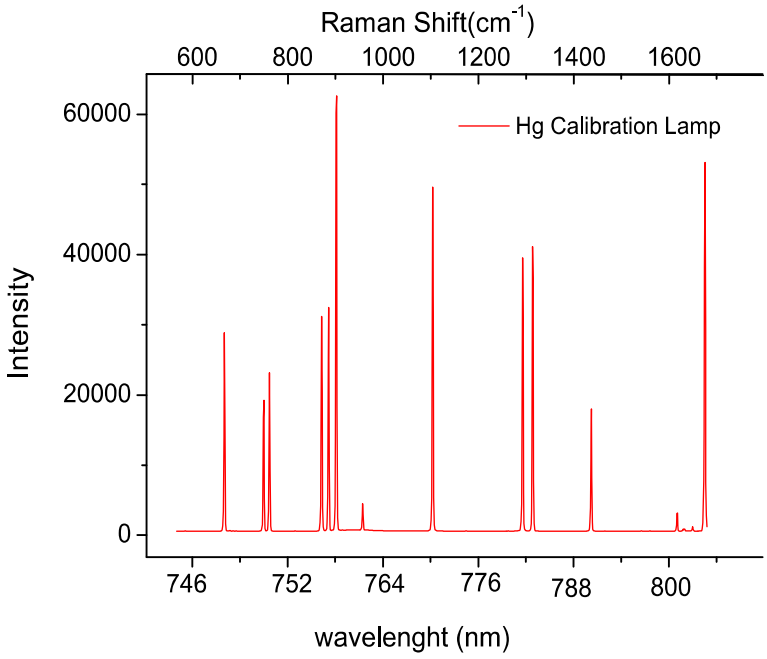

Figure 3.13 Emission spectrum of the calibration lamp measured with the Oriel spectrometer

The analysis showed that spectral resolution of the spectrometer was 2.3 cm^{-1}. This result indicate that the spectral resolving power of the spectrometer is similar to

other instruments used in studies using Raman micro-spectrometer for molecular imaging of cells [6].

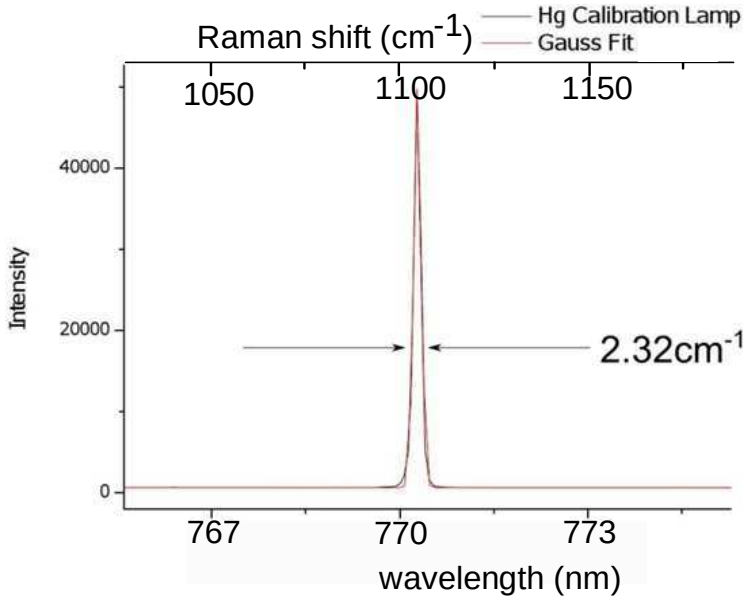

Figure 3.14 Fit for a typical spectral peak of the Hg calibration lamp

3.4 Evaluation of signal to noise ratio (SNR) of the Raman spectra as function of laser wavelength

Most of the Raman micro-spectrometers available for cells measurements use laser diodes at 785 nm wavelength. This type of laser is a good compromise between price, wavelength stability and beam quality. Given the popularity of these lasers, there is wide offer of laser-line filters, long-pass filters and dichroic mirrors that can be used for Raman spectroscopy. However because the Raman intensity is

proportional to λ^{-4} tuning the wavelength of Ti:sapphire laser at 710 nm should lead to increase in the signal by a factor of 1.5×.

Although the 700 nm wavelength was available, this selection was restricted by the availability of filters (laser line, dichroic mirror, long pass filter). To compare the performances of the instrument when the laser wavelength was set to 710 and 785 nm, Raman spectra of polystyrene samples were measured at these two wavelengths using an objective 50× 0.75 N.A., 275 mW (Figure 3.15).

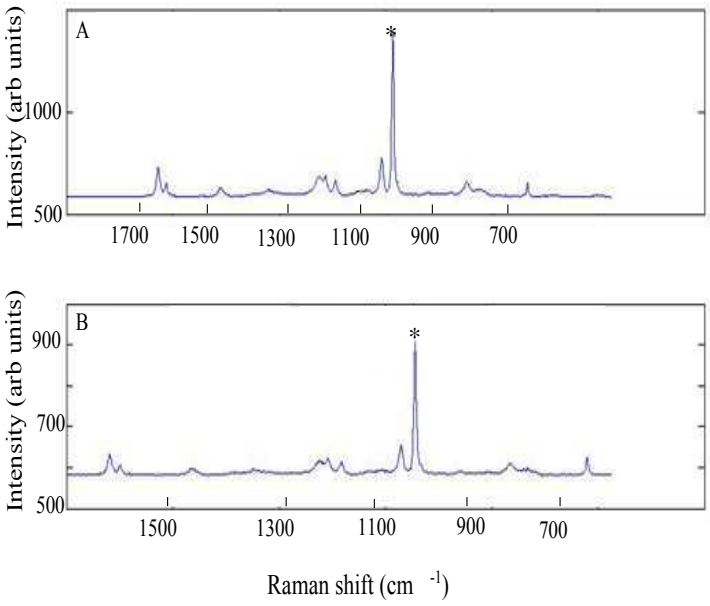

Figure 3.15 Raman spectra of polystyrene measured two distinct wavelengths using: A) 710nm B) 785nm. The (∗) symbol indicates the Raman bands used for comparison of signal intensity

The ratio of the intensity several Raman bands was calculated to be 1.54, slightly larger than theoretical prediction. It is worth mentioning, that the quantum efficiency of the CCD detector and the transmission of the microscope objective are higher in the region corresponding to 710 nm excitation than for 785 nm excitation. Based on this observation it is expected that overall optical performances of the Raman micro-spectrometer using 710 nm excitation wavelength to be improved, beyond λ^{-4} factor.

3.5 CCD sensitivity

In addition to the increased Raman scattering efficiency when shorter excitation wavelength is selected, tuning the laser at 710 nm offers another advantage related to the quantum efficiency of the detector. For the 710 nm excitation wavelength, the wavelength domain corresponding to the Raman fingerprint region (550-1800 cm^{-1}) is 738 - 815 nm region. The quantum efficiency curve of the Andor CCD has its peak value around 750 nm. By matching the fingerprint region with the peak region of the CCD quantum efficiency curve it is possible to increase the detection sensitivity of small Raman bands such as the bands associated the nucleic acids at 788 cm^{-1}, 813 cm^{-1} or lipids at 717 cm^{-1} (748 nm). Such improvement may be important when imaging the distribution of these bio-chemicals inside cells. When the 785 nm excitation wavelength is selected the wavelength domain corresponding to the Raman region of interest is 820-914 nm. Therefore an improvement by ≈1.17

times compared with 785 nm set-up is expected (Figure 3.16). Along with the theoretical improvement of 1.5× based on the λ^{-4} factor increase of the SNR by a factor of 1.74 can be achieved.

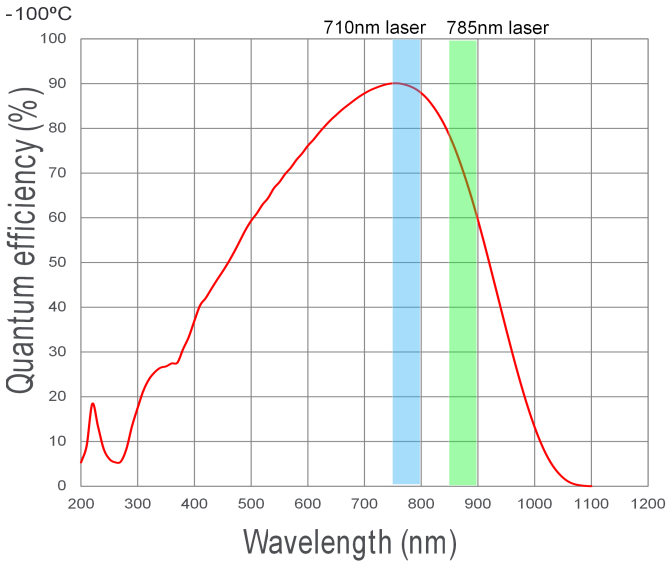

Figure 3.16 Quantum efficiency curves for the Andor CCD detector [8].

3.6 Spatial resolution versus SNR

The Raman micro-spectrometer was tested for different confocal arrangement to assess the influence of the diameter of the optical fibre used for collection of the Raman photons on the axial resolution and signal to noise ratio of

the Raman spectrum. In this design the traditional confocal pinhole was replaced with an optical fibre that can reject the out of focus signal. The Raman signal collected from the 63× Zeiss (W Plan-Apochromat 63×) microscope objective was focused onto the optical fibre by another lens.

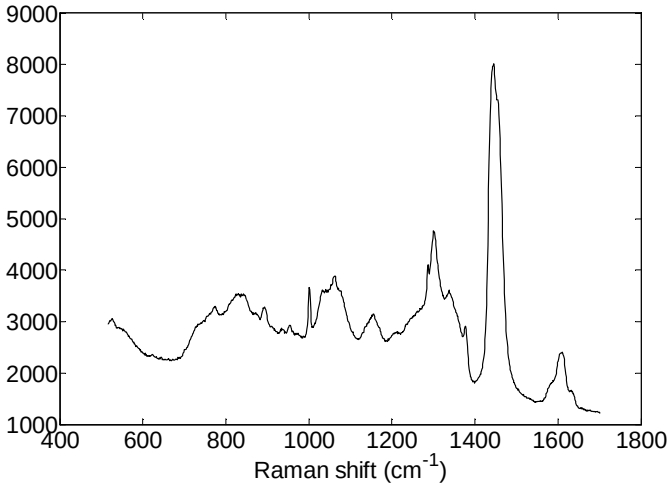

Figure 3.17 Raman spectra of oil

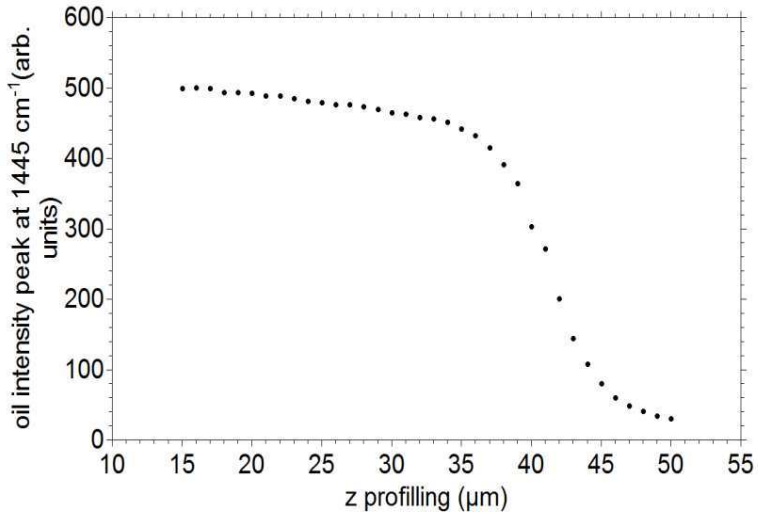

Figure 3.18 response curve for oil layer profiling

To optimise the spatial resolution and Raman intensity signal, several combinations of optical fibres and focusing lenses were tested. The diameters of optical fibres used for the measurements were 9, 20, 25 and 50 µm with 0.12 N.A matching the numerical aperture of our spectrometer. Achromatic lenses with focal length 30mm and 25mm were selected as well as 5× microscope objective (5× Zeiss A-Plan) with focal length of 30mm and 0.12 N.A. To measure the spatial resolution in the axial direction, Raman spectra of a layer of oil (Figure 3.17) on a coverslip were measured while the z position was change in steps of 1µm. The response curve (Figure 3.17) was obtained by plotting the intensity of the most intense Raman band of oil (1445 cm^{-1}).

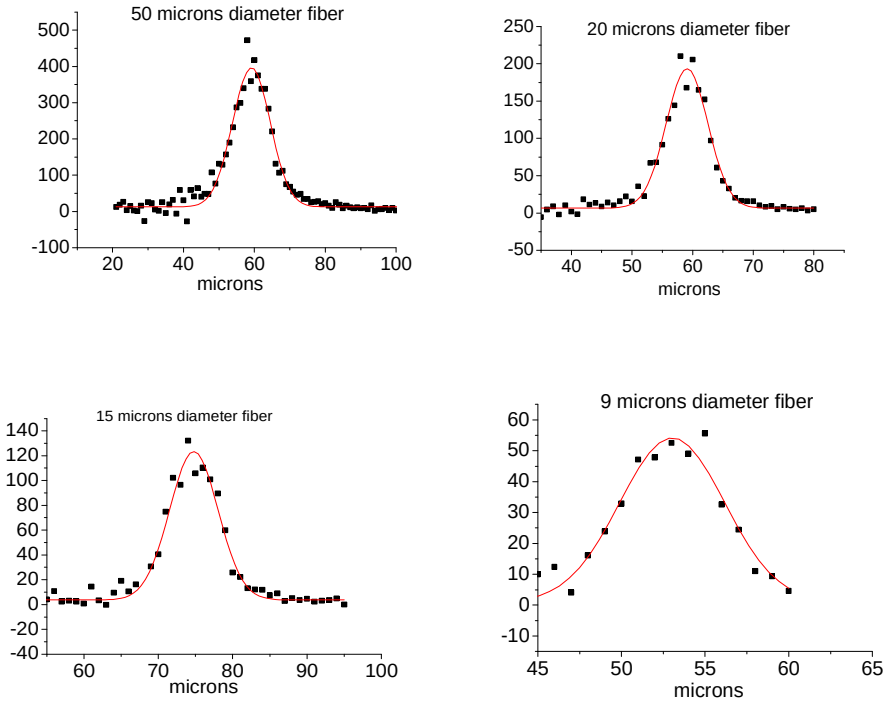

Figure 3.19 The first derivative of the response curve for optical arrangement when a 30 mm focal length lens was used for focusing the Raman light into optical fibres with diameters in the range 9-50 µm

The axial resolution of the microscope was then determined as the FWHM of the peak corresponding to the first derivative of the response curve. Figure 3.19, 3.20, 3.21 shows the first derivatives of the response curves when different lenses were used to focus the Raman signal to optical fibres with different diameters.

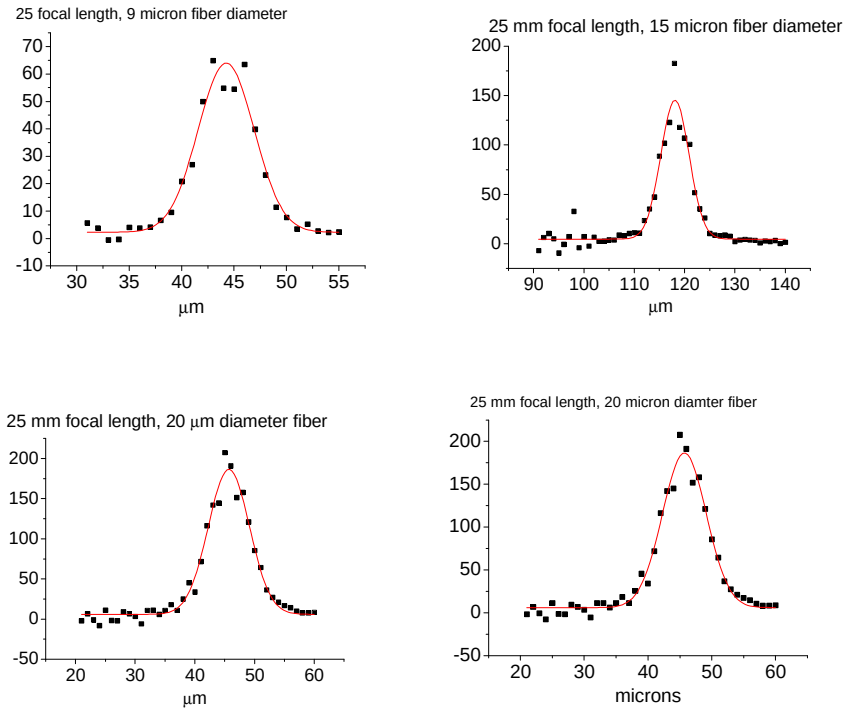

Figure 3.20 First derivative of the response curve for 25 mm focal length using different fibre diameters

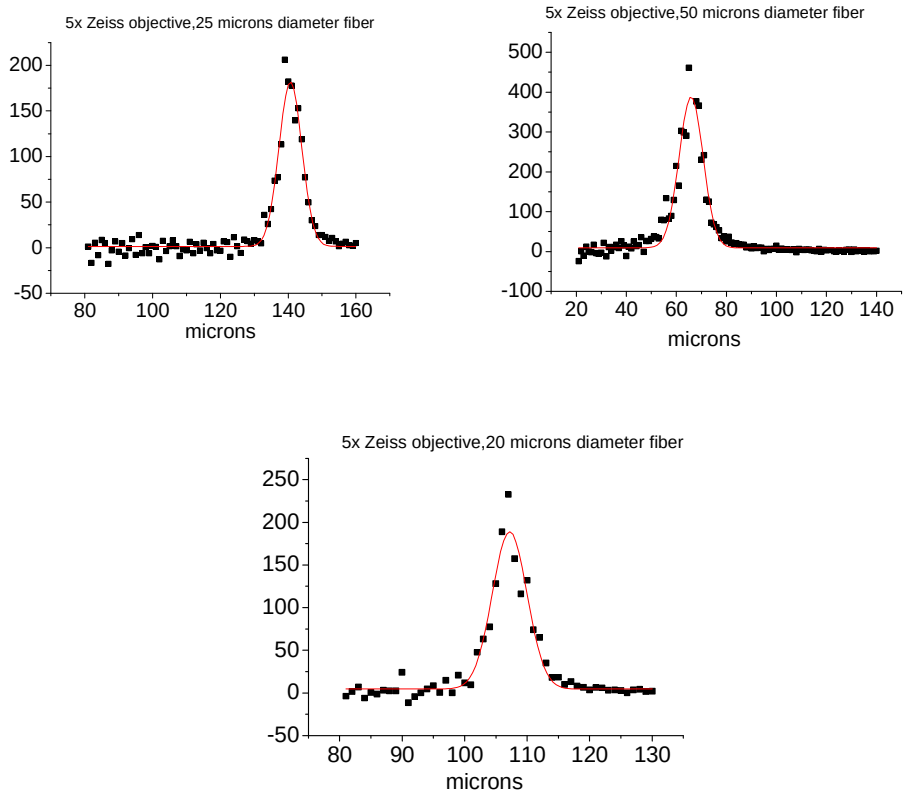

Figure 3.21 first derivative of the response curve for optical arrangement: Zeiss 63× water immersion objective and Zeiss 5× objective using different fibre diameters

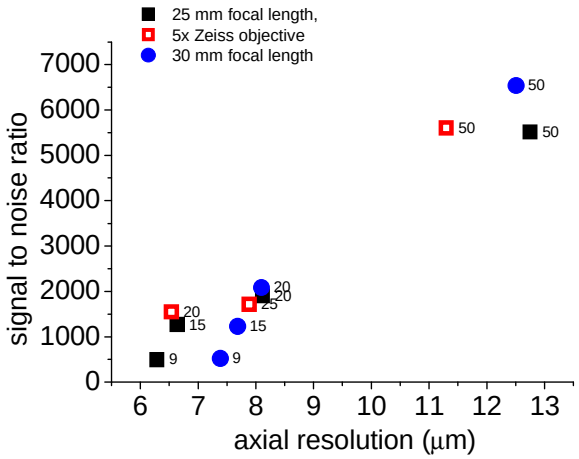

Figure 3.22 signal to noise ratio versus axial resolution for different fibre diameter with 25mm, 300mm and 5× Zeiss as a focusing lens

	Zeiss 5x objective	30 mm focal length	25 mm focal length
20 μm fibre	6.5 μm (1549)	8.1 μm (2084)	8.1 μm (1893)
50 μm fibre	11.3 μm (5602)	12.5 μm (6520)	12.76 μm (5509)

Table 3.1 The axial resolution and signal to noise ratio for different optical designs

Table 3.1 summarise the values obtained for the axial resolution and Raman signal for several combinations of focusing lenses and fibre optics. Figure 3.22 shows that the axial resolution can be as low as 6.35 μm when the diameter of the optical fibre is reduced to 9 μm and 25 mm focal length focusing lens. However, in this case the SNR is decreased to 600. A similar value for the axial resolution can be obtained with a 20 μm diameter optical fibre and Zeiss 5× microscope objective but with two fold increases in the signal noise ratio. For the optical fibre with 50 μm diameter the best results for axial resolution was achieved when the Zeiss 5× microscope objective was used. In conclusion the diameter of the optical fibre influences the signal collection efficiency and axial resolution as well. The best performance was obtained when Zeiss 5× was and related to its correction of the optical aberrations compared to the achromatic lenses. The final choice of optical fibre depends on the experiment requirements.

3.7 Sample retro-positioning

For sample retro positioning on the Raman micro-spectrometer an algorithm was developed to allow the identification of the measured area after the sample was removed from the microscope. The cell chambers were made of titanium and marks were engraved using laser close to the MgF_2 disk (figure 3.23). In the first step the coordinates of two marks on the sample holder were recorded (x_0, y_0, x_1, y_1). Then coordinates of each when Raman spectra were collected were recorded (x_s, y_s). On the sample holder was place back on the microscope stage the new coordinates of the reference marks were recorded ($x_{0'}$, $y_{0'}$, $x_{1'}$, $y_{1'}$), then the coordinates $x_{s'}$, $y_{s'}$ can be calculated using:

$$x_s' = x_s \cos\alpha_s - y_s \sin\alpha_s \tag{3.11}$$

$$y_s' = x_s \cos\alpha_s - y_s \sin\alpha_s \tag{3.12}$$

where

$$\alpha_s = \tan^{-1}\frac{y_1' - y_0'}{x_1' - x_0'} - \tan^{-1}\frac{y_1 - y_0}{x_1 - x_0} \tag{3.13}$$

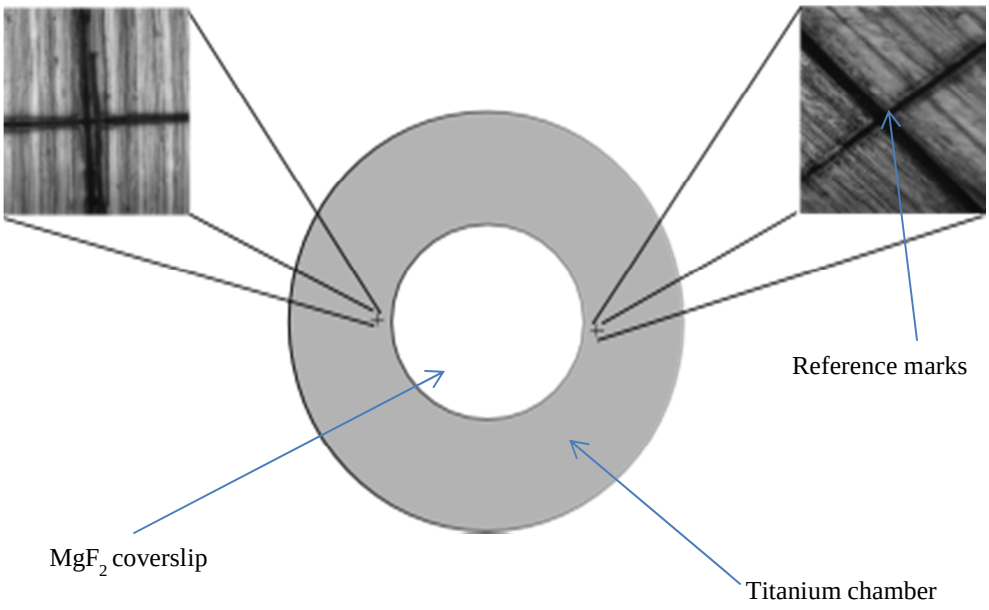

Figure 3.23 Titanium cell chamber with laser marks.

Using polystyrene micro-beads, the accuracy of the retro positioning was measured to be 2-4 μm, which is well below the size of the cell investigates in this thesis (10-60 μm diameter).

3.8 Raman spectral imaging of human endothelial cells

The Raman micro-spectrometer using 710 nm laser excitation was tested for spatial imaging of human endothelial cells. The system was used to acquire images and map the distribution of nucleic acids and lipids inside cells.

3.8.1 Cell culture

Human endothelial cells (HBMEC) were provided by Dr Hany El Sheika from the School of Veterinary Medicine and Science, The University of Nottingham. The cells were purchased frozen from HPA tissue culture collection, (UK). Directly after thawing, HBMEC were cultured in RPMI medium supplemented with 20% heat-inactivated foetal calf serum (Invitrogen, UK). Cultured cells were grown at 37 °C with 5% CO_2. Cells were then split weekly in 1:3 ratios using trypsin-EDTA (Invitrogen, UK). Cells were counted on a hemocytometer and approximately 5000-10000 cells were seeded in a titanium cell-chamber. When approximately 30% of the cover slip surface was covered by cells, the cells were fixed. Culture medium was discarded and the coverslip was wash with 1X phosphate buffered saline (PBS), then, 1 ml of 2.5% glutaraldehyde was added to fix the cells. The coverslip is washed with 1X PBS three times to remove any traces of the fixative. Finally, the chamber is filled with PBS and kept at 4^0C until measurements.

3.8.2 Data analysis

Data preprocessing and analysis was done using home built functions in Matlab (Mathwork, USA). Data pre-processing involved removal of peaks caused by

detection of random cosmic rays, noise reduction by singular value decomposition (SVD), background subtraction and baseline correction. The spectral images were obtained by measuring the peak area of selected Raman bands after subtraction of local baseline. SVD is a mathematical method from algebra used to decompose a rectangular matrix M of size m×n into a product of three matrices [9]:

$$M = USV^T, \tag{3.11}$$

where U (m×m) is an orthogonal matrix of, V (n×n) is a transpose orthogonal matrix and S (m×n) is a diagonal matrix containing singular values. The diagonal matrix S contains elements with chemical significance and noise from original data. Hence a matrix can be reconstructed using only the components which contain relevant information for data analysis.

3.8.3 Results and discussions

Raman spectra of typical a human endothelial cell is shown in Figure 3.26 and contains bands from nucleic acids, proteins and lipids. Nucleic acids are present with bands at 788 cm^{-1} (O-P-O phosphodiester bond in DNA), 828 (tyrosine) and 1095-1060 cm^{-1} (PO_2^- streching). Raman bands associated to proteins can be distinguish at 760 cm^{-1} (tryptophan), 854 cm^{-1} (tyrosine), 1003 cm^{-1} (phenylalanine), 1220-1284 cm^{-1} (amide III), 1420-1480 cm^{-1} (C-H bending), 1655-1680 cm^{-1} (amide I). Lipids band at 717 cm^{-1} belongs to C-C-N^+ stretching

vibration of phosphadylcholine group. Other Raman bands of lipids are present at 1301 cm^{-1} (C-H vibration) and 1660 cm^{-1} (C=C streching) [10].

Figures 3.25 (A, B, C) shows the bright field image of a typical HBMEC cell and that corresponding to Raman spectral images of the lipids (717 cm^{-1}) and DNA (788 cm^{-1}). These Raman images were obtained by scanning a square area of 60x38 µm with a step size of 1 µm and integration time of 500 ms per pixel.

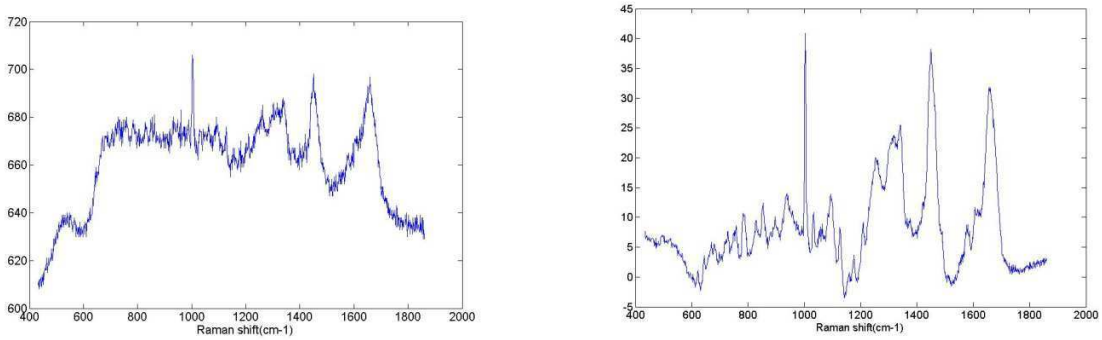

Figure 3.24 Typical examples of Raman as measured (a) and after pre-processing (b). The Raman were measured from the nucleus (acquisition time 500ms)

Both Raman images at 717 cm^{-1} and 788 cm^{-1} are showing a considerable distinction in their spatial distribution. By comparing the Raman image at 788 cm^{-1}, with the bright field image of the endothelial cell, we can conclude that the Raman image at 788 cm^{-1} overlaps with the nuclear region of the cell. Further comparison between individual Raman spectra taken from the cell nucleus and cytoplasm are presented in Figure 3.25 E.

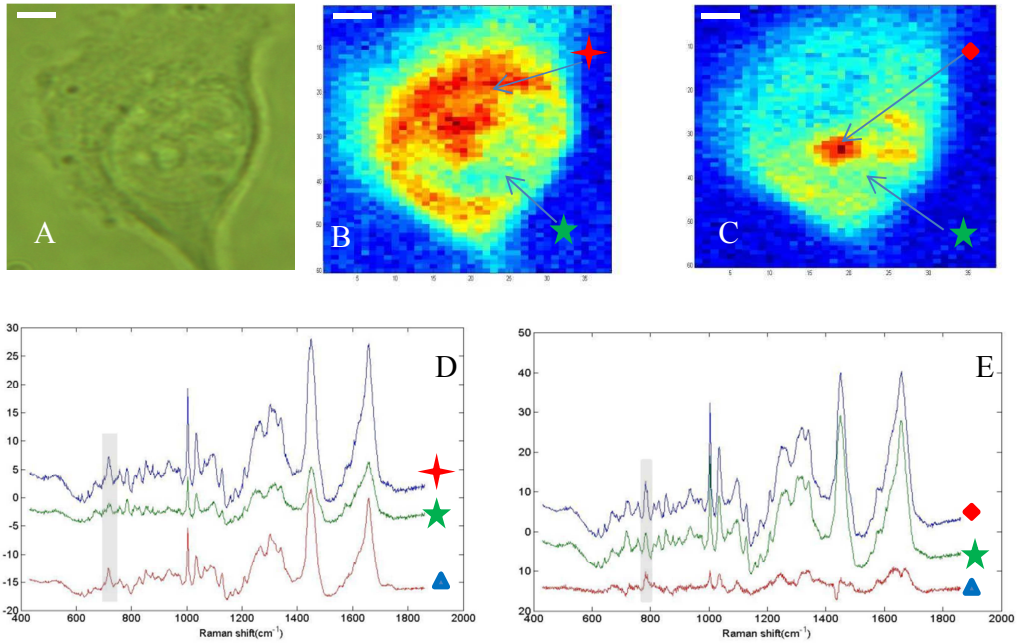

Figure 3.25 a Bright field image of the cell A) Raman images corresponding to the 717 cm^{-1} band (red region) B) and 788 cm^{-1} band (red region) C) Individual Raman spectra from selected position of the red region at 717 cm^{-1} (red star), outside red region (green stars) and computed difference (blue triangle) D) Individual Raman spectra from selected position of the red region at 788 cm^{-1} (red diamond) outside red region (green stars) and computed difference (blue triangle E) (acquisition time 500 ms/pixel). (scale bars: 5 µm).

The difference spectra bring forward positive bands at 788 cm^{-1} and 1578 cm^{-1} (guanine and adenine) which indicates a significant presence of nucleic acids. Individual spectra from Raman image at 717 cm^{-1} are compared along with their computed difference in figure 3.25 D. The intense band 717 cm^{-1} highlighted in the computed difference suggest a significant presence of phospholipids. This is not surprising since endothelial cells are involved in lipids metabolism. It has been

reported that endothelial cells incorporate the fatty acids from cells and convert them into phospholipids and triglycerides [11]. Also different cell organelles like endoplasmic reticulum, the Golgi apparatus or intracellular vesicles are covered by a membrane which comprise of phospholipids.

3.8.4 Conclusions

In this chapter were presented the design and characterization of an Raman micro-spectrometer optimized for Raman spectral images of cells. The selection of 710 nm wavelength laser improved the signal to noise ratio by a factor of 1.54 compared to previous instruments using 785 nm laser.

Measurements of human endothelial cells demonstrated the ability of this instrument to map different biochemical constituents inside single cells with acquisition as short as 500 ms/pixel. This is a 4 fold improvement compared to previous equipment available in our laboratory [6] and more than 10 times faster improvement compared commercial instruments (InVia Raman microscope from Renishaw) [12]. The acquisition time is comparable to other Raman micro-spectrometer using lasers in the visible region where the Raman scattering efficiency is considerable higher. However, visible lasers are less suitable for studying live cells as they can induce cell damage at considerable lower powers [13]. The spatial distribution of lipids and nucleic acids was determined by

mapping the intensity of the 717 cm^{-1} and 788 cm^{-1} bands and images with spatial resolution of 1 µm were obtained.

References:

1. Liang, H., et al., *Wavelength dependence of cell cloning efficiency after optical trapping.* Biophysical Journal, 1996. **70**(3): p. 1529-33.
2. Neuman, K.C., et al., *Characterization of photodamage to Escherichia coli in optical traps.* Biophysical Journal, 1999. **77**(5): p. 2856-63.
3. http://microscope.olympus-global.com/uis2/en/uplsapo60xw/, *UPLSAPO 60XW.*
4. Technology, C., *Long Pass filter*. 2010.
5. Semrock. *45^0 dichroic mirror*. Available from: http://www.semrock.com/Catalog/Detail.aspx?FilterPartID=767&CategoryID=11.
6. Zoladek, A., et al., *Non-invasive time-course imaging of apoptotic cells by confocal Raman micro-spectroscopy.* Journal of Raman Spectroscopy, 2011. **42**(3): p. 251-258.
7. Pully, V.V., et al., *Microbioreactors for Raman microscopy of stromal cell differentiation.* Anal Chem, 2010. **82**(5): p. 1844-50.
8. Andor, i.S.
9. Golub, G.H. and C. Reinsch, *Singular Value Decomposition and Least Squares Solutions.* Numerische Mathematik, 1970. **14**(5): p. 403-&.
10. Tu, A.T., *Raman spectroscopy in biology: principles and applications*. 1982: Wiley.
11. Denning, G.M., et al., *Role of triglycerides in endothelial cell arachidonic acid metabolism.* J Lipid Res, 1983. **24**(8): p. 993-1001.
12. Gentleman, E., et al., *Comparative materials differences revealed in engineered bone as a function of cell-specific differentiation.* Nature Materials, 2009. **8**(9): p. 763-770.
13. Puppels, G.J., et al., *Laser irradiation and Raman spectroscopy of single living cells and chromosomes: sample degradation occurs with 514.5 nm but not with 660 nm laser light.* Exp Cell Res, 1991. **195**(2): p. 361-7.

Chapter 4: Cytoplasmic RNA in Undifferentiated Neural Stem Cells: A Potential Label-Free Raman Spectral Marker for Assessing the Undifferentiated Status

In this chapter Raman micro-spectroscopy (RMS) was used to identify, image and quantify potential molecular markers for label-free monitoring the differentiation status of individual live neural stem cells (NSCs) in vitro. The differences between Raman spectra of NSCs and glial cells indicated that the discrimination of the NSCs was based on higher concentration of nucleic acids in NSCs. Spectral images corresponding to Raman bands assigned to nucleic acids for individual NSCs and glial cells were compared with fluorescence staining of cell nuclei and cytoplasm to show that the origin of the spectral differences were related to cytoplasmic RNA.

4.1 Introduction

Neural stem cell-based therapies are emerging approaches opening radically new strategies for the treatment of neurological diseases [7]. Currently, neurological diseases are one of the leading causes of adult disability and it is estimated that by 2040 neurological diseases will surpass cancer as the second most common cause of death among elderly people [8]. In light of our ageing population, the development of effective therapeutic strategies for neurological disorders is of great importance. Although the potential clinical impact of stem cell therapy for neurological diseases has already been shown [9], there are still a number of challenges to overcome before it can be considered suitable for widespread, long-term use. One such challenge is the identification of appropriate cell sources and the maintenance of a stable cell phenotype during the necessary phase of in vitro expansion. Current approaches for the characterization of neural stem cells (NSCs) in vitro are experimentally intensive, often employ destructive assays [10] rendering time-course experiments impossible, or are based on crude estimates, such as morphological features [11], which are insufficient to provide mechanistic insight into cellular processes. In order to address fundamental questions necessary for process discovery and development of robust cell cultures for cellular therapy, new methodologies capable of quantifying key biomarkers in a non-invasive manner are urgently needed [12].

Conventional cell biology assays (eg. polymerase chain reaction, western blotting, etc) are invasive and are not suitable for characterizing heterogeneous cell

populations since they require a large number of cells and results represent averages over entire cell populations. Fluorescence imaging can provide high-spatial resolution information for cells in vivo and in vitro, but often relies on lineage-specific surface markers that are expressed on the cell membrane [13]. However, there are numerous cases, including NSCs, where the major lineage specific markers are intracellular targets and detection requires fixation and permeabilization of cell membrane, rendering the cell unusable in a clinical environment.

Recently, Raman micro-spectroscopy (RMS) has been proposed for label-free non-invasive characterisation of stem cells and their progeny [[14-20]. RMS combines the chemical specificity of Raman spectroscopy with the high spatial resolution of optical microscopy to provide detailed molecular information on cells without using labels or other invasive procedures [21]. Since water has a low Raman scattering cross-section compared to most biomolecules, Raman spectra of cells have only a minimal background signal from water. Therefore, repeated measurements by Raman spectroscopy on viable cells maintained under physiological conditions are usually easier to carry out [22] compared to infrared absorption spectroscopy, where the strong absorption bands of water can distort the IR spectra[23, 24].

The basic hypothesis for using RMS to discriminate between undifferentiated and differentiated cells relies on the expression of specific biomolecules by the cells at various stages of differentiation. Earlier studies reported that undifferentiated murine embryonic stem cells (mESCs) had higher

concentration of mRNA compared to mESCs after 14 and 21 days of differentiation induced by removal of leukaemia inhibitory factor[14]. These biochemical differences were related with the increased translation of dormant mRNAs during differentiation of the mESCs, by similarity with maturation of oocytes. Spectral differences related to nucleic acids were also reported for human ESCs (hESCs), but spectral differences were mostly associated to the smaller cytoplasm to nucleus ratio of undifferentiated cells compared to differentiated cells[17]. Comparison between different age groups of rhesus monkey mesenchymal cells derived from bone marrow also indicated a higher DNA and lower protein contribution in the Raman spectra of fetal compared to juvenile cells [25]. Spectral variations assigned to glycogen have also been reported for hESCs maintained under normal growth conditions in vitro [18, 26].

In addition to undifferentiated stem cells, RMS has also been used for non-invasive phenotypic identification of individual cells or characterization of differentiated cell cultures derived from stem cells. Comparison between Raman spectra of human bone marrow stromal cells grown in purposed-built bioreactors over 21 days in basic and osteogenic culture media showed biochemical differences related to cell differentiation and mineralisation [6]. Differences between the bone nodules formed by osteoblasts derived from mESCs and native tissues were also identified by Raman spectroscopy [27]. More recently, RMS has also been proposed for phenotypic identification of individual cardiomyocytes within highly heterogeneous cell populations as commonly obtained during in vitro differentiation of hESCs. High accuracy discrimination models based on Raman

bands associated mainly to glycogen and myofibrils allowed identification of hESC-derived cardiomyocytes with sensitivity >96% and specificity >97% [19].

Although currently the measurement speed is limited to only few cells per second, these initial studies are starting to progress the Raman spectroscopy technique towards the development of Raman-activated cell sorting for label-free enrichment and purification of cell populations with well-defined phenotype[28].

In this study we have investigated the ability of RMS to provide label-free spectral markers for non-invasive monitoring of the differentiation status of live NSCs in vitro, as well as detect spectral changes during their differentiation towards the glial phenotype. First, multivariate statistical models were developed to discriminate between undifferentiated NSCs and glial cells, and then high spatial resolution Raman spectral imaging was used to correlate the observed spectral differences with molecular properties of NSCs.

4.2 Materials and Methods

4.2.1 Cell Culture

Cell culture reagents were purchased from Invitrogen (Paisley, UK) unless otherwise stated. Mouse neural stem cells were cultured as described elsewhere [10]. Briefly, cells were maintained in NSC medium prepared with DMEM/F12 and Neurobasal medium (1:1), N2, B27, Pen/Strep, bFGF (20 ng/ml) and EGF (20

ng/ml, Sigma, UK). To passage the cultures, the cells were treated with 1 ml of Accutase (Patricell Ltd, Nottingham, UK) and the sample was incubated at 37ºC for 5 minutes. After a PBS wash, the pellet was resuspended in fresh medium and transferred to a new vessel. Culture stocks were routinely split 1 in 3.

For Raman analysis, cells were seeded on glass Matrigel (Becton Dickinson) according to the manufacturer's instruction, to promote cell adhesion. For in vitro differentiation, NSC medium was replaced with medium containing DMEM/F12 and Neurobasal (1:1), 1% FCS, Pen/Strep. Fresh medium was added every 2 days, taking care not to disturb the monolayer. After treatment, cells were fixed with 4% ice-cold paraformaldehyde and stored at 4ºC until analysis.

4.2.2 Immunostaining

Samples were washed in PBT (PBS + 0.1% Tween-20 (Sigma)), blocked for 1 hour in 1% blocking solution (PBT+0.1% FCS), and incubated overnight at 4ºC with an anti-GFAP antibody (Dako, Ely, UK) diluted 1/100 in 1% blocking solution. After extensive washing in PBT for 40 minutes, samples were incubated with a fluorescein-conjugated secondary antibody (Vector Labs, Peterborough, UK) for 1 hour, washed for 1 hour in PBS, and kept in PBS containing 1 µg/ml Hoechst 33342 (Sigma) until imaging.

4.2.3 Raman micro-spectroscopy measurements

For measurements on live cells, a Raman micro-spectrometer equipped with an environmental enclosure (Solent, Segensworth, UK) was used to maintain the cells under sterile physiological conditions (culture medium, 37°C temperature, 5% CO2). The instrument was based on an inverted microscope (IX 71, Olympus, Essex, UK) with a 60×/NA 0.90 water-immersion objective (Olympus), a 785 nm ~170 mW diode laser (after objective) (Toptica Photonics, Munich, Germany), a spectrometer equipped with a 830 lines/mm grating and cooled deep-depletion back-illuminated CCD detector (Andor Technologies, Belfast, UK) and an automated step-motor stage (Prior, Cambridge, UK). For the high spatial resolution spectral images, a second confocal Raman micro-spectrometer was used which is described in Chapter 3 of this thesis. Both instruments were calibrated prior to each experiment using a standard tylenol sample and the spectral resolution was ~2-3 cm^{-1} in the 600-1800 cm^{-1} region. Purpose designed titanium cell-chambers were built, which incorporated MgF_2 coverslips (0.17 mm thick) at the bottom to enable acquisition of Raman spectra of the cells using the inverted optical configuration. For the live cells, the Raman spectrum of each individual cell represented the average of a total of 625 spectra measured at different positions inside the cell by raster-scanning the cell through the laser focus in 2 µm steps (equivalent to a grid of 25 by 25 points). The acquisition time at each position was 1 second. After the acquisition of Raman spectra was completed, the position coordinates of each cell was recorded, the cells were fixed and prepared for immunostaining (phenotypic marker and cell nucleus). The

phenotypic marker of the cells was established using a wide-field fluorescence staining system integrated on the Raman microscope. The retro-positioning of each cell was achieved by using the cell coordinates (accuracy ~5 µm).

4.2.4 Data analysis and processing

Data preprocessing consisted of removal of spectra containing cosmic rays, background subtraction and normalization. The average of the Raman spectra measured at points outside of the cell (automatically identified using a k-means clustering analysis) represented the background spectrum (contributions from the culture medium, MgF_2 coverslip and microscope objective). The Raman spectrum representative of each cell was obtained by algebraic subtraction of the background spectrum from the average of the Raman spectra at all positions inside the cell. All Raman spectra were then normalised using the standard normal variance method [19, 29].

The Raman spectra of cells were analysed by principal component analysis (PCA) and linear discriminant analysis (LDA). Raman spectra measured of purified commercial nucleic acids were measured from baker's yeast RNA, calf thymus DNA and human serum albumin (all from Sigma Aldrich, UK). Spectral images corresponding to selected Raman bands were obtained by calculating the area under the spectral bands after subtraction of an estimated local linear baselines and representing the integrated intensity value at each measurement position in the cell.

Prior to calculation of band areas, the singular value decomposition method was used to reduce the noise in the Raman spectra [30]. The trapz function in Matlab was used to calculate the area under each curve. The resulting volume of the cell was the sum over entire values obtained with trapz function.

4.4 Results and Discussions

4.4.1 Discrimination between undifferentiated neuroprogenitors and glial cells

The first aim of the study was to identify Raman spectral bands which enable discrimination between undifferentiated NSCs and NSC-derived glial cells by using non-invasive Raman spectral measurements on live cells. Although previous studies using 785 nm lasers to measure Raman spectra of other cell types showed that no damage was induced to the cells [19, 31] viability tests on selected NSCs and NSC-derived glial cells were carried out after completion of the Raman measurements. The results of the fluorescence staining tests on 4 undifferentiated stem cells and three glia cell confirmed that the cells remained viable at the end of the Raman measurements (figure 4.1).

Figure 4.2 presents average Raman spectra and immuno-fluorescence images and of two typical live glial cells and two groups of NSCs. When carrying out Raman spectral measurements on individual live NSCs it was found that cell

motility was significant over the measurement time (~10 minutes). Therefore, to reduce errors due to cell motility, the Raman spectra of NSCs were recorded as full raster scans over individual cells or groups of 5-6 cells in proximity, for which motility was observed to be considerably reduced. No differences were observed in the Raman spectra of individual NSCs or NSCs in groups (figure 4.2).

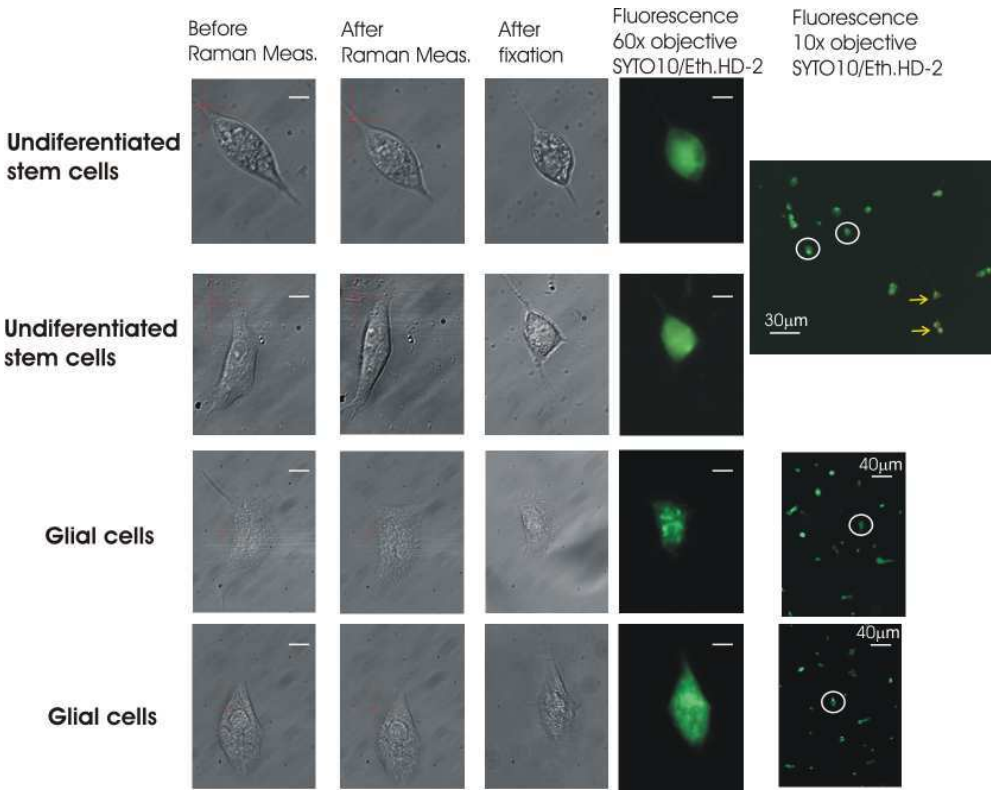

Figure 4.1: Viability tests for typical NSCs and NSC-derived glial cells following laser exposure during the acquisition of Raman spectra (Scale bar 10 µm unless otherwise specified). The morphology of the cells irradiated by the laser remained typical to the phenotype of the cells. In the lower magnification images, the cells exposed to the laser were marked by a white circle. The cells investigated by RMS stained positive for the SYTO10 dye (green) and negative for the ethidium homodimer-2 dye (red) demonstrating that the laser exposure did not affect their viability. The

staining of the cells was similar to the surrounding healthy cells which were not exposed to the laser. The yellow arrows indicate few cells not exposed to the laser but which had compromised cell membrane (stained positive for the ethidium homodimer-2 dye).

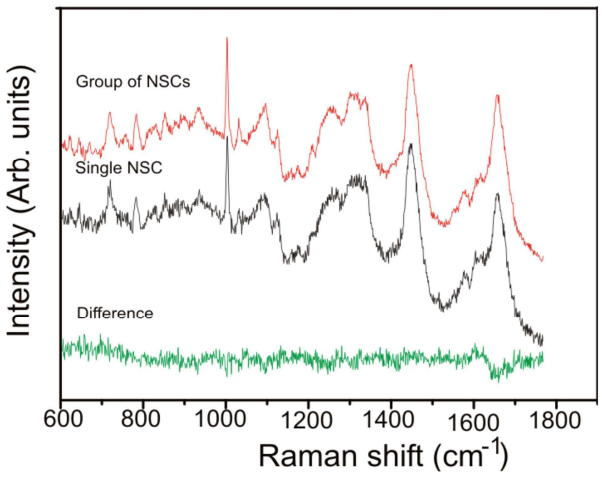

Figure 4.2. Comparison between the Raman spectra of a typical individual NSC and a group of NSCs.

After Raman measurements, all cells were fixed and stained to confirm the phenotype: nestin was used for undifferentiated NSCs and GFAP was used for glial cells. The phenotypic confirmation was carried out to ensure that no errors due to potential population heterogeneities were included in the Raman spectral model; as such errors can significantly reduce the phenotypic discrimination of the cells. The Raman spectra in Figure 4.2A show that the sampling method used in this study led to high signal-to-noise Raman spectra which accounted for the molecular heterogeneity of the cells. Therefore, such average Raman spectra are representative of an entire cell or group of cells analysed. The Raman spectra of both cell types consist of typical Raman bands of cellular biomolecules (nucleic

acids, protein, lipids and carbohydrates) and are consistent with previous reports on other cell types [21]. Spectral differences between the glial and NSC populations can be observed in particular in the 700-830 cm^{-1} region, which contains contributions mainly from nucleic acids. However, to confirm these spectral differences, Figure 4.4A presents the average Raman spectra of 120 NSCs (19 groups) and 27 differentiated glial cells along with the computed difference spectrum (average spectrum for all NSCs minus average spectrum of all glial cells). Several Raman bands corresponding to nucleic acids can be identified in the difference spectrum, which are significantly larger than the computed standard deviation at the corresponding wavenumbers.

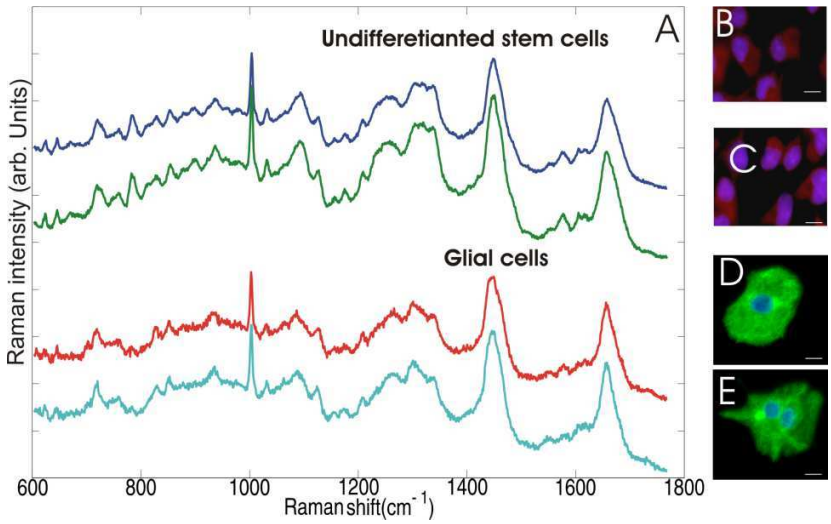

Figure 4.3. (A) Typical Raman spectra measured for undifferentiated neural stem cells and glial cells, and the corresponding fluorescence staining of the cells confirming their phenotypes:

(B,C) undifferentiated neural stem cells: blue=nuclei, red=nestin; (D,E) glial cells: blue=nuclei, green=GFAP (Glial fibrillary acidic protein).

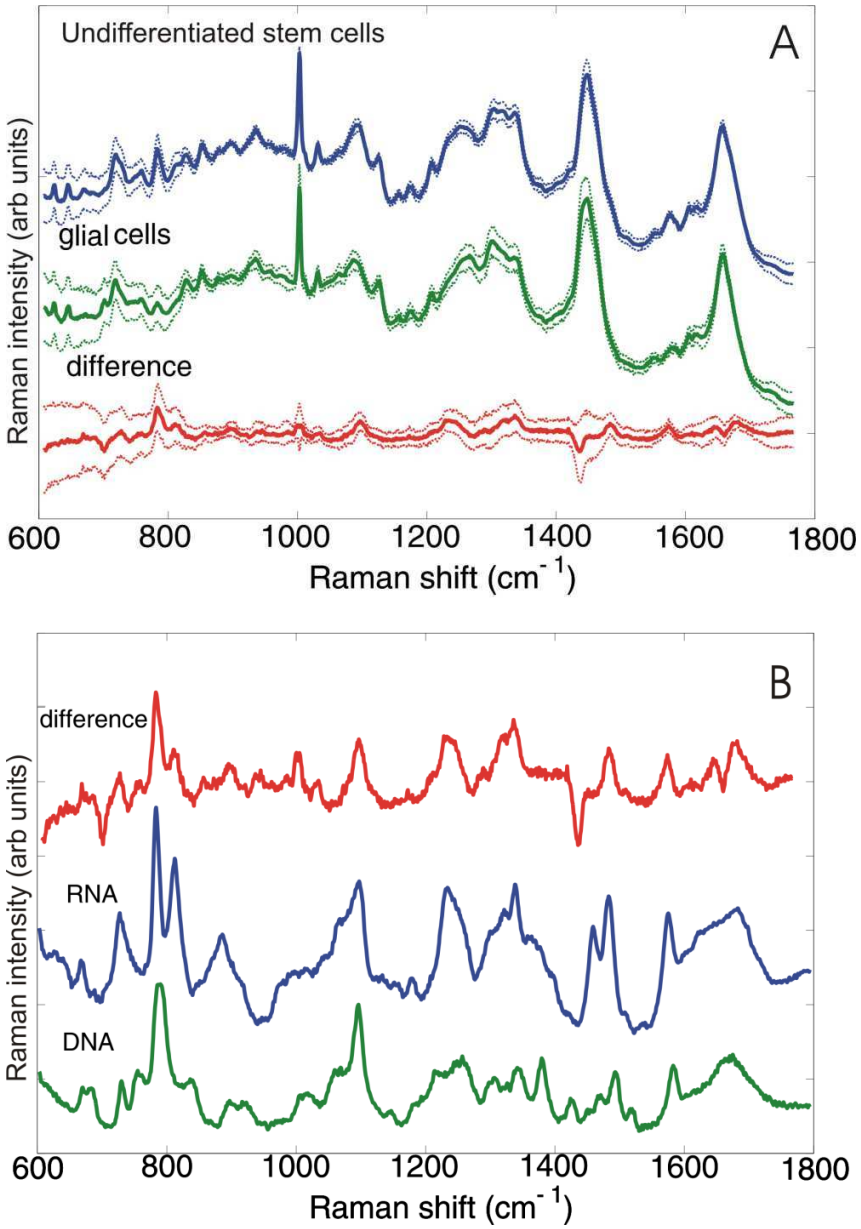

Figure 4.4: (A) Average Raman spectra of undifferentiated stem cells and glial cells, and their computed difference. The side lines represent the standard deviation calculated at each

wavenumber. (B) Comparison between the computed difference spectrum in (A) and the Raman spectra measured from purified RNA and DNA.

A comparison between the difference spectrum and the Raman spectra of DNA and RNA in water are presented in Figure 4.4B. Based on previous reports using X-diffraction measurements on nucleic acids solution at neutral pH and equilibrium conditions (as used in our experiments), the DNA adopts a B-conformation while the RNA adopts a A-conformation [32, 33] . Raman bands associated to the DNA and RNA bases can be identified at 729 (adenine), 782 and 785 (uracil, cytosine), and 1578 cm^{-1} (guanine and adenine) [34].

Raman bands corresponding to the nucleic acid backbone can also be identified and used for identification of the conformation of the nucleic acids. B-conformation DNA elicits a strong band at 788 cm^{-1} and a shoulder at 835 cm^{-1} corresponding to the symmetric and asymmetric O-P-O phosphodiester stretching vibrations. For A-DNA and RNA, the symmetric vibration shifts to 813 cm^{-1} and the band corresponding to the asymmetric stretching vanishes [35, 36]. In addition, a Raman band at 1098 cm^{-1} can also be identified corresponding to the PO_2^- vibrations. These results suggest that the main spectral differences between NSCs and differentiated glial cells rely on a higher concentration of nucleic acids in NSCs [14].

A multivariate spectral model based on the principal component analysis (PCA) followed by linear discriminant analysis (LDA) was developed to enable spectral discrimination between the two cell types. The loading spectra corresponding to the first three principal components capturing 82.1% of spectral variation are showed

in Figure 4.4A. For the LDA model, only PC1, PC2 and PC3 were used as other PCs either consisted only of broad bands characteristic to the culture medium or were dominated by noise, therefore they did not improve the discrimination between the two cell types.

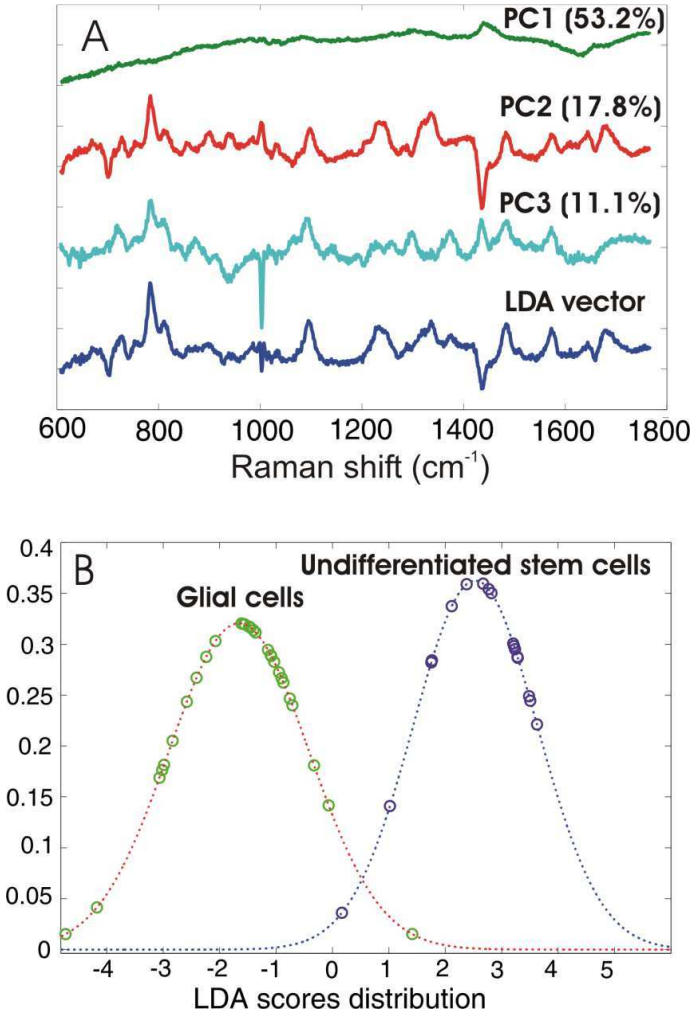

Figure 4.5: (A) The loadings of the first three PCA components (PC1, PC2, PC3) used for building the LDA discrimination vector to maximise the discrimination between the Raman spectra of the undifferentiated NSCs and glial cells. The variance captured by each principal component is

shown in the brackets. (B) Distribution of LDA scores for undifferentiated stem cells (purple dots) and glial cells (green dots).

The computed linear discriminant analysis loading which maximized the discrimination between the NSCs and glial cells is presented in Figure 4.4A and the corresponding scores in Figure 4.4B. The probability distribution for the LDA scores (Figure 4.4B) shows a clear distinction between NSCs and glial cells. To determine the accuracy for phenotypic identification of NSCs, cross-validation (CV) was used to determine the sensitivity and specificity parameters for a certain target sensitivity or specificity. The leave-one-out CV showed that the LDA spectral model can discriminate between NSCs and glial cells with 89.4% sensitivity and 96.4% specificity.

4.4.2 Assignment and quantification of the Raman spectral markers

The computed difference spectrum in Figure 4.3 indicates that significant molecular changes related to nucleic acids can be identified between undifferentiated NSCs and glial cells. In particular, one can highlight the Raman band at 813 cm^{-1} which has been assigned to the symmetric stretching of the phosphodiester bonds in nucleic acids. However, this spectral difference could be related either to conformational changes of DNA from B-form to A-form or due to changes related to the RNA concentration.

A decrease in the 813 cm^{-1} band was also detected by RMS in the case of spontaneous differentiation of mESCs over a 21 days period [14]. The intense 813

cm^{-1} band in undifferentiated mESCs was suggested to be related to repressed translation of mRNAs in the embryonic stem cells followed by increased mRNA translation during the differentiation. Spectral differences associated to nucleic acids were also found in undifferentiated and differentiated hESC and mesenchymal stem cells [17, 25], and were attributed to a higher nucleus to cytoplasm ratio in the undifferentiated cells and associated to the increased proliferation rates compared to differentiated cells. However, these studies recorded only single point measurements for individual cells and did not include spatially resolved Raman spectra needed to determine whether the increased signals corresponding to nucleic acids was associated to the cell nuclei (mainly DNA) or cytoplasm (RNA), or alternative methods to distinguish between RNA and A-form DNA.

One of the important features of confocal RMS is that it allows the mapping of the biomolecules within individual cells with diffraction limited spatial resolution. Comparison between Raman spectral images corresponding to specific biomolecules and fluorescence staining also allows a better correlation between Raman spectral information and cellular components [19, 29]. In this case, such comparison was carried out to establish whether the spectral differences were related to DNA conformational changes (most DNA is located in the nucleus) or to RNA concentration (cytoplasmic RNA). Raman spectral maps for the 788 cm^{-1} and 813 cm^{-1} were measured and compared with fluorescence staining for the nucleus and cytoplasm for the same cells. Such comparisons were carried out on both NSCs and glial cells to establish whether the spectral changes corresponded to the nuclei or cytoplasm. However, Raman imaging requires raster scanning the cell through

the laser focus and collection of a full spectrum at each position. Although individual Raman spectra with sufficient signal-to-noise ratio in the 700-850 cm^{-1} region can be acquired using integration times as short as 500 ms/pixel (Figure 4.5), a Raman mapping using step sizes of half the diffraction limit (500 nm) requires 20 minutes. To avoid cell movement during the Raman imaging and thus enable accurate comparison between the Raman maps and fluorescence images, the measurements were carried out on fixed NSCs and glial cells. The comparison between the Raman spectra of fixed and live cells shows that paraformaldehyde fixation of cells did not significantly affect the Raman spectra (Figure 4.7), findings which agree with published reports on other cell types [37, 38].

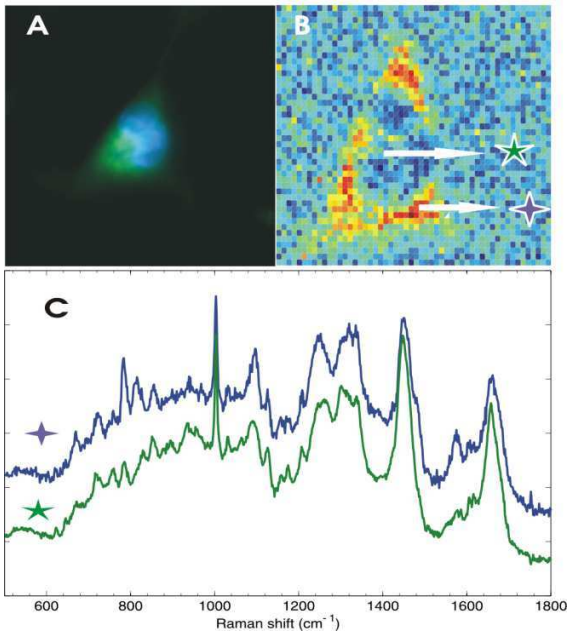

Figure 4.6: Fluorescence image of the progenitor stem cell (A); Image (area of 813 cm^{-1} peak) of the same undifferentiated stem cell at 500 ms (B); individual spectra taken from RNA and outside RNA region respectively(C)

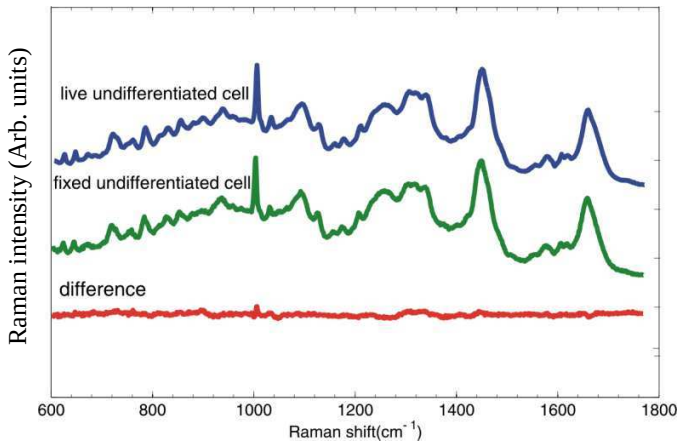

Figure 4.7: The comparison between the Raman spectra of fixed and live undifferentiated stem cells.

Figure 4.8 presents the spectral maps of two typical NSCs corresponding to the 788 cm^{-1} and 813 cm^{-1} Raman bands along with the corresponding phase contrast and fluorescence staining of the cell nuclei (DAPI) and cytoplasm (GFAP). Compared to the DAPI staining, the cell region of high 788 cm^{-1} intensity is larger than the cell nuclei because this band consists of an overlap between the C and U ring vibration at 785 cm^{-1} and the O-P-O symmetric stretch in B-DNA. Therefore, the Raman images corresponding to the 788 cm^{-1} highlight regions rich in both DNA and RNA.

However, comparison between the fluorescence images and the Raman images corresponding to the 813 cm^{-1} Raman band shows that the cell regions where these bands have high intensity correspond to the cytoplasm. To confirm the presence of the 813 cm^{-1} band in the cytoplasm of the NSCs, individual Raman spectra from locations of intense 788 cm^{-1} and 813 cm^{-1} Raman bands are also

presented in figure 4.8 and compared to spectra at other positions in the cytoplasm with reduced nucleic acid contributions (spectra dominated by other biomolecules such as proteins and lipids).

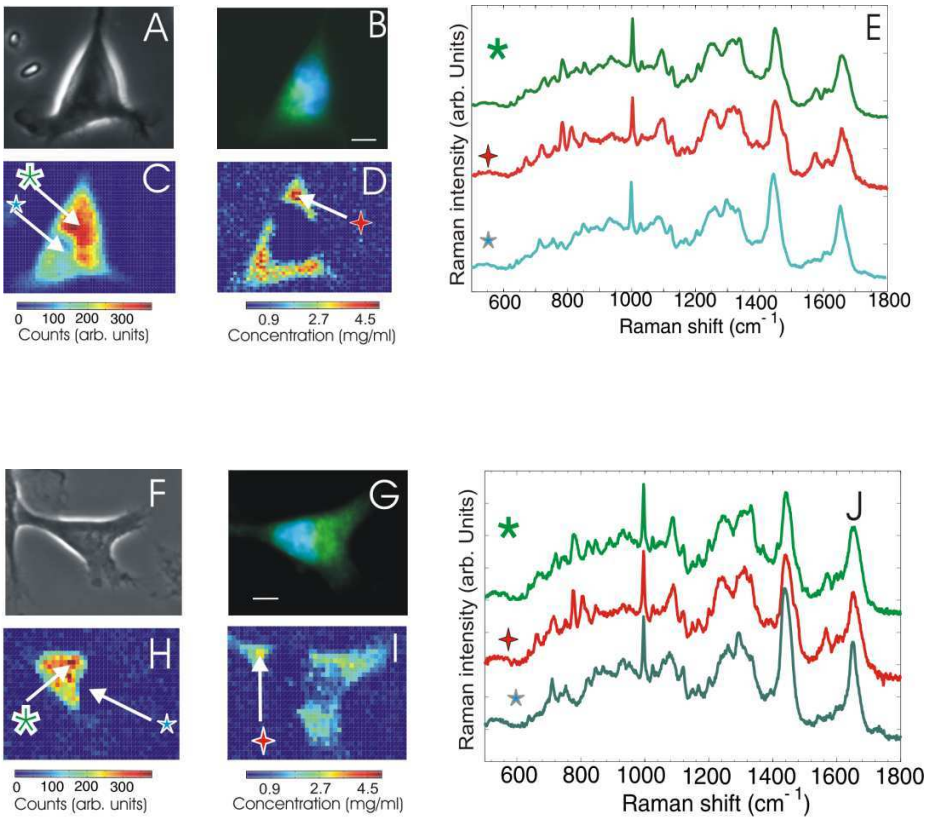

Figure 4.8: Phase contrast images (A,F), nuclei(blue)/nestin(green) fluorescence staining (B,G) and Raman spectral images corresponding to the 788 cm^{-1} band (C,H) and 813 cm^{-1} band (D,I) for two typical fixed undifferentiated neural stem cells. The Raman images in (D) and (I) were calibrated using the curve in Figure 6. (E), (J) Individual Raman spectra taken from selected positions of the nuclei (green star), cytoplasm regions rich in RNA (red star) and cytoplasm regions rich in phospholipids (blue star). (Scale bars: 10 µm).

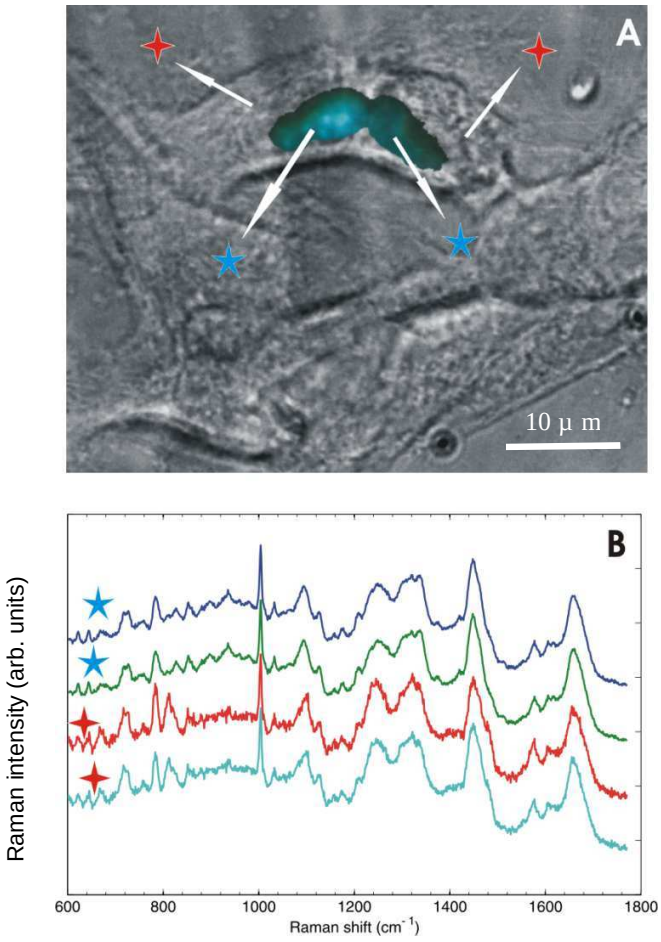

Fig 4.9: Confirmation of cytoplasmic RNA rich regions in live NSCs. Due to cell motility Raman maps were recorded at 2 µm step size (total imaging time ~6 minutes). (A) Overlap of DAPI image on the bright field image enables visualization of nucleic acids region; (B) individual Raman spectra from the nucleic and cytoplasmic regions rich in RNA.

Based on these results, it can be concluded that the assignment of the 813 cm^{-1} band corresponds to cytoplasm RNAs and not to conformational changes of the DNA. A confirmation of these findings for live NSCs is presented in the Figure 4.9. However, to reduce the errors due to cell motility when comparing Raman and

fluorescence images, the Raman spectral images were recorded at a lower spatial resolution (2 µm step size, total imaging time ~6 minutes).

Figure 4.10 presents, similar comparisons between Raman spectral maps of nucleic acids and fluorescence staining for two typical differentiated glial cells derived from NSCs

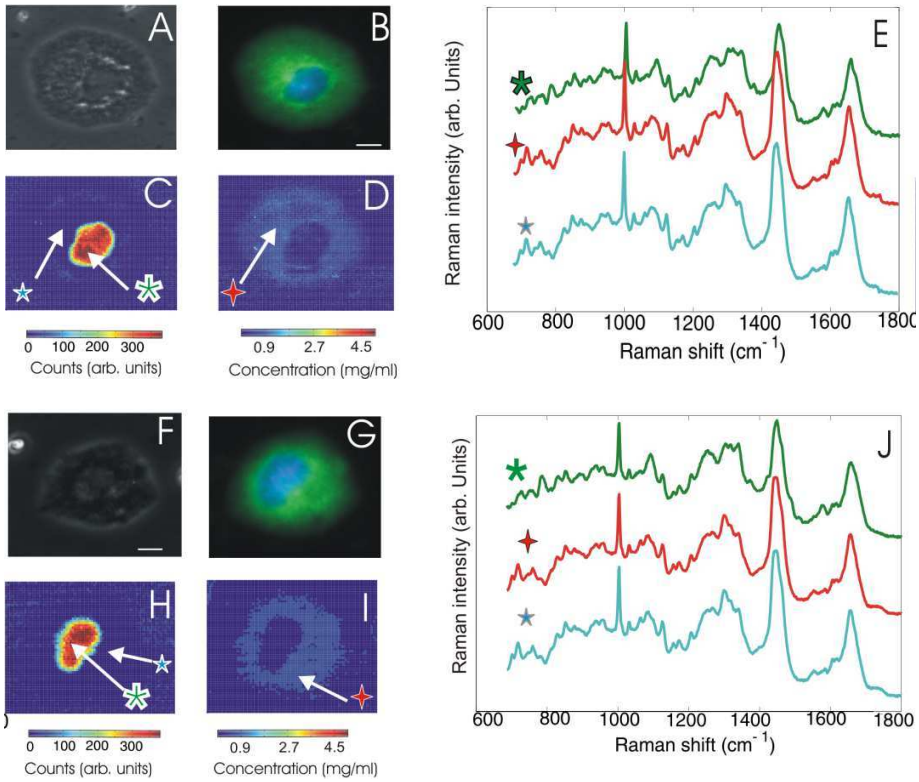

Figure 4.10: Phase contrast images (A,F), DAPI(blue)/FITC(green) fluorescence staining (B,G) and Raman spectral images corresponding to the 788 cm^{-1} band (C,H) and 813 cm^{-1} band (D,I) for two typical fixed glial cells. The Raman images in (D) and (I) were calibrated using the curve in Figure 6. (E), (J) Individual Raman spectra taken from selected positions of the nuclei (green star) and two positions in the cytoplasm (red and blue star). (Scale bars: 10 µm).

In this case, a very close similarity can be observed between the Raman maps corresponding to the 788 cm^{-1} band and the DAPI images of the nuclei.

These results indicate that, contrary to NSCs, contribution from nucleic acids in the glial cells can only be detected in the nucleus. Therefore, the concentration of the RNA in the cytoplasm of glial cells is considerably lower than in NSCs, becoming below the detection limit by RMS.

The origin of these spectral differences which allow the assessment of the differentiation status of NSCs by RMS may be attributed to two main properties of NSCs when compared to differentiated cells: lower cytoplasm volume and overall higher amount of RNA. Although an accurate evaluation of cytoplasmic volume is difficult, we attempted an estimation of the ratio between the cytoplasm volumes between NSCs and glial cells based on the fluorescence images and selected Raman maps. Assuming that the intensity of the 1450 cm^{-1} band corresponding to CH_2 vibrations in all biomolecules, can be used to measure the biomass volume, by summing the areas under all curves of the Raman maps for NSCs and glial cells (Figure 4.11C and 4.11 D). The calculated ratio of the cytoplasmic volume of the glial cells over the cytoplasmic volume of the NSCs is 4.84. Based on these estimates, the increase in cytoplasmic volume of the glial cells would lead to a maximum ~5 fold decrease in the concentration of cytoplasmic RNA if the overall amount of RNA would remain unchanged during the differentiation. Figure 4.11E presents a calibration curve for the 813 cm^{-1} Raman band corresponding to RNA as a function of concentration in phosphate buffer saline, built using similar measurement conditions as used for cell measurements.

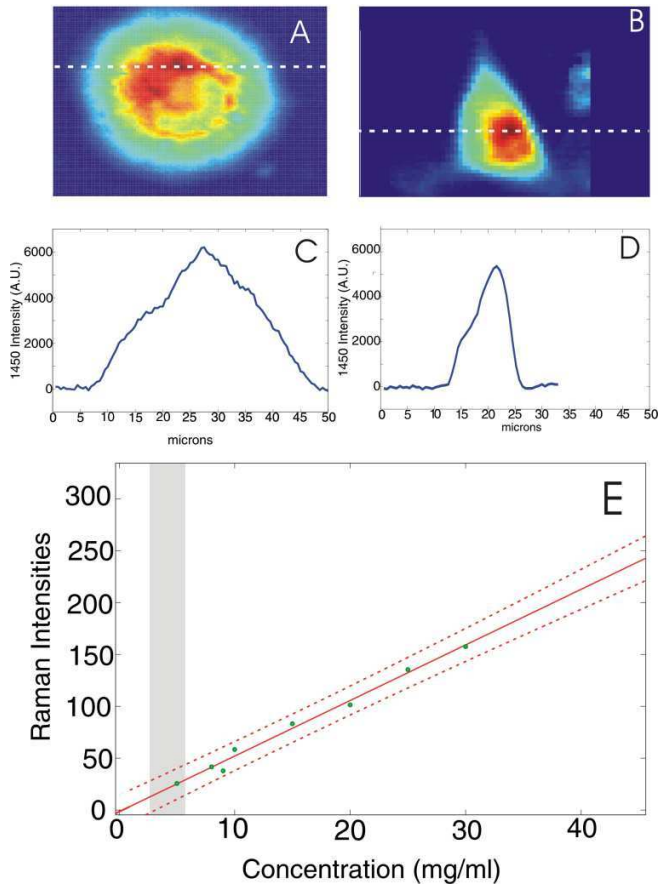

Figure 4.11: Raman spectra maps corresponding to the 1450 cm^{-1} band for a glial cell (A) and undifferentiated neural stem cell (B) and their corresponding profiles at the positions indicated by the white dotted lines (C, D). (E) Calibration curve for the 813 cm^{-1} Raman band using purified RNA solutions in phosphate buffer saline. The grey area highlights the range of maximum RNA concentrations in the cytoplasm of the undifferentiated neural stem cells.

According to this calibration curve, the maximum concentration of RNA in the cytoplasm of NSCs ranges from 3-5 mg/ml (accuracy in this range is

±1.2mg/ml) while for glial cells the concentration becomes lower than the detection limit of our instrument, which is ~2 mg/ml.

Therefore, these estimates indicate that the increase in the cytoplasm volume by a factor of 10 may account for a decrease in the cytoplasm RNA concentration during the differentiation of NSCs to the glial phenotype.

However, the higher intensities of Raman bands corresponding to RNA in NSCs may also be related to a higher amount of RNA in undifferentiated cells compared to fully differentiated cells. Early studies on lineage progenitors have reported a change in RNA content during the differentiation process. Histological analysis of embryonic brain explants has shown that neuroepithelial progenitor populations in the ependymal layer have a higher total RNA content than their mature differentiated progeny [39]. Increased concentration of nontranslated mRNAs corresponding to the post-transcriptional control of genes has been related to neurogenesis [40] and neuronal function [41], as well as stem cell proliferation and embryogenesis [42, 43].For example, high abundance of proteins which repress the translation of mRNAs and maintained the undifferentiated state of NSCs have been found in the cytoplasms of these cells [40]. In a different model, epidermal progenitors have similarly been reported to display higher RNA amounts than terminally differentiated keratinocytes [44]. Interestingly, the fine dynamics of these variations over the differentiation process appears to involve a transient increase before a significant drop in RNA amounts observed in mature differentiated lineages. More recently, the importance of RNA subtypes including long non-coding RNAs and microRNAs has been highlighted in the context of cell

differentiation [45-48]. Data gathered from mouse ES cells, and more recently NSCs, suggest that such non coding regulatory RNAs are dynamically regulated during the differentiation process. Further improvements in the imaging speed and discrimination potential of the Raman spectrum analysis may allow a finer characterisation of the distinct RNA components which are differentially regulated between NSCs and their progeny in live cultures.

4.5 Conclusion

RMS is an attractive technique for non-invasive characterisation of individual live cells in vitro. In this study, RMS was used to identify label-free spectral markers for non-invasive monitoring the differentiation status of live neural stem cells (NSCs) in vitro. Such techniques are urgently needed for the characterisation of cell populations and assessing their differentiation status non-invasively.

Principal component analysis (PCA) and linear discriminant analysis (LDA) models based on Raman spectra of undifferentiated NSCs and NSC-derived glial cells enabled discrimination of NSCs with 89.4% sensitivity and 96.4% specificity. The differences between Raman spectra of NSCs and glial cells indicated that the discrimination between these cell types is based on higher concentration of nucleic acids in NSCs compared to glial cells. Comparison between Raman mapping of DNA and RNA showed that the regions with largest spectral differences are located

in the cytoplasm of the NSCs and therefore can be assigned to cytoplasmic RNAs. These results are in agreement to previous studies on mouse embryonic stem cells which indicated a significant decrease in RNA during differentiation in vitro.

References:

1. Kalladka, D. and K.W. Muir, *Stem cell therapy in stroke: Designing clinical trials.* Neurochemistry International, 2011. **59**(3): p. 367-370.

2. Lilienfeld, D.E. and D.P. Perl, *Projected Neurodegenerative Disease Mortality among Minorities in the United-States, 1990-2040.* Neuroepidemiology, 1994. **13**(4): p. 179-186.

3. Rossi, F. and E. Cattaneo, *Opinion - Neural stem cell therapy for neurological diseases: dreams and reality.* Nature Reviews Neuroscience, 2002. **3**(5): p. 401-409.

4. Alcock, J. and V. Sottile, *Dynamic distribution and stem cell characteristics of Sox1-expressing cells in the cerebellar cortex.* Cell Research, 2009. **19**(12): p. 1324-1333.

5. Arocena, M., et al., *A Time-Lapse and Quantitative Modelling Analysis of Neural Stem Cell Motion in the Absence of Directional Cues and in Electric Fields.* Journal of Neuroscience Research, 2010. **88**(15): p. 3267-3274.

6. Fox, J.L., *FDA scrutinizes human stem cell therapies.* Nature Biotechnology, 2008. **26**(6): p. 598-599.

7. Fukuda, H., et al., *Fluorescence-activated cell sorting-based purification of embryonic stem cell-derived neural precursors averts tumor formation after transplantation.* Stem Cells, 2006. **24**(3): p. 763-771.

8. Notingher, I., et al., *In situ spectral monitoring of mRNA translation in embryonic stem cells during differentiation in vitro.* Anal Chem, 2004. **76**(11): p. 3185-3193.

9. Zuser, E., et al., *Confocal Raman microspectral imaging (CRMI) of murine stem cell colonies.* Analyst, 2010. **135**(12): p. 3030-3.

10. Chan, J.W., et al., *Label-Free Separation of Human Embryonic Stem Cells and Their Cardiac Derivatives Using Raman Spectroscopy.* Anal Chem, 2009. **81**(4): p. 1324-1331.

11. Schulze, H.G., et al., *Assessing Differentiation Status of Human Embryonic Stem Cells Noninvasively Using Raman Microspectroscopy.* Anal Chem, 2010. **82**(12): p. 5020-5027.

12. Konorov, S.O., et al., *Evidence of marked glycogen variations in the characteristic Raman signatures of human embryonic stem cells.* Journal of Raman Spectroscopy, 2011. **42**(5): p. 1135-1141.

13. Pascut, F.C., et al., *Noninvasive Detection and Imaging of Molecular Markers in Live Cardiomyocytes Derived from Human Embryonic Stem Cells.* Biophys J, 2011. **100**(1): p. 251-259.

14. Konorov, S.O., et al., *Raman microspectroscopic evidence that dry-fixing preserves the temporal pattern of non-specific differentiation in live human embryonic stem cells.* Journal of Raman Spectroscopy, 2011. **42**(4): p. 576-579.

15. Notingher, I. and L.L. Hench, *Raman microspectroscopy: a noninvasive tool for studies of individual living cells in vitro.* Expert Review of Medical Devices, 2006. **3**(2): p. 215-234.

16. Zoladek, A., et al., *Non-invasive time-course imaging of apoptotic cells by confocal Raman micro-spectroscopy.* Journal of Raman Spectroscopy, 2011. **42**(3): p. 251-258.

17. Kuimova, M.K., K.L.A. Chan, and S.G. Kazarian, *Chemical Imaging of Live Cancer Cells in the Natural Aqueous Environment.* Applied Spectroscopy, 2009. **63**(2): p. 164-171.

18. Marcsisin, E.J., et al., *Infrared microspectroscopy of live cells in aqueous media.* Analyst, 2010. **135**(12): p. 3227-3232.

19. Kim, B.S., et al., *Growth, differentiation, and biochemical signatures of rhesus monkey mesenchymal stem cells.* Stem Cells Dev, 2008. **17**(1): p. 185-98.

20. Konorov, S.O., et al., *Absolute Quantification of Intracellular Glycogen Content in Human Embryonic Stem Cells with Raman Microspectroscopy.* Anal Chem, 2011. **83**(16): p. 6254-6258.

21. Pully, V.V., et al., *Microbioreactors for Raman microscopy of stromal cell differentiation.* Anal Chem, 2010. **82**(5): p. 1844-50.

22. Gentleman, E., et al., *Comparative materials differences revealed in engineered bone as a function of cell-specific differentiation.* Nature Materials, 2009. **8**(9): p. 763-770.

23. Pascut, F.C., et al., *Toward label-free Raman-activated cell sorting of cardiomyocytes derived from human embryonic stem cells.* J Biomed Opt, 2011. **16**(4).

24. Matthaus, C., et al., *Label-free detection of mitochondrial distribution in cells by nonresonant Raman microspectroscopy.* Biophys J, 2007. **93**(2): p. 668-73.

25. Uzunbajakava, N., et al., *Nonresonant confocal Raman imaging of DNA and protein distribution in apoptotic cells.* Biophys J, 2003. **84**(6): p. 3968-3981.

26. Zoladek, A.B., et al., *Label-free molecular imaging of immunological synapses between dendritic and T cells by Raman micro-spectroscopy.* Analyst, 2010. **135**(12): p. 3205-12.

27. Davies, D.R., *X-ray diffraction studies of macromolecules.* Annu Rev Biochem, 1967. **36**: p. 321-64.

28. Arnott, S., *The geometry of nucleic acids.* Prog Biophys Mol Biol, 1970. **21**: p. 265-319.

29. Tu, A.T., *Raman Spectroscopy in Biology: Principles and Applications*. 1982: Books on Demand.

30. Erfurth, S.C., E.J. Kiser, and W.L. Peticolas, *Determination of the backbone structure of nucleic acids and nucleic acid oligomers by laser Raman scattering.* Proc Natl Acad Sci U S A, 1972. **69**(4): p. 938-41.

31. Benevides, J.M. and G.J. Thomas, Jr., *Characterization of DNA structures by Raman spectroscopy: high-salt and low-salt forms of double helical poly(dG-dC) in H2O and D2O solutions and application to B, Z and A-DNA.* Nucleic Acids Res, 1983. **11**(16): p. 5747-61.

32. Chan, J.W., D.S. Taylor, and D.L. Thompson, *The effect of cell fixation on the discrimination of normal and leukemia cells with laser tweezers Raman spectroscopy.* Biopolymers, 2009. **91**(2): p. 132-9.

33. Mazur, A.I., et al., *Evaluating different fixation protocols for spectral cytopathology, part 1.* Anal Chem, 2012. **84**(3): p. 1259-66.

34. Birge, W.J., *A histochemical study of ribonucleic acid in differentiating ependymal cells of the chick embryo.* Anat Rec, 1962. **143**: p. 147-55.

35. Okano, H., et al., *Function of RNA-binding protein Musashi-1 in stem cells.* Experimental Cell Research, 2005. **306**(2): p. 349-56.

36. Finkenstadt, P.M., et al., *Somatodendritic localization of Translin, a component of the Translin/Trax RNA binding complex.* J Neurochem, 2000. **75**(4): p. 1754-62.

37. Kuersten, S. and E.B. Goodwin, *The power of the 3' UTR: translational control and development.* Nat Rev Genet, 2003. **4**(8): p. 626-37.

38. Macnicol, M.C. and A.M. Macnicol, *Developmental Timing of mRNA Translation-Integration of Distinct Regulatory Elements.* Molecular Reproduction and Development, 2010. **77**(8): p. 662-669.

39. Staiano-Coico, L., et al., *Human keratinocyte culture. Identification and staging of epidermal cell subpopulations.* J Clin Invest, 1986. **77**(2): p. 396-404.

40. Dinger, M.E., et al., *Long noncoding RNAs in mouse embryonic stem cell pluripotency and differentiation.* Genome Res, 2008. **18**(9): p. 1433-45.

41. Mercer, T.R., et al., *Long noncoding RNAs in neuronal-glial fate specification and oligodendrocyte lineage maturation.* BMC Neurosci, 2010. **11**: p. 14.

42. Pauli, A., J.L. Rinn, and A.F. Schier, *Non-coding RNAs as regulators of embryogenesis.* Nature Reviews Genetics, 2011. **12**(2): p. 136-149.

43. Guttman, M., et al., *lincRNAs act in the circuitry controlling pluripotency and differentiation.* Nature, 2011. **477**(7364): p. 295-U60.

Chapter 5: Monitoring the mineralisation of bone nodules in-vitro by space- and time-resolved Raman micro-spectroscopy

Raman microscopy was used as a label-free method to study the mineralisation of bone nodules formed by mesenchymal stem cells cultured in osteogenic medium in vitro. Monitoring 10 individual bone nodules over 28 days revealed temporal and spatial changes in the crystalline phase of the hydroxyapatite components of the nodules.

5.1 Introduction

The clinical demand for bone grafts is steadily increasing in many surgical procedures, such as hip revision, removal of bone tumours, treatment of congenital bone deformities and reconstruction surgery [49]. Newer alternative methods to autologus bone grafting are being developed by combining cells, scaffolds and bioreactors in laboratories, in order to produce engineered tissue with optimised properties [50-52]. Mesenchymal stem cells (MSCs) isolated from bone marrow aspirates have been used for bone tissue engineering and for in vitro studies of postnatal osteogenesis [53-57]. When cultured in osteogenic medium containing dexa-methasone (DEX), ascorbic acid phosphate and beta-glycerophosphate, MSCs can differentiate towards an osteoblastic phenotype and can form mineralised bone nodules, a process spanning over several weeks [55]. However, the information related to the composition of the mineral deposits and their evolution in time is limited. Most of the techniques used for the analysis of the bone nodules, such as Alizarin red [58] or Von Kossa staining [59], high resolution electron microscopy [60], polymerise chain reaction (PCR) [27] are destructive and can provide only single snap-shots. Therefore, the current understanding of the mineralisation process is mostly based on experimental results obtained at different time-points from parallel cultures. However, one of the difficulties when extrapolating information obtained from single time-point measurements of parallel cultures is related to the biological variability and cell-to-cell heterogeneity. The dynamic

patterns and the correlation between the temporal and spatial evolution of the bone nodules is mostly lost in snap-shot assays.

Raman spectroscopy is a label-free analytical technique that allows non-invasive measurements of the molecular properties of cells [19] and bone grown in-vitro [27]. It was shown that the frequency of the v1 vibration of the PO_4^{3-} changes with ionic incorporation and crystallinity of the apatite: 955-959 cm^{-1} in B-type apatite (carbonate substituted phosphate in apatite lattice), 962-964 cm^{-1} in nonsubstituted apatite, and 945-950 cm^{-1} in disordered hydroxyapatite lattice (probably A-type carbonate substitution, i.e. carbonate for hydroxide or amorphous CaP) [61, 62]. More recently, Raman spectroscopy has also been used to study the mineralisation of human MSCs cultured in osteogenic media in-vitro [6, 63] and to compare the mineral deposits at different time-points using parallel cultures.

Another important feature of Raman spectroscopy is that it allows in situ time and spatially-resolved measurements of live cells cultured in vitro, without disturbing the chemical and biological integrity of the cells. Recent studies showed that Raman spectroscopy can be used as a label free technique to measure chemical changes in apoptotic cells over periods of 35 minutes to 6 hours [64]. Raman spectroscopy has also been used for time-course experiments over 5-6 days to monitor the cardiac differentiation of human embryonic stem cells grown in purpose designed micro-bioreactors in-vitro [6].

Here, we show the feasibility of Raman spectroscopy to study the spatial and temporal development of individual bone nodules in vitro over durations as long as 28 days.

5.2 Materials and Methods

5.2.1 Raman micro-spectroscopy measurements

Cells were grown in purpose-designed bioreactors and the same areas of the cell cultures were repeatedly interrogated by Raman micro-spectroscopy at 48 hours intervals. The bone nodules were formed by human MSCs cultured in osteogenic medium (medium supplemented with dexamethasone, glycerophosphate and L-ascorbic acid-2-phosphate) and grown in purpose-designed bioreactors.

For the time-course experiment, Raman spectra were recorded using a Raman micro-spectrometer equipped with an environmental enclosure (Solent, Segensworth, UK). The chamber allowed the cells to be maintained at 37^0C, 5% CO_2 and avoid contamination. The instrument was develop by Dr Flavius Pascut [20] and consists of an inverted microscope (IX 71, Olympus, Essex, UK) with a 60×/NA 1.20 water-immersion objective (Olympus), a 785 nm ~170 mW diode laser (Toptica Photonics, Munich, Germany), a spectrometer equipped with a 830 lines/mm grating and cooled deep-depletion back-illuminated CCD detector (Andor Technologies, Belfast, UK) and an automated step-motor stage (Prior, Cambridge, UK).

The instrument was calibrated prior to each experiment using a standard 1,4 BSMB (Sigma-Aldrich, UK) sample with a precision of ~0.5 cm^{-1}in the 600-1800 cm^{-1} spectral region. Purpose designed titanium cell-chambers were built (25mm diameter and 15mm height) and incorporated a MgF_2 coverslip (0.17 mm thick) at

the bottom to enable acquisition of Raman spectra of the cells using the inverted optical configuration.

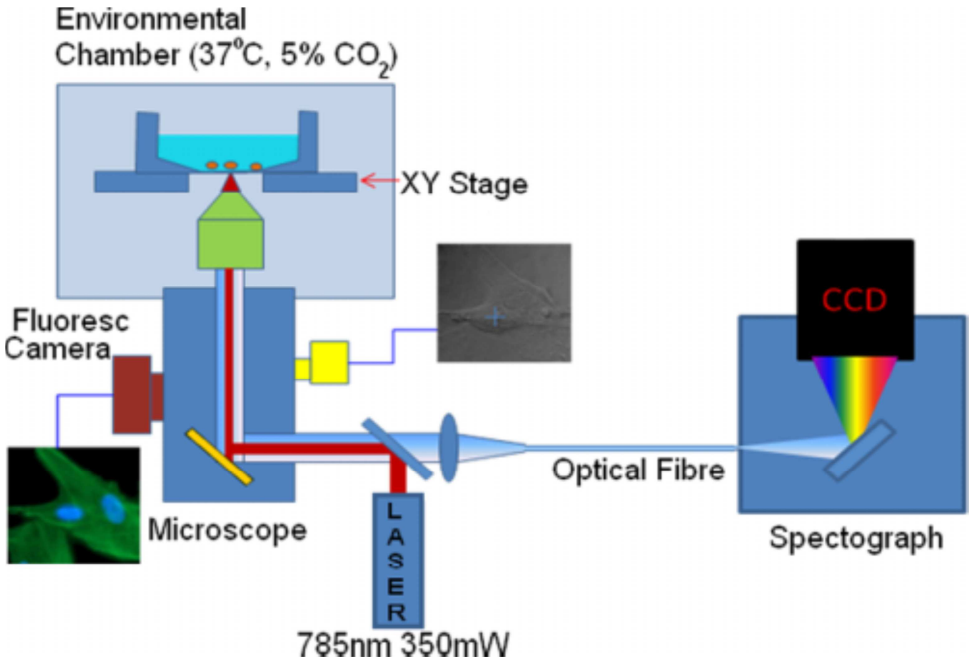

Figure 5.1 Schematic description of the Raman micro-spectrometer: inverted optical microscope with automated sample stage, 785 nm laser, water immersion objective spectrograph and CCD detector [22]

To account for biological variability of the live cells, for each bioreactor seven areas were measured at 2 or 3 days intervals by raster scanning the samples through the laser focus with 3 μm steps size (equivalent to a grid of 70 by 70 points), with acquisition time of 1 s/pixel at each position. Between the Raman spectroscopy measurements the cells were returned in the incubator. At the end of

the time-course experiment, the cultures were fixed and stained with Alizarin red to highlight the calcium mineral areas.

5.2.2 Data analysis and processing

Data analysis was performed in Matlab 2011 (MathWorks Inc., Natick, MA). Spectra containing cosmic rays were removed and singular value decomposition (SVD) was used to reduce the noise. The resulting Raman spectra from SVD procedure were analysed via univariate data analysis and principal component analysis (PCA). PCA images were constructed by projecting the scores corresponding to the principal components that showed bands corresponding to hydroxyapatite (HA). Univariate spectral images corresponding to selected Raman bands were obtained by calculating the area under the spectral bands after subtraction of estimated local linear baselines and representing the integrated intensity values at each measurement position in the cell.

5.3 Results and discussion

At day 1, all cells had a fibroblast-like morphology and covered the entire area of the coverslips forming a compact layer. Significant changes in the morphology and density of the cells cultured in the osteogenic and control media

were observed after 4 days (Figure 5.2). These images indicate that the cells grown in the osteogenic medium had a higher proliferation rate compared to cells cultured in the control medium.

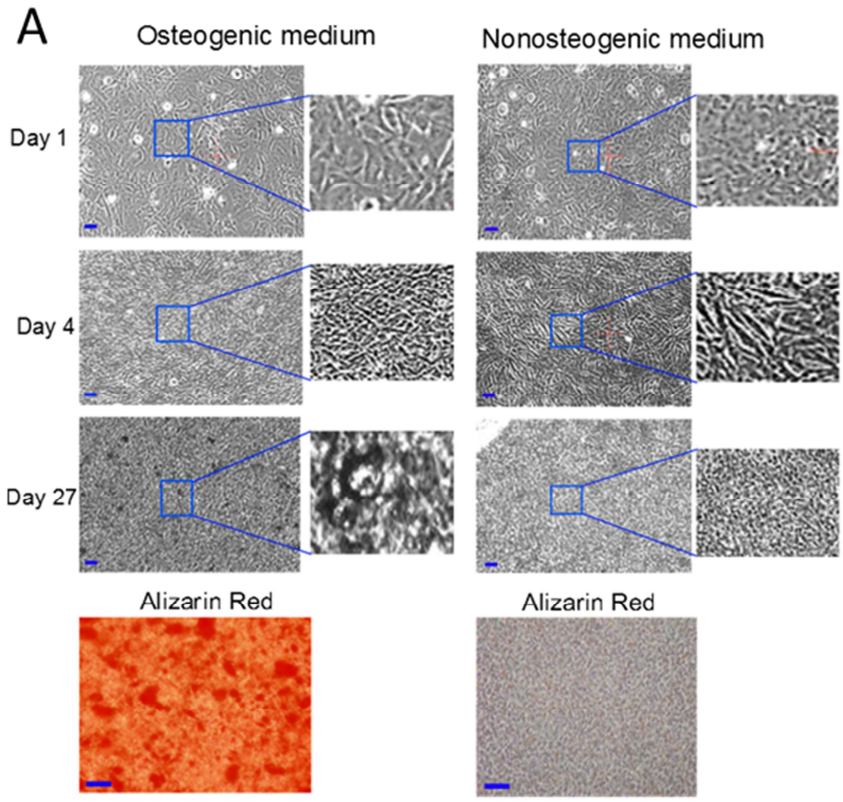

Figure 5.2 (A) Phase contrast images of MSCs cultured in osteogenic and control media. Alizarin staining was performed at day 27 or 28. Scale bars: 10µm. (B) Mean time-course Raman spectra of typical 210×210 mm^2 regions of the cultures shown in (A).

Aggregated structures approximately 10µm in size were observed starting with day 12. The number and size of these structures increased constantly with time, reaching 10-70 µm diameter and a density of ~7 nodules for areas of 210 µm x 210µm. For the 50 cells grown in the control media, no major morphological

changes were observed during the 28 days period. Alizarin red staining was carried out at the end of the time-course experiment and confirmed the formation of calcium mineral deposits only for the MSCs cultured in osteogenic medium. Other papers have reported similar time scales for mineralization [13] and indicated that bone nodule crystallisation started with the formation of aggregated structures [18, 21]. For the cells grown in the control media, no major morphological changes were observed during measurements. Alizarin red staining was carried out at the end of the time-course experiment and confirmed the formation of mineral deposits when MSCs were cultured in osteogenic medium. The calcium phosphate structures observed by alizarin red staining tend to spread out and cover the entire surface of coverslip. The sizes of these structures can vary from 10 µm up to 70 µm depending on the morphology.

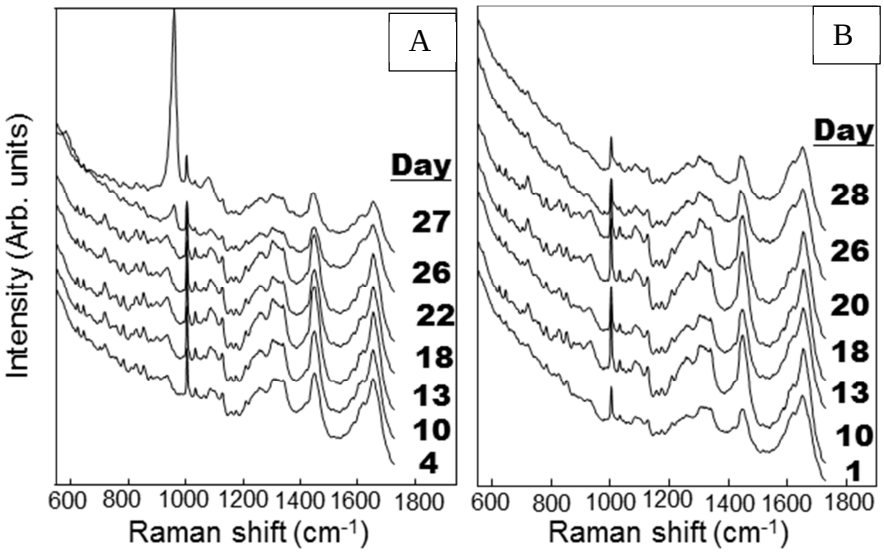

Figure 5.3 Raman spectra at different time points for the same regions of the culture A) osteoblast in osteogenic medium and B) non-osteogenic medium.

To obtain information regarding the spatial and temporal chemical composition of the samples we used Raman spectroscopy to measure several areas of the cells in osteogenic and control media. Figure 5.3 compares the time evolution of the mean Raman spectra for two regions of cell cultures kept in osteogenic and non-osteogenic mediums. The spectra have all the Raman bands characteristic to the main cellular biomolecules (nucleic acids, protein, lipids and carbohydrates) and are consistent with previous reports on other cell types [22].

Spectral differences are observed throughout every stage of osteoblast differentiation and bone mineralization become obvious in the computed difference spectra, i.e. subtract of average Raman spectra of osteoblast region minus control cell region (figure 5.4). Prior to that, each Raman spectra had the baseline removed and normalized. Positive peaks at 782 cm^{-1}corresponding to nucleic acids [23], 717 cm^{-1} phospholipids [22], 1004 cm^{-1} phenylalanine [24] can be observed at days 1, 5 and 9. The increased contribution from nucleic acids relates to a higher cell proliferation rate for cell grown in the osteogenic medium at the early stage, whereas the positive evolution of bands assigned to proteins in Raman spectra is as an indication of extracellular matrix (ECM) production. The extracellular matrix is known to consist of proteins and serves as a mineralization support [12] and connective medium for the mineral part of the bone [25]. Although collagen is a major part of ECM, no Raman band specific to collagen type I or Type II were noticed in the Raman spectra. At days 15- 20, mineralisation of the bone nodules is indicated by the increase in the intensity of the Raman band at 950-958 cm^{-1} assigned to the PO_4^{3-} symmetric stretching of hydroxyapatite (figure 5.4) and

continued to increase until the end of experiments (day 28). Previous work showed that the formation of hydroxyapatite crystals can be produce during bone mineralization either by heterogeneous nucleation of Ca and P crystals by collagen and phospho-protein complex [26] and /or calcium and phosphate accumulation in matrix vesicles [27-29]. Because no spectral bands characteristic to collagen were detected in the Raman spectra it is likely that the mineralization process leads to the formation of an aggregated structure which have been previously and described in literature as a dystrophic mineral [11]. In such structures CaP crystal are formed by precipitation of inorganic calcium ions and phosphate [30].

Figure 5.4: Time course difference spectra of osteoblast and control cells.

While the average Raman spectra provide information regarding the overall molecular changes of the cells during differentiation and mineralisation, Figure 5.2 shows that the cultures are highly heterogeneous. Therefore, principal component

analysis (PCA) was used to analyse the time-resolved spectral maps of all measured areas to capture both the temporal and the spatial molecular changes.

Figure 5.5 (A) Maps corresponding to the PC2 scores recorded for the same culture regions at different measurements days. (B) The loadings corresponding to the first four principal components. Scale bar: 10 μm.

Figure 5.5A presents the loadings corresponding to the first four principal components accounting for most of the spectral variability. The 2nd principal component (PC2) contained an intense band assigned to the PO_4^{3-} symmetric stretching, indicating mineralisation. Fig. 5.5B presents the time course spectral maps corresponding to the PC2 scores for three typical areas of the cell cultures. The results show that the mineralization occurs in different sizes and shapes, from round to irregular hand-like shapes. The size of the round shapes varied between 10 to 20 μm, whereas the irregular shapes were ~40 μm. To obtain more insight into the mineralisation of the bone nodules, a more detailed analysis of the spectral region 940-990 cm^{-1} was carried out. Previous reports indicated that PO_4^{3-} stretching in crystalline hydroxyapatite produces a sharp peak at 958 cm^{-1} while the frequency of this vibrational mode is found in the 945-950 cm^{-1} range for disordered phase hydroxyapatite [15].

The PCA analysis also indicated that the peak at 958 cm^{-1} appears to be asymmetric due to the overlap of several Raman bands. Using a peak deconvolution algorithm, it was possible to separate the peaks corresponding to the disordered and crystalline hydroxyapatite.

Figure 5.6A presents the results of the peak deconvolution algorithm for a typical bone nodule and shows that the intensity of the Raman band corresponding to crystalline hydroxyapatite increases with time compared to the band corresponding to the amorphous phase. Figure 5.6B presents the computed the time dependence of the ratio between peaks at 958 cm^{-1} (crystalline HA) and 945 cm^{-1} (disordered HA) for five bone nodules.

Figure 5.6 (A) Time evolution of Raman spectra of a typical bone nodule. (B) Spectral deconvolution of a bone nodule during the early stages of mineralisation (days 15-19). (C) The temporal profiles of the computed ratio between the intensity of the Raman bands corresponding to 55 crystalline (I958/I948) and amorphous hydroxyapatite for 5 bone nodules

The amorphous phase is more abundant in the newly form bone nodules and evolves towards a more crystalline phase. Our results show that the overall crystalline to amorphous ratio for each bone nodule doubles in approximately 4 days after the start of mineralisation. These results obtained at a single bone-nodule level confirm the earlier hypothesis proposed by Posner based X-ray spectroscopy data obtained from bone nodules analysed at different time points [31]. Our results

support the hypothesis that the amorphous phosphate is secreted by osteoblasts and can be regarded as a transient precursor to the crystalline phase [32] and is deposited after mineralization in the ECM [13]. Figure 5.6B confirms the tendency of amorphous phase to convert into a crystalline phase over time. Despite the fact that other groups have reported the presence of additional transient calcium phosphate phases like octalcalcium phosphate (OCP), Raman bands corresponding to OCP were not present in our spectra.

The acquisition of the spectral maps by raster-scanning Raman microscopy combined with the peak deconvolution analysis also provides time-resolved information related to the spatial distribution of the amorphous and crystalline phases of hydroxyapatite for individual bone nodules. Figure 5.7 presents the line-profiles for the peak intensity ratio I958/I948 calculated at the start of mineralisation (day 15) and 4 days later for typical round and irregular shaped nodules.

The results (figure 5.7B) show that the ratio between crystalline and disordered phase decreases strongly (2-3 times) over a 5 □m distance at the edges of the bone nodules, regardless of the shape of the nodules. The central parts of the bone nodules have a high contribution of crystalline hydroxyapatite while the disordered phase is dominant at the edges. Apparently the amorphous phase tends to accumulate at the edges, followed by a phase transformation in the following days. This finding is in agreement with the overall increase in intensity of the Raman band corresponding to the crystalline HA over time (see figure 5.6 B).

Figure 5.7 (A) PC2 maps for two individual bone nodules. (B) Line profiles at days 15 and 19 (sample 1 on the right and sample 2 on the left). The dash lines in (A) represents the line profile region.

5.3 Conclusion

This chapter demonstrates the potential of Raman spectroscopy to perform non-invasive time course experiments on live stem cells over periods as long as four weeks and to measure molecular changes related to in vitro mineralisation. For MSCs cultured in osteogenic medium, spatial and temporal analysis of the Raman spectra indicate that initially the bone nodules consist mainly of amorphous HA that transforms into crystalline HA. A deconvolution algorithm allowed the separation of the spectral contribution from amorphous and crystalline hydroxyapatite and proved that the crystalline phase increases in time over amorphous phase for each individual bone nodule. Amorphous HA is detected at the edges of the bone nodules even at the late stages of mineralisation, suggesting that during the development of the bone nodules, amorphous hydroxyapatite tends to form at the edges of the nodules, followed by a phase transformation in the following days. This study highlights the potential of Raman spectroscopy for non-invasive label-free characterisation of bone nodules.

References

1. Liang, H., et al., *Wavelength dependence of cell cloning efficiency after optical trapping.* Biophysical Journal, 1996. **70**(3): p. 1529-33.
2. Neuman, K.C., et al., *Characterization of photodamage to Escherichia coli in optical traps.* Biophysical Journal, 1999. **77**(5): p. 2856-63.
3. http://microscope.olympus-global.com/uis2/en/uplsapo60xw/, *UPLSAPO 60XW.*
4. Technology, C., *Long Pass filter*. 2010.
5. Semrock. *45^0 dichroic mirror*. Available from: http://www.semrock.com/Catalog/Detail.aspx?FilterPartID=767&CategoryID=11.
6. Pully, V.V., et al., *Microbioreactors for Raman microscopy of stromal cell differentiation.* Anal Chem, 2010. **82**(5): p. 1844-50.
7. Kalladka, D. and K.W. Muir, *Stem cell therapy in stroke: Designing clinical trials.* Neurochemistry International, 2011. **59**(3): p. 367-370.
8. Lilienfeld, D.E. and D.P. Perl, *Projected Neurodegenerative Disease Mortality among Minorities in the United-States, 1990-2040.* Neuroepidemiology, 1994. **13**(4): p. 179-186.
9. Rossi, F. and E. Cattaneo, *Opinion - Neural stem cell therapy for neurological diseases: dreams and reality.* Nature Reviews Neuroscience, 2002. **3**(5): p. 401-409.
10. Alcock, J. and V. Sottile, *Dynamic distribution and stem cell characteristics of Sox1-expressing cells in the cerebellar cortex.* Cell Research, 2009. **19**(12): p. 1324-1333.
11. Arocena, M., et al., *A Time-Lapse and Quantitative Modelling Analysis of Neural Stem Cell Motion in the Absence of Directional Cues and in Electric Fields.* Journal of Neuroscience Research, 2010. **88**(15): p. 3267-3274.
12. Fox, J.L., *FDA scrutinizes human stem cell therapies.* Nature Biotechnology, 2008. **26**(6): p. 598-599.
13. Fukuda, H., et al., *Fluorescence-activated cell sorting-based purification of embryonic stem cell-derived neural precursors averts tumor formation after transplantation.* Stem Cells, 2006. **24**(3): p. 763-771.
14. Notingher, I., et al., *In situ spectral monitoring of mRNA translation in embryonic stem cells during differentiation in vitro.* Anal Chem, 2004. **76**(11): p. 3185-3193.
15. Zuser, E., et al., *Confocal Raman microspectral imaging (CRMI) of murine stem cell colonies.* Analyst, 2010. **135**(12): p. 3030-3.
16. Chan, J.W., et al., *Label-Free Separation of Human Embryonic Stem Cells and Their Cardiac Derivatives Using Raman Spectroscopy.* Anal Chem, 2009. **81**(4): p. 1324-1331.
17. Schulze, H.G., et al., *Assessing Differentiation Status of Human Embryonic Stem Cells Noninvasively Using Raman Microspectroscopy.* Anal Chem, 2010. **82**(12): p. 5020-5027.

18. Konorov, S.O., et al., *Evidence of marked glycogen variations in the characteristic Raman signatures of human embryonic stem cells.* Journal of Raman Spectroscopy, 2011. **42**(5): p. 1135-1141.
19. Pascut, F.C., et al., *Noninvasive detection and imaging of molecular markers in live cardiomyocytes derived from human embryonic stem cells.* Biophys J, 2011. **100**(1): p. 251-9.
20. Konorov, S.O., et al., *Raman microspectroscopic evidence that dry-fixing preserves the temporal pattern of non-specific differentiation in live human embryonic stem cells.* Journal of Raman Spectroscopy, 2011. **42**(4): p. 576-579.
21. Notingher, I. and L.L. Hench, *Raman microspectroscopy: a noninvasive tool for studies of individual living cells in vitro.* Expert Review of Medical Devices, 2006. **3**(2): p. 215-234.
22. Zoladek, A., et al., *Non-invasive time-course imaging of apoptotic cells by confocal Raman micro-spectroscopy.* Journal of Raman Spectroscopy, 2011. **42**(3): p. 251-258.
23. Kuimova, M.K., K.L.A. Chan, and S.G. Kazarian, *Chemical Imaging of Live Cancer Cells in the Natural Aqueous Environment.* Applied Spectroscopy, 2009. **63**(2): p. 164-171.
24. Marcsisin, E.J., et al., *Infrared microspectroscopy of live cells in aqueous media.* Analyst, 2010. **135**(12): p. 3227-3232.
25. Kim, B.S., et al., *Growth, differentiation, and biochemical signatures of rhesus monkey mesenchymal stem cells.* Stem Cells Dev, 2008. **17**(1): p. 185-98.
26. Konorov, S.O., et al., *Absolute Quantification of Intracellular Glycogen Content in Human Embryonic Stem Cells with Raman Microspectroscopy.* Anal Chem, 2011. **83**(16): p. 6254-6258.
27. Gentleman, E., et al., *Comparative materials differences revealed in engineered bone as a function of cell-specific differentiation.* Nature Materials, 2009. **8**(9): p. 763-770.
28. Pascut, F.C., et al., *Toward label-free Raman-activated cell sorting of cardiomyocytes derived from human embryonic stem cells.* J Biomed Opt, 2011. **16**(4).
29. Matthaus, C., et al., *Label-free detection of mitochondrial distribution in cells by nonresonant Raman microspectroscopy.* Biophys J, 2007. **93**(2): p. 668-73.
30. Uzunbajakava, N., et al., *Nonresonant confocal Raman imaging of DNA and protein distribution in apoptotic cells.* Biophys J, 2003. **84**(6): p. 3968-3981.
31. Zoladek, A.B., et al., *Label-free molecular imaging of immunological synapses between dendritic and T cells by Raman micro-spectroscopy.* Analyst, 2010. **135**(12): p. 3205-12.
32. Davies, D.R., *X-ray diffraction studies of macromolecules.* Annu Rev Biochem, 1967. **36**: p. 321-64.
33. Arnott, S., *The geometry of nucleic acids.* Prog Biophys Mol Biol, 1970. **21**: p. 265-319.

34. Tu, A.T., *Raman spectroscopy in biology: principles and applications*. 1982: Wiley.
35. Erfurth, S.C., E.J. Kiser, and W.L. Peticolas, *Determination of the backbone structure of nucleic acids and nucleic acid oligomers by laser Raman scattering.* Proc Natl Acad Sci U S A, 1972. **69**(4): p. 938-41.
36. Benevides, J.M. and G.J. Thomas, Jr., *Characterization of DNA structures by Raman spectroscopy: high-salt and low-salt forms of double helical poly(dG-dC) in H2O and D2O solutions and application to B, Z and A-DNA.* Nucleic Acids Res, 1983. **11**(16): p. 5747-61.
37. Chan, J.W., D.S. Taylor, and D.L. Thompson, *The effect of cell fixation on the discrimination of normal and leukemia cells with laser tweezers Raman spectroscopy.* Biopolymers, 2009. **91**(2): p. 132-9.
38. Mazur, A.I., et al., *Evaluating different fixation protocols for spectral cytopathology, part 1.* Anal Chem, 2012. **84**(3): p. 1259-66.
39. Birge, W.J., *A histochemical study of ribonucleic acid in differentiating ependymal cells of the chick embryo.* Anat Rec, 1962. **143**: p. 147-55.
40. Okano, H., et al., *Function of RNA-binding protein Musashi-1 in stem cells.* Experimental Cell Research, 2005. **306**(2): p. 349-56.
41. Finkenstadt, P.M., et al., *Somatodendritic localization of Translin, a component of the Translin/Trax RNA binding complex.* J Neurochem, 2000. **75**(4): p. 1754-62.
42. Kuersten, S. and E.B. Goodwin, *The power of the 3' UTR: translational control and development.* Nat Rev Genet, 2003. **4**(8): p. 626-37.
43. Macnicol, M.C. and A.M. Macnicol, *Developmental Timing of mRNA Translation-Integration of Distinct Regulatory Elements.* Molecular Reproduction and Development, 2010. **77**(8): p. 662-669.
44. Staiano-Coico, L., et al., *Human keratinocyte culture. Identification and staging of epidermal cell subpopulations.* J Clin Invest, 1986. **77**(2): p. 396-404.
45. Dinger, M.E., et al., *Long noncoding RNAs in mouse embryonic stem cell pluripotency and differentiation.* Genome Res, 2008. **18**(9): p. 1433-45.
46. Mercer, T.R., et al., *Long noncoding RNAs in neuronal-glial fate specification and oligodendrocyte lineage maturation.* BMC Neurosci, 2010. **11**: p. 14.
47. Pauli, A., J.L. Rinn, and A.F. Schier, *Non-coding RNAs as regulators of embryogenesis.* Nature Reviews Genetics, 2011. **12**(2): p. 136-149.
48. Guttman, M., et al., *lincRNAs act in the circuitry controlling pluripotency and differentiation.* Nature, 2011. **477**(7364): p. 295-U60.
49. Damien, C.J. and J.R. Parsons, *Bone graft and bone graft substitutes: a review of current technology and applications.* J Appl Biomater, 1991. **2**(3): p. 187-208.
50. Griffith, L.G. and G. Naughton, *Tissue engineering - Current challenges and expanding opportunities.* Science, 2002. **295**(5557): p. 1009-+.
51. Vacanti, J.P. and R. Langer, *Tissue engineering: the design and fabrication of living replacement devices for surgical reconstruction and transplantation.* Lancet, 1999. **354**: p. Si32-Si34.

52. Lysaght, M.J. and J. Reyes, *The growth of tissue engineering.* Tissue Eng, 2001. **7**(5): p. 485-93.
53. Beresford, J.N., S.E. Graves, and C.A. Smoothy, *Formation of mineralized nodules by bone derived cells in vitro: a model of bone formation?* Am J Med Genet, 1993. **45**(2): p. 163-78.
54. Cheng, S.L., et al., *Differentiation of human bone marrow osteogenic stromal cells in vitro: induction of the osteoblast phenotype by dexamethasone.* Endocrinology, 1994. **134**(1): p. 277-86.
55. Jaiswal, N., et al., *Osteogenic differentiation of purified, culture-expanded human mesenchymal stem cells in vitro.* J Cell Biochem, 1997. **64**(2): p. 295-312.
56. Pittenger, M.F., et al., *Multilineage potential of adult human mesenchymal stem cells.* Science, 1999. **284**(5411): p. 143-7.
57. Sottile, V., et al., *Stem cell characteristics of human trabecular bone-derived cells.* Bone, 2002. **30**(5): p. 699-704.
58. Gough, J.E., J.R. Jones, and L.L. Hench, *Nodule formation and mineralisation of human primary osteoblasts cultured on a porous bioactive glass scaffold.* Biomaterials, 2004. **25**(11): p. 2039-46.
59. Bonewald, L.F., et al., *Von Kossa Staining Alone Is Not Sufficient to Confirm that Mineralization In Vitro Represents Bone Formation.* Calcified Tissue International, 2003. **72**(5): p. 537-547.
60. Mahamid, J., et al., *Bone mineralization proceeds through intracellular calcium phosphate loaded vesicles: A cryo-electron microscopy study.* Journal of Structural Biology, 2011. **174**(3): p. 527-535.
61. Tarnowski, C.P., M.A. Ignelzi, and M.D. Morris, *Mineralization of developing mouse calvaria as revealed by Raman microspectroscopy.* Journal of Bone and Mineral Research, 2002. **17**(6): p. 1118-1126.
62. Timlin, J.A., et al., *Raman spectroscopic imaging markers for fatigue-related microdamage in bovine bone.* Analytical Chemistry, 2000. **72**(10): p. 2229-2236.
63. McManus, L.L., et al., *Raman spectroscopic monitoring of the osteogenic differentiation of human mesenchymal stem cells.* Analyst, 2011. **136**(12): p. 2471-81.
64. Okada, M., et al., *Label-free Raman observation of cytochrome c dynamics during apoptosis.* Proc Natl Acad Sci U S A, 2012. **109**(1): p. 28-32.

Chapter 6: Conclusions

6.1 Conclusions of the thesis

The research presented in this thesis was motivated by the need for label-free methods characterization of cell for tissue engineering applications. The experimental chapters of this thesis provide strong evidence that Raman spectroscopy can be used as a non-destructive, non-invasive, label free tool for cell discrimination and in-situ monitoring of molecular dynamics. The thesis is divided into six chapters, with the first chapters dedicated to a brief review of existing methods for chemical analysis of single cells, theoretical overview of Raman scattering and optical design of Raman micro-spectrometers.

Chapter 3 focus on the practical aspects of instrumental development of an optimized Raman micro-spectrometer instrumental design; system characterization for stability, spectral resolution and optimization of the confocal setup for the best compromise axial resolution vs Raman signal; first NIR Raman spectral maps of endothelial cells.

In Chapter 4 Raman spectroscopy was used to identify molecular markers that can be used to determine the differentiation status of live neural stem cells in vitro. The nucleic acids are the markers responsible for discrimination between neural progenitor and glia cells, with a higher concentration reported in neuro-progenitor. These results open new doors for a potentially label free discrimination of neural stem cells in vitro. The statistical model based on PCA data analysis probes the high accuracy in discrimination with 89.4% sensitivity and 96.4%

specificity. Raman maps associated to nucleic acids were compared to fluorescence images of the same cells to establish the origins of these differences in the Raman spectra. Maps corresponding to Raman bands specific to DNA and RNA indicates the presence of regions with high concentration of RNA spectral within the cytoplasmic region.

Chapter 5 reports for the first time the ability to perform Raman time course experiments to study the mineralisation of bone nodules formed by mesenchymal stem cells in-vitro.

Biological processes such as cell proliferation and crystallization of bone nodules were followed and analysed for the same nodule. Raman spectra confirmed the presence of band corresponding to amorphous and crystalline hydroxipapatite. Analysis of the time-course spectra indicated a higher contribution of the crystalline phase over the amorphous phase at a later stage of mineralization.

6.2 Future work

Taking advantage of high delivery maximum output power (≈3W) of Ti:sapphire laser, further improvement to the Raman micro-spectrometer can be achieved by switching from point scanning to line scanning and changing the mirror based spectrograph with a lens based spectrograph. Holographic imaging spectrograph from Kaiser optical with high throughput (*f*/1.8) and equipped with

custom NIR transmission gratings optics can provide a significant advantage in acquisition time and spatial integrity in demanding Raman imaging applications.

Thus a larger area can be scanned in a shorter amount of time preserving the sensitivity of detection achieved in point scanning design with great potential for a large number of sample measurements such as tissue section analysis large or cell sorting.